

MEMS RESONANT TEMPERATURE SENSING WITH VARIABLE  
COUPLING STIFFNESS AND IMPROVED SENSITIVITY

A THESIS SUBMITTED TO  
THE GRADUATE SCHOOL OF NATURAL AND APPLIED SCIENCES  
OF  
MIDDLE EAST TECHNICAL UNIVERSITY

BY

ERTUĞ ŞİMŞEK

IN PARTIAL FULFILLMENT OF THE REQUIREMENTS  
FOR  
THE DEGREE OF MASTER OF SCIENCE  
IN  
MICRO AND NANOTECHNOLOGY

SEPTEMBER 2020



Approval of the thesis:

**MEMS RESONANT TEMPERATURE SENSING WITH VARIABLE  
COUPLING STIFFNESS AND IMPROVED SENSITIVITY**

submitted by **ERTUĞ ŞİMŞEK** in partial fulfilment of the requirements for the degree of **Master of Science in Micro and Nanotechnology, Middle East Technical University** by,

Prof. Dr. Halil Kalıpçılar  
Dean, Graduate School of **Natural and Applied Sciences**

Prof. Dr. Almıla Güvenç Yazıcıoğlu  
Head of the Department, **Micro and Nanotechnology**

Assoc. Prof. Dr. Kıvanç Azgın  
Supervisor, **Mechanical Eng. Dept., METU**

Assist. Prof. Dr. Emre Yüce  
Co-Supervisor, **Physics, METU**

**Examining Committee Members:**

Prof. Dr. Haluk Külah  
Electrical and Electronics Eng., METU

Assoc. Prof. Dr. Kıvanç Azgın  
Mechanical Eng. Dept., METU

Assoc. Prof. Dr. Ulaş Yaman  
Mechanical Eng. Dept., METU

Assoc. Prof. Dr. Sezer Özerinç  
Mechanical Eng. Dept., METU

Assist. Prof. Dr. Erdiñç Tatar  
Electrical and Electronics Eng. Dept., Bilkent Uni.

Date: 23.09.2020

**I hereby declare that all information in this document has been obtained and presented in accordance with academic rules and ethical conduct. I also declare that, as required by these rules and conduct, I have fully cited and referenced all material and results that are not original to this work.**

Name, Last name : Ertuğ Şimşek

Signature :

## ABSTRACT

### **MEMS RESONANT TEMPERATURE SENSING WITH VARIABLE COUPLING STIFFNESS AND IMPROVED SENSITIVITY**

Şimşek, Ertuğ

Master of Science, Micro and Nanotechnology

Supervisor: Assoc. Prof. Dr. Kıvanç Azgın

Co-Supervisor: Assist. Prof. Dr. Emre Yüce

September 2020, 84 pages

This thesis presents the design, modelling, fabrication and characterization of a resonance based MEMS temperature sensor with improved sensitivity. The temperature sensor is composed of an electrostatically coupled double ended-tuning fork (DETF) MEMS resonator. The sensor utilizes the thermal expansion coefficient difference of the materials to detect the temperature change. The design consists of 2 resonator tines where each of them has two capacitive plates on each side. The capacitive plates facing each other on the inner side of the resonators are used for the electrostatic coupling, which is the crucial point of the study. The negative electrostatic coupling stiffness generated between these tines enables mode-ordering. By mode-ordering, the sensor can be operated closer to pull-in in order to achieve higher sensitivity for the out-of-phase mode. The outside capacitive plates are used for actuation and sensing, whose mechanisms are explained with the equations. The analytical model is presented with the thermo-electro-mechanical equations for the mode shapes and their corresponding natural frequencies. The model is verified by the Finite Element Analysis by comparing the resonance frequencies of the modes

of interests. In FEM analysis, the effects of the electrostatic coupling are shown with the parametric sweep for the various proof mass voltage configurations with the thermal expansion physics node included. Having the thermal expansion, the effect of the temperature increase is shown in the modal analysis as the frequency shift in the mode of interests. The characterization tests are performed in a vacuum environment. The quality factor for the out-of-phase mode is about 25500 at a pressure of around 0.15mTorr. Resonance frequencies for the mode of interests of the resonator are close to the analytical model and the FEM simulation results. The effect of the electrostatic softening effect is investigated for the same, and the opposite sign proof mass voltage configurations. The frequency change for the opposite sign proof mass configuration from 6V to 20V is 3063Hz and 666Hz for out-of-phase and in-phase, respectively. For the same proof mass configuration, the resonance frequency shifts 579Hz. The out-of-phase mode and the in-phase mode frequency changes for the temperature increase from 25°C to 65°C are 1078Hz and 988 Hz for the  $V_{PM1}=20V$  and  $V_{PM2}=-20V$ . For the same proof mass configuration ( $V_{PM1}=20V$  and  $V_{PM2}=20V$ ), the frequency change is 986Hz, still lower than the in-phase mode frequency of the opposite sign proof mass voltage configuration but very close as expected. The overall sensitivities are obtained using the maxima of the frequency response plots. For the opposite sign proof mass configuration, out-of-phase mode and in-phase mode temperature sensitivity are increased from 24.4Hz/K to 26.5Hz/K and 24Hz/K to 24.4Hz/K, respectively, with the voltage increase from 8V to 20V. This study shows that the temperature sensitivity can be increased by varying coupling stiffness by adjusting the proof mass voltages close to pull-in voltage and mode-ordering.

Keywords: MEMS, Resonator, Double-Ended Tuning Fork (DETF), Temperature Sensor

## ÖZ

### **YÜKSEK ÇÖZÜNÜRLÜKLÜ, DEĞİŞKEN EŞLENİK YAY SABİTLİ TİTREŞİM TABANLI MEMS SICAKLIK SENSÖRÜ**

Şimşek, Ertuğ  
Yüksek Lisans, Mikro ve Nanoteknoloji  
Tez Yöneticisi: Doç. Dr. Kıvanç Azgın  
Ortak Tez Yöneticisi: Dr. Öğr. Üyesi Emre Yüce

Eylül 2020, 84 sayfa

Bu tez, geliştirilmiş hassasiyete sahip bir rezonant tabanlı MEMS sıcaklık sensörünün tasarımını, modellemesini, imalatını ve karakterizasyonunu sunmaktadır. Sıcaklık sensörü elektrostatik olarak bağlı çift sonlu ayar çatalı (DETF) MEMS rezonatör içerir. Sensör, sıcaklık değişimini tespit etmek için termal genişleme katsayısı farkı prensibini kullanır. Tasarım, her birinin her iki tarafında iki kapasitif plakaya sahip olan 2 rezonatör çatalından oluşur. Rezonatörün iç kısmında birbirine bakan kapasitif plakalar çalışmanın can alıcı noktası olan elektrostatik bağlantı için kullanılır. Negatif elektrostatik bağlantı sertliği mod sıralamasını sağlar. Mod sıralaması ile sensör, daha yüksek hassasiyet elde etmek amacıyla faz dışı mod için sınır yapışma gerilimine çok yakın çalıştırılabilir. Denklemlerle çalışma mekanizmaları açıklanan dış kapasitif plakalar çalıştırma ve algılama için kullanılır. Analitik model, mod şekilleri ve karşılık gelen doğal frekanslar için termo-elektro-mekanik denklemlerle sunulur. Model, ilgili modlarının rezonans frekansları karşılaştırılarak sonlu eleman analizi ile doğrulanır. Sonlu eleman analizinde,

elektrostatik bağlanmanın etkileri, çeşitli gövde kütle voltajı konfigürasyonları için termal genleşme fizik düğümü dahil edilerek parametrik taramayla gösterilmiştir. Isıl genleşme dahil edilerek, sıcaklık artışının etkisi modal analizde ilgili modlardaki frekans kayması olarak gösterilir. Karakterizasyon testleri vakum ortamında gerçekleştirilir. Zıt fazlı mod için kalite faktörü, 0.15mTorr civarındaki bir basınçta yaklaşık 25500'dür. Rezonatörün ilgili modu için rezonans frekansları analitik modele ve FEM simülasyon sonuçlarına yakındır. Elektrostatik yumuşatma etkisinin etkisi aynı ve zıt işarete gövde kütle voltaj konfigürasyonları için araştırılmıştır. Zıt işaretli kütle gövde voltajı yapılandırması için 6V'den 20V'ye frekans değişimi, sırasıyla faz dışı ve faz içi için sırasıyla 3063Hz ve 666Hz'dir. Aynı işaretli gövde kütle voltajı konfigürasyonu için, rezonans frekans değişimi 579Hz'tir. 25°C'den 65°C'ye sıcaklık artışı için faz dışı mod ve faz içi mod frekansı değişiklikleri, VPM1=20V ve VPM2=-20V için 1078Hz ve 988 Hz'dir. Aynı gövde kütle voltajı konfigürasyonu için (VPM1 = 20V ve VPM2 = 20V), frekans değişimi 986Hz'dir. Zıt işaretli gövde kütle voltaj konfigürasyonununun faz içi mod frekansına çok yakın olsa da beklendiği gibi daha düşüktür. Genel sıcaklık hassasiyetleri frekans yanıtı grafiklerinin maksimumlarından elde edilmiştir. Zıt işaretli gövde kütle konfigürasyonu için faz dışı ve faz içi sıcaklık hassasiyetinin 8V'tan 20 V'a doğru olan gerilim artışı ile, sırasıyla, 24.4 Hz/K'den, 26,5 Hz/K'e ve 24 Hz/K'den, 24,4Hz/K'e arttığı gözlemlenmiştir. Bu çalışma, kütle voltaj geriliminin, sınır yapışma gerilimine yaklaştırılarak, bağlantı sertliği değiştirilmesi ve mod sıralaması ile sıcaklık hassasiyetinin artırılabilceğini göstermektedir.

Anahtar Kelimeler: MEMS, Rezonatör, Çift Taraflı Ayarlama Çatalı, Sıcaklık Algılayıcı

*To Great Author*

&

*My family,*

## ACKNOWLEDGMENTS

Firstly, I would like to express my deepest gratitude to my thesis advisor Assoc. Prof. Dr. Kıvanç Azgın for his friendly relationship, valuable discussions and guidance throughout my graduate studies.

I would like to thank Onurcan Kaya for his support, guidance, help in the research lab, sharing his valuable experience on characterization and great friendship.

I would like to thank Orhan Akar for his insight, guidance, support and help in microfabrication processes and cleanroom training. Without him, I would not have such a fabrication point of view. I am also thankful to Adem Saraç, Ahmet Murat Yağcı, Akın Aydemir, Evren Erdil, Hasan Gavcar, Kadir Ulak, Levent Abat, Oğuzhan Temel, Taylan Töral, and all METU MEMS Center staff for their help, guidance in the cleanroom and the effort to keep the facility running.

I would like to thank to my dear friends; Ahmet Gülsaran, Bahar Atik, Baran Utku Tekin, Batuhan Beşcan, Buğrahan Gülcüler, Ebru Arslan, Emrah Dirican, Emre Ersoy, Gürel Dimez, Meltem Okan, Seval Şahin for being around me whenever I need.

I believe there are two crucial issues which make us lucky in life that we are limited in making decisions. They are the family we were born into and teachers who have a significant influence on us. I feel very fortunate on both and would like to thank my primary school teacher Dilek Ünsal.

Last but not least, I would like to thank my family for making me feel the luckiest person in the world. I am very grateful to my father, although no longer with us, continues to inspire me, Ercan, my mother Gülsevrim and my brother Erdem Şimşek for their endless love, encouragement, trust and support throughout my entire life.

## TABLE OF CONTENTS

ABSTRACT.....	v
ÖZ .....	vii
ACKNOWLEDGMENTS .....	x
TABLE OF CONTENTS.....	xi
LIST OF TABLES .....	xiii
LIST OF FIGURES .....	xiv
CHAPTERS	
1 INTRODUCTION .....	1
1.1 Overview of the MEMS Resonators .....	3
1.2 Overview of the Coupled Resonators .....	8
1.3 Overview of the MEMS Resonators Based Temperature Sensors .....	12
1.4 Objectives and Organization of the Thesis Study .....	16
2 DESIGN AND MODELLING OF THE DETF MEMS RESONATOR.....	19
2.1 Operation Principle of the MEMS Resonator .....	19
2.2 Analytical Modelling of DETF Resonant MEMS Load Cells.....	21
2.2.1 Capacitive Actuation .....	24
2.2.2 Capacitive Detection .....	26
2.2.3 Electrostatic Coupling Stiffness .....	27
2.2.4 Operation Principles of MEMS DETF Resonators as MEMS Temperature Sensor .....	27
2.3 Dynamic Model of the 2 Degree of Freedom DETF Resonator .....	29
2.4 Finite Element Analysis of Resonant MEMS Load Cells .....	37

2.4.1	Pull-in Voltage and Static Deflection Study for DETF Resonator .....	38
2.4.2	Mode Shape Analysis for the DETF MEMS Resonator .....	40
2.4.3	FEM Simulations of the Electrostatic Softening Effect.....	42
2.4.4	Finite Element Simulations of the Temperature Change.....	43
2.5	Summary.....	46
3	FABRICATION OF THE DESIGNED MEMS RESONATOR.....	47
3.1	Process Flow of the Sensor Structures .....	47
3.2	Fabricated DETF Resonators .....	53
3.3	Summary.....	54
4	TEST RESULTS .....	55
4.1	Frequency Response Characterization of the Resonators .....	55
4.1.1	Frequency Response Test Setup .....	55
4.1.2	Frequency Response Test Results.....	58
4.2	System-Level Test .....	60
4.2.1	System-Level Test Setup .....	61
4.2.2	System-Level Test Results.....	62
4.3	Summary.....	68
5	CONCLUSION AND FUTURE WORKS.....	71
	REFERENCES .....	75
	APPENDICES	
A.	Temperature Controller Algorithm with Proportional-Integral Controller .....	83

## LIST OF TABLES

### TABLES

Table 1-1. Sensitivity comparison of the state of the art resonant force sensors[35] .....	12
Table 2-1 Device parameters used in this study .....	21
Table 2-2.Parameters of the numerical analysis for the opposite proof mass voltage configuration using the geometrical parameter used in Table 2-1.....	36
Table 2-3.The first 8 mode shape simulation results obtained by COMSOL for VPM2=10V, VPM2=-10V.....	41

## LIST OF FIGURES

### FIGURES

Figure 1.1. Three basic types of vibration of mechanical resonators: flexural, torsional and bulk mode structures.[15] .....	3
Figure 1.2. The schematic view of the DETF structure.[5] .....	4
Figure 1.3. Schematic view of in-phase and out-of-phase mode shapes of a conventional DETF structure. ....	5
Figure 1.4. Schematic view of parallel plate(a) and comb-finger(b) configurations.	6
Figure 1.5. Quality factor illustration on a frequency response plot. ....	7
Figure 1.6. Schematic view of a DETF MEMS resonant temperature sensor with a strain-amplifying beam.[23] .....	7
Figure 1.7. The scheme of biaxial resonant accelerometer with two-stage micro leverage mechanisms.[20] .....	8
Figure 1.8. Optical images of the electrically-mechanically coupled resonators(a, b)[24], [30] and schematic view of the magnetically-mechanically coupled resonators[25] .....	9
Figure 1.9. Finite element simulation results for 3DoF balanced and mode localized by a tensile force resonators. [32].....	10
Figure 1.10. Loci of the dimensionless eigenvalues of the coupled resonators for the disorder in the tines[33].....	11
Figure 1.11. Schematic of the active oven control loop. The simplified oscillator circuitry is shown in grey colour.[45] .....	13
Figure 1.12. Schematic view of the Spring Resistor DETF resonator.[40].....	14
Figure 1.13. The schematic of the dual PLL circuit.[46] .....	14
Figure 1.14. The schematic view of two DETF resonator in closed-loop.[49] .....	15
Figure 2.1. The complete schematic of the DETF resonant system with drive and sense electrodes .....	20
Figure 2.2. The geometrical parameters used in design on the schematic view of the out of phase mode.....	24

Figure 2.3. Schematic view of the cross-section of the device under temperature change .....	28
Figure 2.4. A two degree of freedom representation for the system.....	29
Figure 2.5. Schematic view of the tines for pull-in voltage calculation and free body diagram. ....	31
Figure 2.6. The effect of the electrostatic coupling for various voltages on the axial force versus resonance frequency relation. ....	34
Figure 2.7. Stiffness ratio of the electrostatic coupling stiffness to effective stiffness with respect to proof mass voltage.....	37
Figure 2.8. Pull-in analysis performed by COMSOL Multiphysics .....	38
Figure 2.9. Applied voltage and corresponding static deflection analysis of tine resonator for +45V and -45V proof mass voltages.....	39
Figure 2.10. Displacement versus voltage graph of the endpoint of the capacitive tine.....	39
Figure 2.11. Deflection pattern of the electrostatic coupling electrode for different voltages. ....	40
Figure 2.12. The effect of the increasing proof mass voltage for the same proof mass voltage configuration where the single tine is utilized as the temperature sensor. .	42
Figure 2.13 The electrostatic softening effect due to the increasing proof mass voltage for the opposite sign proof mass voltage configuration. ....	43
Figure 2.14. Frequency change versus temperature change graphs obtained analytically for the same, and the opposite sign proof mass configurations.....	44
Figure 2.15 Frequency change versus temperature change graphs obtained by FEM results for the same proof mass configurations.....	44
Figure 2.16. Frequency change versus temperature change plot for opposite proof mass voltage configuration. ....	45
Figure 3.1. Cleaning step of the glass wafer. ....	48
Figure 3.2. Anchors on glass wafer formed with wet etching in HF solution. ....	48
Figure 3.3. Substrate wafer with anchors and metallization lines. ....	49
Figure 3.4. Precleaning of the SOI wafer is done in piranha and BHF solution.....	49

Figure 3.5. Formation of the resonant structures is done with DRIE.....	50
Figure 3.6. Anodic bonding of the substrate wafer and the SOI wafer. ....	50
Figure 3.7. Removal of the handle layer of the SOI wafer is processed by DRIE..	51
Figure 3.8. Removal of the buried oxide in BHF solution. ....	51
Figure 3.9. Optical microscopy photo of the device with wire bonds.....	52
Figure 3.10. The bottom view through the glass wafer. ....	52
Figure 3.11. SEM image of the fabricated device with the critical dimensions which are indicated in the box.....	53
Figure 4.1. Frequency response setup .....	56
Figure 4.2. Schematic view of the frequency response test setup for the single tine is utilized with the same proof mass configuration.....	57
Figure 4.3. Schematic view of the frequency response test setup for both tines is utilized with the opposite proof mass configuration. ....	57
Figure 4.4. Frequency Response Graph for $V_{PM1}=V_{PM2}$ .....	58
Figure 4.5. Frequency Response Graph for $V_{PM1}=-V_{PM2}$ .....	59
Figure 4.6. The close view of the frequency response plot to see the quality factor for the out-of-phase mode. ....	60
Figure 4.7. Schematic of the temperature controller setup with the device under test. .....	61
Figure 4.8. Frequency response plots for various temperatures for same proof mass configuration.....	63
Figure 4.9. System-level test result for DETF resonator for single tine where 10V proof mass voltages applied on both tines.....	63
Figure 4.10. System-level test result for DETF resonator for single tine where 20V proof mass voltages applied on both tines.....	64
Figure 4.11. Frequency response plots for various temperatures for opposite sign proof mass configuration.....	65
Figure 4.12. The system-level test result of DETF resonator for dual tines with the opposite proof mass configuration for the out-of-phase mode ( $V_{PM1}=10V$ , $V_{PM2}=-$ $10V$ ).....	65

Figure 4.13. The system-level test result of DETF resonator for dual tines with the opposite proof mass configuration for the in-phase mode ( $V_{PM1}=10V$ , $V_{PM2}=-10V$ ) .....	66
Figure 4.14. The system-level test result of DETF resonator for dual tines with the opposite proof mass configuration for the out-of-phase mode ( $V_{PM1}=20V$ , $V_{PM2}=-20V$ ) .....	66
Figure 4.15. The system-level test result of DETF resonator for dual tines with the opposite proof mass configuration for the in-phase mode ( $V_{PM1}=20V$ , $V_{PM2}=-20V$ ) .....	67
Figure 4.16. Temperature sensitivity versus proof mass voltage graph for the in-phase mode of opposite sign, out-of-phase mode of opposite sign and same sign proof mass voltage configurations.....	67



# CHAPTER 1

## INTRODUCTION

Humankind has measured quantities for agriculture, construction, trade and navigation purposes since around 3<sup>rd</sup> and 5<sup>th</sup> century BC. Over time, more accurate measurement is needed in order to develop new technologies, to ease life and to trade between nations on Earth. Starting with the 18<sup>th</sup> century, with the help of electricity developments and its applications, more standardized, universal and modern measurement techniques are developed[1]. New materials and their applications started to play a crucial role in developing technology. In the middle of the 19 hundreds, the utilization of the semiconductors started a new technology era with developments in integrated circuitry(IC) and the invention of the transistor. The dimensions of the technology did shrink in the following years very rapidly as parallel to Moore's observation [2]. Micro-sized devices combined with micro-sized electronics spread different applications which are an indispensable part of our lives and enabled more precise measurements with sophisticated appliances. The most recent review on applications and the future of the sensors is presented excellently by Zhu et al. [3] in areas, which have fast development rate nowadays. These areas can be listed as fifth-generation cellular network technology(5G), MEMS-NEMS devices, artificial intelligence (AI), virtual reality(VR) applications. The developed applications are widely used in consumer electronics, automotive industry, telecommunication, automation, military and healthcare. Accordingly, the market value of Micro-Electro-Mechanical Systems(MEMS) is around \$12B by 2019, and it is expected to grow with a 15% to 18% compound annual growth rate during the period of 2019 to 2025.[4].

MEMS sensors perform the measurements mainly by transduction between the mechanical, electrical, thermal, magnetic, chemical and radiative energy domains. After the invention of the transistor, researchers began developing miniaturized devices, which uses the conversion between these energy domains. The advantages of using these small devices are compatibility with IC fabrication, high repeatability, small size and high performance. However, there are still challenges like high power consumption of devices, 3-D integration difficulties, packaging cost and lack of advanced lithography techniques. Among the different types of sensors, it is seen that the resonant type of sensors is the most common type of sensors which are used extensively in many fields. In these fields, the sensors are used to measure different physical phenomena such as force[5], displacement, acceleration[6], angular velocity, magnetic field[7] etc.

In MEMS sensors, the most crucial drawback is the temperature-related performance deteriorations. In the literature, many studies are aiming to compensate for the performance degradation related to temperature effects. The temperature compensation can be done by designing the sensor with a minimum temperature dependency or measuring the exact temperature of the sensor and calibrating the sensor output using the temperature data. Both approaches are studied well by the researchers. High-performance applications are developed with having negligible temperature dependency. In addition to these applications, high sensitivity temperature sensors are utilized. In this thesis, the objective is obtaining a MEMS resonant temperature sensor with variable coupling stiffness, which enables us to increase the temperature sensitivity by adjusting the coupling stiffness, which also provides the mode-ordering.

In Section 1.1, a literature survey of resonant MEMS sensors is presented. Then, the coupled resonator approach and applications are introduced in Section 1.2. The various design approaches and the improvements are explained in details. In Section 1.3, the temperature detection mechanisms used in MEMS sensors are presented. Finally, the objectives and the organization of the theses are presented.

## 1.1 Overview of the MEMS Resonators

MEMS resonators are utilized in a wide range of sensor applications due to their simple operation principles and their superior advantages such as high stability, high sensitivity, compatibility with CMOS, high-quality factor, low cost of fabrication etc. After the MEMS resonator concept is proposed [8] and a relation between the resonance frequency and internal stress is formulated in vibrating cylinder pressure transducers[9] in the 1960s, remarkable progress has been made in the past decades in the improvement of micromachined resonant sensors[10]. Depending on the applications, which includes the acoustic, optical and photonic systems, different MEMS resonator types are utilized with various types of materials in different designs like flexural[11], [12], bulk[13], shear[14] and torsional mode resonators[7]. Figure 1.1 presents the different operational modes of the resonators widely used in the applications.

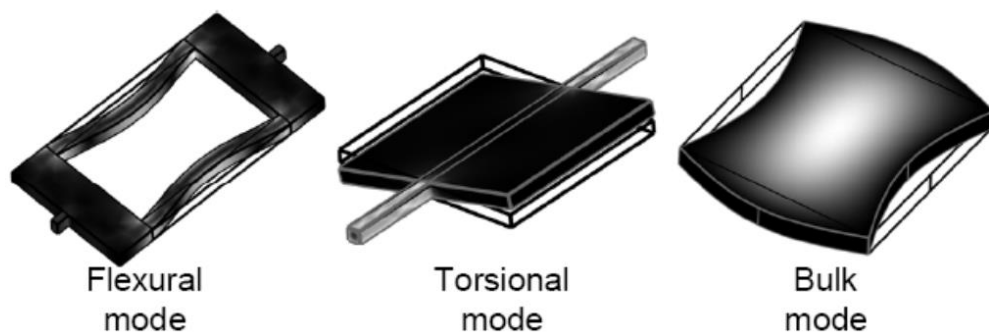


Figure 1.1. Three basic types of vibration of mechanical resonators: flexural, torsional and bulk mode structures.[15]

In the resonant sensor applications, physical phenomena are detected by using various sensing approaches. Utilization of advanced materials like piezoresistive and piezoelectric elements are available in the literature. Although these sensors have simple designs, high resolution and sensitivity, they have high power consumption, material dependent disadvantages. Moreover, optical and magnetic sensing methods are used in some sensor applications. In addition to the methods aforementioned,

capacitive sensing method is used in nearly 30% of the resonant sensors due to high sensitivity and resolution, large bandwidth, no drift and robustness.

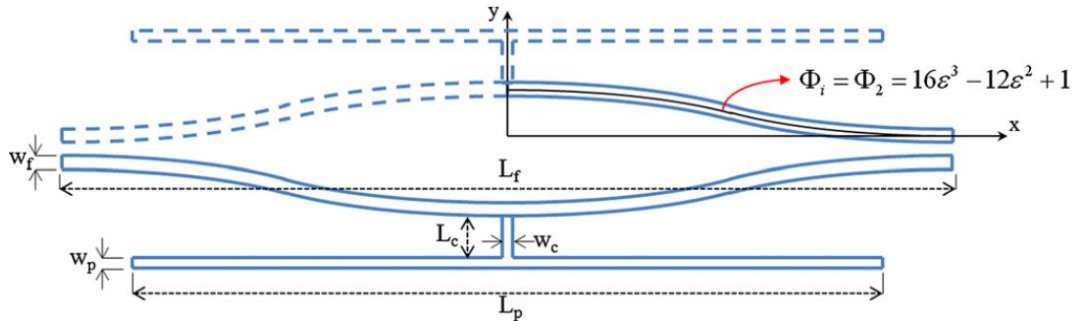


Figure 1.2. The schematic view of the DETF structure.[5]

In the feasible designs, it is proven that using more than one resonator increase the power of the output signal, enhances the frequency separation and decreases the phase noise in oscillators [16]. The sensing element used in this study is DETF resonator design, which has the two strain sensitive laterally vibrating tines as in Figure 1.2. The non-dimensionalized mode shape function of the half tine and corresponding resonance frequencies are studied well in the literature.[17] This design is a flexural mode resonator and uses the capacitive sensing method. The vibrating tines have two common modes of operation as illustrated in Figure 1.3, which are in-phase mode and out-of-phase mode, also known as symmetrical mode and antisymmetrical mode, respectively. The out-of-phase mode is preferred as the operational mode due to high tip stability and less anchor dissipation. Hence, energy storage within the system is better compared to the in-phase mode. Less anchor dissipation enhances the quality factor, which is explained in Figure 1.5. However, in the operation of the common DETF resonator, the in-phase mode frequency is lower than the out-of-phase mode frequency. Therefore, the in-phase mode is the limiting mode as the resonator operated close to the pull-in limit.

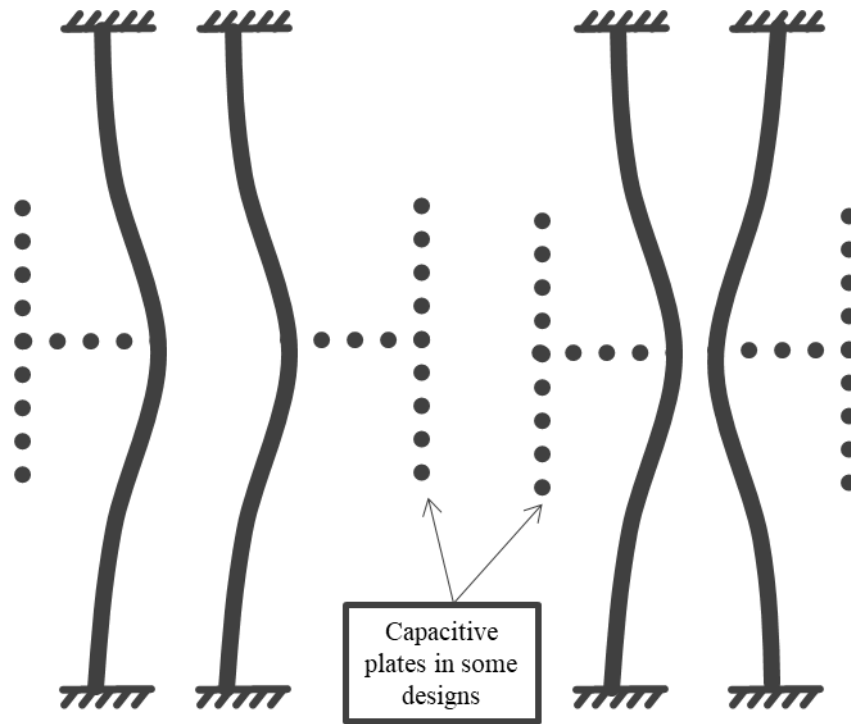


Figure 1.3. Schematic view of in-phase and out-of-phase mode shapes of a conventional DETF structure.

DETF MEMS resonant sensors are actuated and sensed with capacitively. The applied drive signal keeps the resonator at the resonance. The stimulus changes the resonance behaviour of the structure. By quantifying the capacitance change between the sense electrodes and the tines, the measurement is performed. In actuation and detection mechanisms, there are two different design, where the capacitance change occurs. The first method is the comb-finger configuration, in which the capacitance change takes place due to change in the overlap area or varying gap depending on the direction of the motion. This design, which is shown in Figure 1.4.b, can operate under both atmospheric and vacuum environment. At atmospheric pressures, sliding movement of the air creates some damping but does not suppress the motion of the resonator as is the parallel plate. The second design is the parallel plate configuration which is illustrated in Figure 1.4.a. In this configuration, capacitance change takes place resulting from the varying gap. At higher frequencies, the air between the parallel plates behaves like a spring. Therefore, the sensor should be operated under vacuum conditions due to air damping. The higher sensitivity can be obtained bu

using parallel plate compared to comb-finger design. However, the system is highly nonlinear. The crucial benefit of using the parallel plate configuration for this study is enabling the electrostatic coupling between the resonating tines by utilising the coupling electrodes.

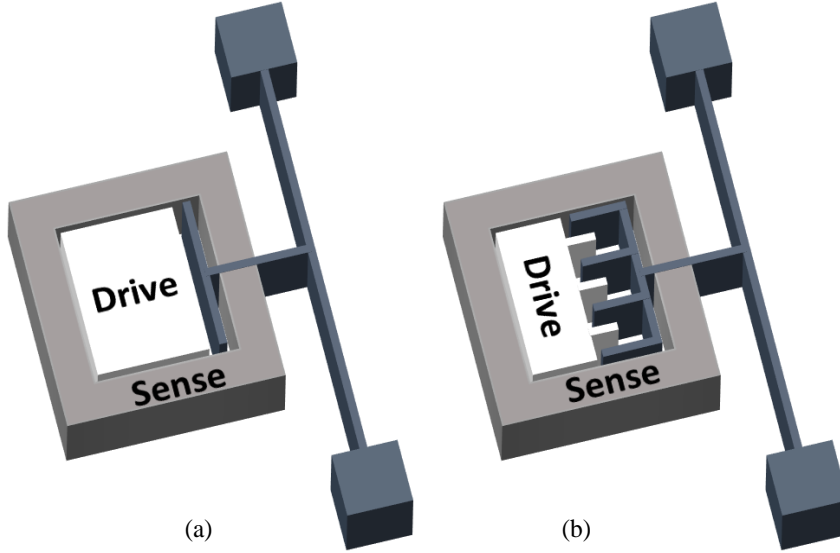


Figure 1.4. Schematic view of parallel plate(a) and comb-finger(b) configurations.

DETF resonators are used in the various sensor applications such as; force sensors[5], accelerometers[18], gyroscopes[19], magnetometer[20], pressure sensors[21], temperature sensors[22] etc. The studies on the resonant type of sensors focus on several ways of enhancing the performance of the sensors. One of the significant parameter for evaluating the performance of the resonator is the quality factor which is a dimensionless parameter. This term indicates how underdamped the system is. The term quality factor for a mechanical system is calculated by (1.1)

$$Q = \frac{\sqrt{km}}{b} = \frac{f_0}{f_2 - f_1} \quad (1.1)$$

where  $k$  is the stiffness,  $m$  is mass and  $b$  is the damping coefficient. In Figure 1.5, the quality factor refers to the ratio of the centre frequency to the half-power bandwidth, where the resonant structure loses half of its energy, or the resonance amplitude decreases 3 dB from the maximum amplitude.

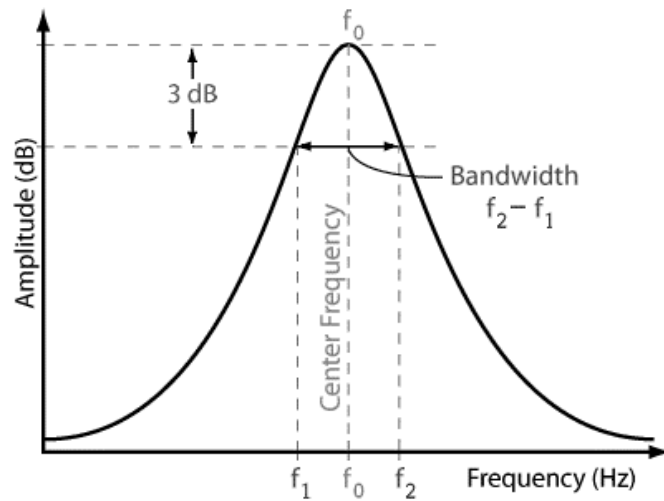


Figure 1.5. Quality factor illustration on a frequency response plot.

Another performance criterion is the scale factor or sensitivity, which is defined as the ratio between the output to input. In the literature, various approaches are used to enhance sensitivity. Leverage mechanisms are integrated into sensor structures to amplify the effect of the inputs as in Figure 1.6, to increase the sensitivity of the sensor. Biaxial resonators are used as the elements to be sampled differentially to increase the sensitivity of the sensors. Moreover, a combination of these methods can be used in a single device structure[6] as in Figure 1.7.

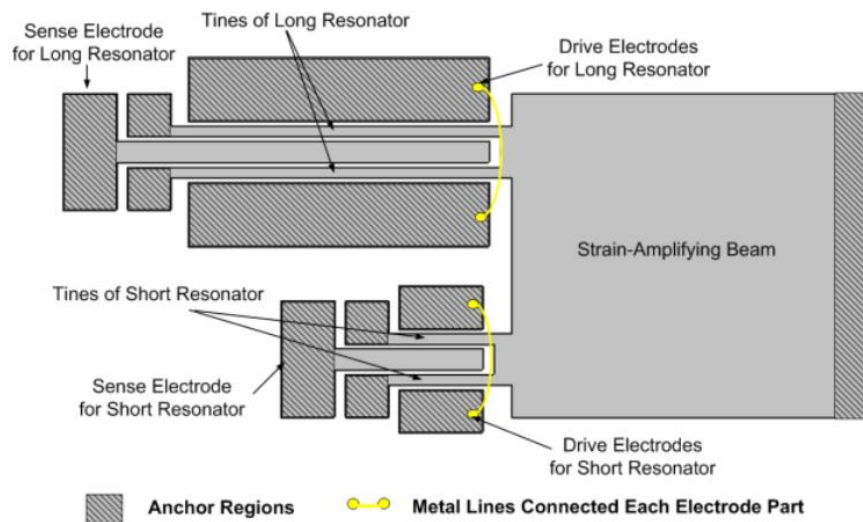


Figure 1.6. Schematic view of a DETF MEMS resonant temperature sensor with a strain-amplifying beam.[23]

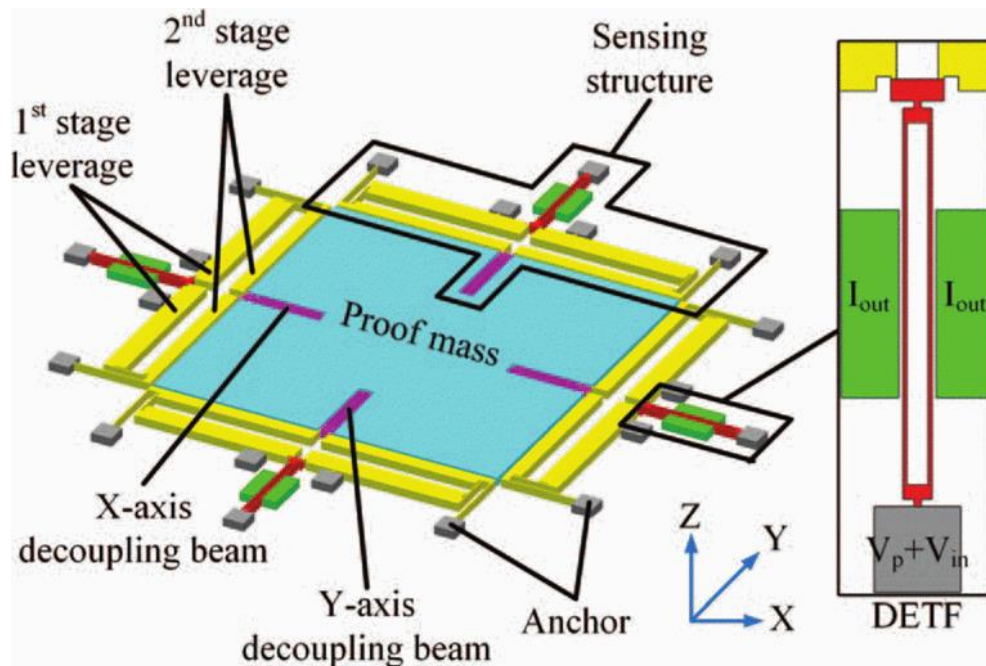


Figure 1.7. The scheme of biaxial resonant accelerometer with two-stage micro leverage mechanisms.[20]

The change in the resonance frequency or the resonance amplitude is used for the resonant characteristic generally. The change in the resonance frequency and amplitudes are detected by frequency modulation(FM) and amplitude modulation(AM) methods, respectively. Amplitude modulation suffers from a lack of stability in the vacuum environment. Therefore, frequency-modulated resonators are used more commonly despite the requirement for the complex circuitry. By adjusting the modulation frequency, resonance is kept at the desired mode.

## 1.2 Overview of the Coupled Resonators

Although most of the MEMS resonant sensors are modelled as 1 degree of freedom(DoF) resonator, which is acceptable in many applications, multi-degree of freedom (M-DoF) coupled MEMS resonators emerged recently as a new approach in sensor applications. Mechanical, electrical and magnetic couplings are used for

this purpose [24] [25]. In the first types of coupled resonators, the frequency shift is used as the output signal, and it is used in many sensor applications [26][27][28][29][30].

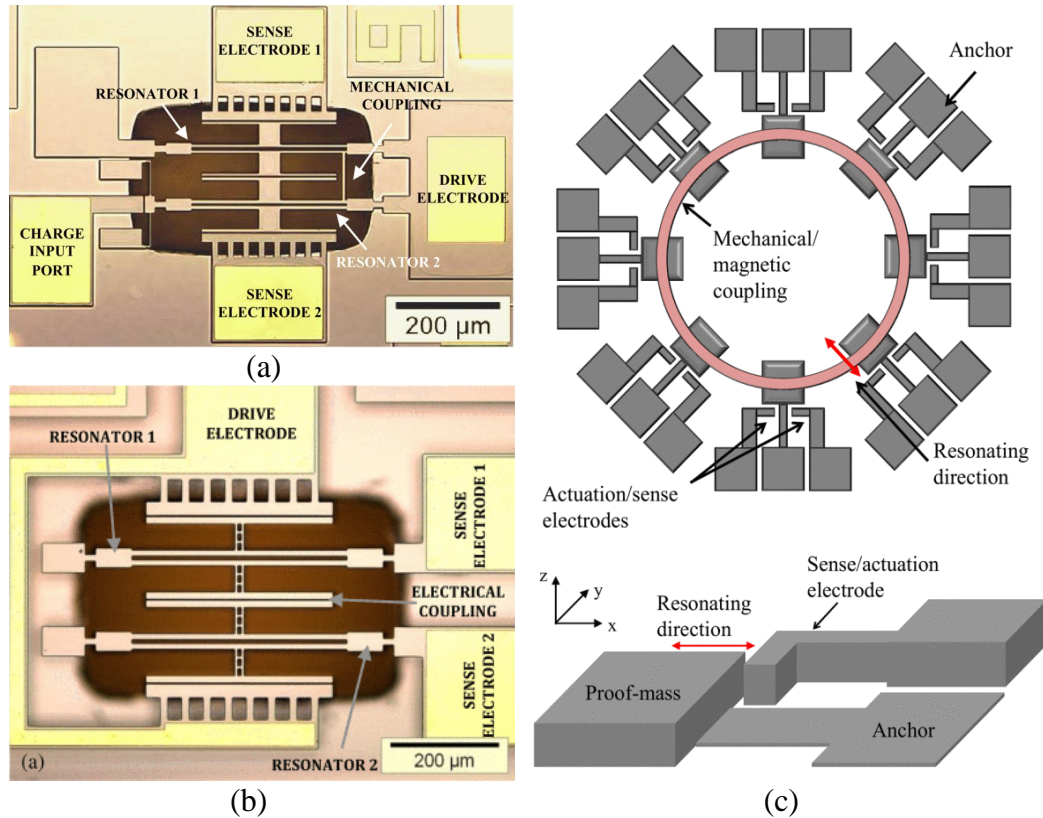
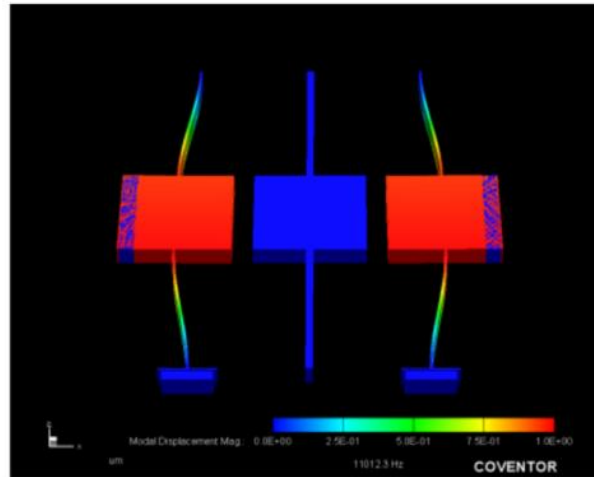


Figure 1.8. Optical images of the electrically-mechanically coupled resonators(a, b)[24], [30] and schematic view of the magnetically-mechanically coupled resonators[25]

Recently, being inspired by Anderson's work[31], a new approach to coupled resonators is established, which is called as mode localization. Mode localization occurs when a disturbance breaks the symmetry in the periodic systems and localizes the vibration into a tiny region as it is seen in Figure 1.5. The localized vibration is strongly dependent on the amplitude of the resonance.[32]. The usage of the M-DoF system has common-mode rejection capabilities, which diminishes the ambient temperature and pressure effects by comparing the mode-localized resonator and the other one.

Balanced situation



With positive stiffness perturbation on the left resonator

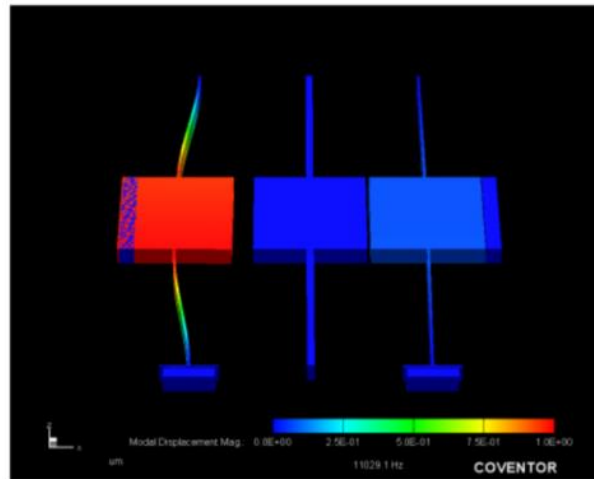


Figure 1.9. Finite element simulation results for 3DoF balanced and mode localized by a tensile force resonators. [32]

Moreover, in the case of mode localization, the eigenvalue curve veering is observed. When there is no disturbance, in other words, the system is perfectly symmetric, loci of the eigenvalues are closest to each other[33], as in Figure 1.10. In the presence of a disturbance on one of the resonators, the energy is localized on the disturbed resonator, as illustrated in Figure 1.9 The resonance behaviour change, which is an amplitude in most studies, is used as a detection mechanism. In these applications, the curve veering phenomena gets more effective as the coupling stiffness is reduced.[34]. It is also observed that, in these weakly coupled resonators, the effect of the coupling stiffness on the in-phase and the out-of-phase frequency change differs.

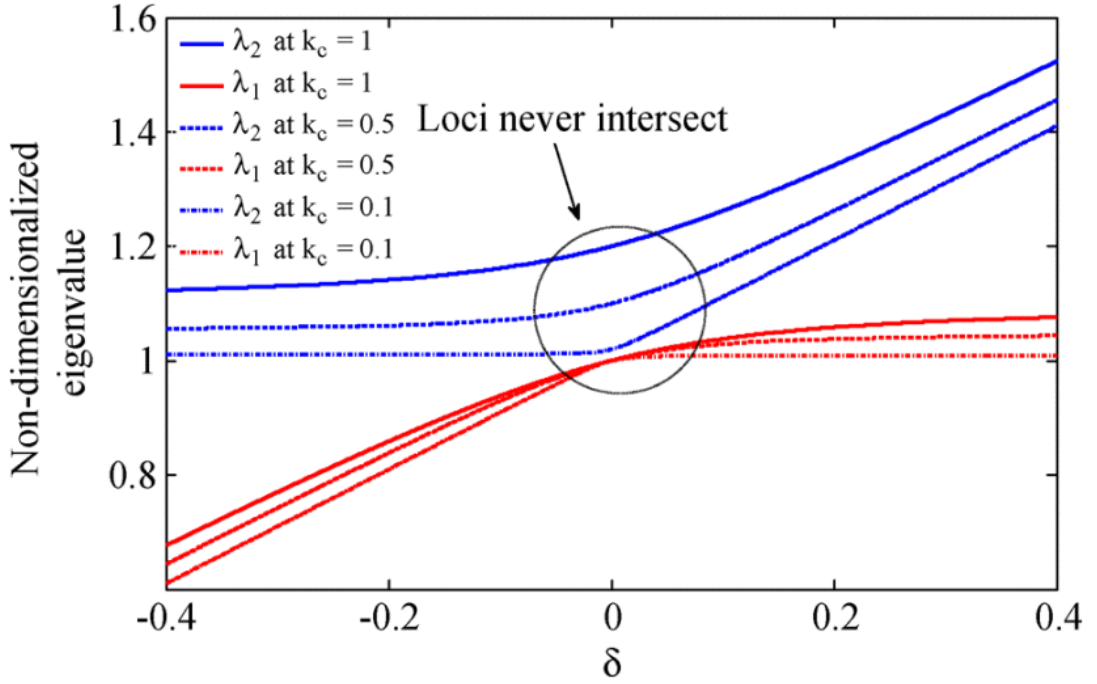


Figure 1.10. Loci of the dimensionless eigenvalues of the coupled resonators for the disorder in the tines[33].

In 2 DoF symmetric coupled resonant systems, which utilize the mode localization, the normalized sensitivity is increased by  $k / 2k_c$ , where the  $k$  is the stiffness and  $k_c$  is the coupling stiffness, for the weak coupling assumption, i.e.,  $k_c \ll k$ . When the coupling stiffness is two to three orders of magnitude smaller than the stiffness, the sensitivity improvement can be two to three orders of magnitude.[28]. Using the same mode localization approach for 3 DoF weakly coupled resonators, the sensitivity can be improved by at least two to three orders of magnitude.[29]. For comparison, the sensitivity expressions and sensitivity values are summarized in Table 1-1, which is explained in details in[35]. In this work, it is seen that using coupling for mode localization improves the parametric sensitivity and have the advantage of common-mode rejection. However, the initial tuning is required, and the resolution of the amplitude measurement is lower. Besides, although the mode localized sensors have excellent sensitivity, the applications, in which the self-oscillating loop are utilized, are still dominant due to fast detection of the varying stimulus.

Table 1-1. Sensitivity comparison of the state of the art resonant force sensors[35]

Type	Sensitivity Expression	Sensitivity	Ref
1DoF resonator with differential sensing and leverage	$\frac{\partial(\Delta f / f)}{\partial T}$	8995	[36]
2DoF resonant sensor	$\frac{\partial(EigenstateShift)}{\partial T}$	1478	[24]
3DoF resonator sensor	$\frac{\partial(AmplitudeRatio)}{\partial T}$	4.9x10 <sup>6</sup>	[29]

### 1.3 Overview of the MEMS Resonators Based Temperature Sensors

In timing applications[37] and the sensing applications, where MEMS-based resonators are used, the performance of the devices is strongly dependent on the temperature. In addition to long term changes like daily temperature differences, short term temperature differences affect the stability of the resonators, especially the ones which have very low thermal constants. Therefore, to eliminate the effect of temperature changes, systems should be designed to be least affected by this change or the exact temperature of the system should be known for compensation. There are numerous studies in the literature to overcome temperature compensation [38], [39]. Moreover, this problem leads researchers also to utilize the MEMS resonators as temperature sensors.

In the literature, there are different approaches for the temperature compensation found by researchers and excellently explained by Hopcroft [40]. The first temperature compensation method is the frequency tuning method. In this method, the temperature change is used as the compensator for the frequency change. This method includes both active and passive techniques, such as electrostatic tuning[41], reducing the thermal stress by using different materials[41], changing the linearity of the springs, using the orientation of the materials, controlling the temperature with ovens[42]–[45], frequency modulation with control circuitry[46] etc. Stabilization

of the resonator by keeping the temperature constant with heaters is one of the best methods, especially placing them as close as possible to the device. However, operating a micro oven is the major weakness of this method due to high power consumption.

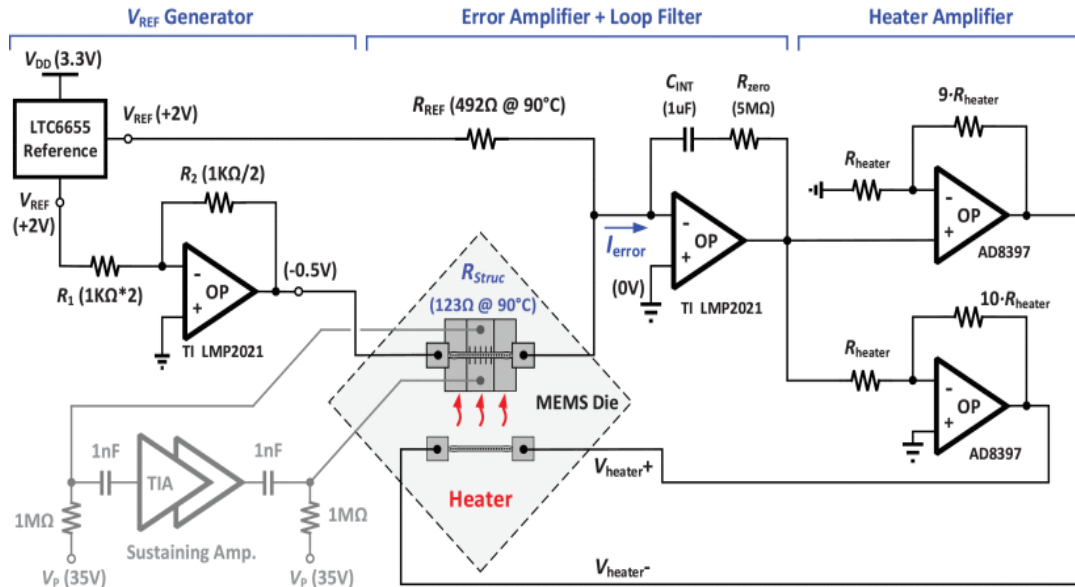


Figure 1.11. Schematic of the active oven control loop. The simplified oscillator circuitry is shown in grey colour.[45]

Hopcroft states that to achieve the best frequency stability, a MEMS resonator should be fabricated with thermal isolation, heating and temperature sensing elements[40]. A DETF resonator with spring resistor configuration as in Figure 1.12, which provides joule heating, thermal and mechanical isolation, sensed with dependency between the quality factor and temperature would give the best result. Therefore, it is clear that measuring the temperature within the system is a crucial part of the novel devices.

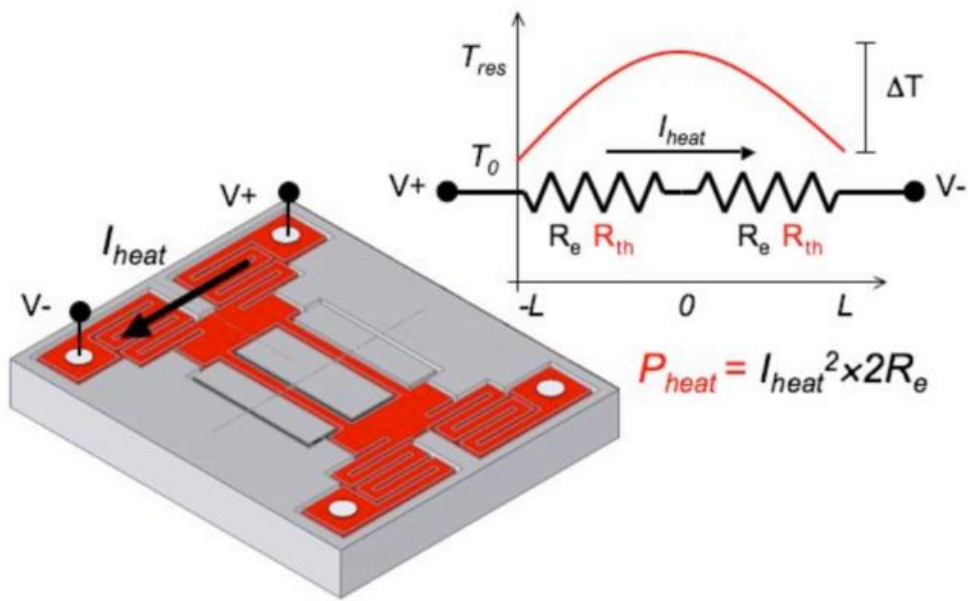


Figure 1.12. Schematic view of the Spring Resistor DETF resonator.[40]

Another solution to temperature compensation is sensor utilization of the electronic circuits. Although passive methods, like stress compensation and using composite materials, which have a close thermal coefficient of expansion(TCE), are available in the literature, they have disadvantages such as hysteresis and fabrication complications. However, with the possible control system as in Figure 1.13, where control loops are utilized, high-performance sensors can be obtained by relating the temperature and the system output, i.e., current or voltage, to compensate the temperature drifts or to measure the temperature.[46]–[48]

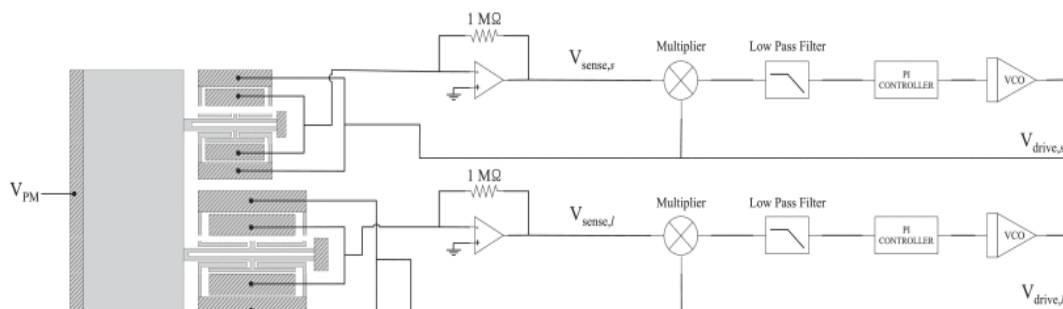


Figure 1.13. The schematic of the dual PLL circuit.[46]

The application of DETF resonator as a temperature sensor can be seen in [38], [49], [50]. In this study [50], the temperature coefficient of frequency(TCf) sensitivity and resolutions are reported as -31ppm/K and 10mK. Integration of the resonant temperature sensor into a pressure sensor is the novelty. However, the sensitivities are similar to standard DETF resonators. In [49], two DETF resonators are utilized with closed-loop, as in Figure 1.14. The resolution and the TCf sensitivity are 0.008°C and -570ppm/K for this study. The dual-resonator design, which can also be used with CMOS applications, generates temperature-dependent beat frequencies to eliminate the effect of thermal lag and static temperature gradients.

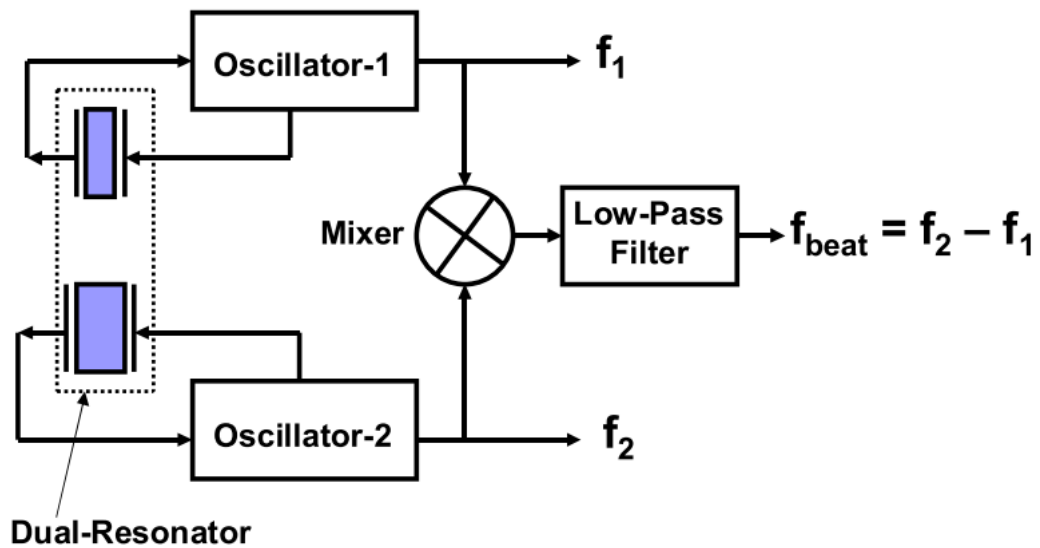


Figure 1.14. The schematic view of two DETF resonator in closed-loop.[49]

In [51], CMOS based temperature sensors are presented in detail. In these applications, very high performance temperatures sensors can be obtained. In this study [52], which is a state of the art, presents a 40 $\mu$ K resolution utilizing a dual-MEMS resonator. However, they can not be mounted next to MEMS sensors. Therefore, the exact temperature of the MEMS sensor can not be measured due to thermal lag. Thus, the actual temperature measurement of the MEMS sensor is crucial, and the integration of the temperature sensor within the system gives the best result.

## 1.4 Objectives and Organization of the Thesis Study

There is an increasing demand for MEMS devices due to their advantages such as small size, less power consumption, easy integration with IC. The novel applications require high-performance devices. Temperature is one of significant effect on this performance. Therefore, measurement of the temperature in the applications like MEMS sensors is very crucial to minimize the impact on the sensor performance. The aim of this thesis is to propose a MEMS resonant temperature sensor with variable coupling stiffness, which enables us to increase the temperature sensitivity by adjusting the coupling stiffness, which also provides the mode-ordering. The specific objectives of this study are;

- Development of an electrostatically coupled DETF MEMS resonant temperature sensor, which uses the thermal coefficient expansion difference of the materials used in the structure with high sensitivity and high dynamic range.
- The operation principles of the resonant temperature sensor and methods to improve the sensitivity is explained with the analytical models. Thermo-electro-mechanical model is derived for the design used in this thesis. The actuation and detection mechanisms used on the resonators is presented.
- Finite element simulations are performed to validate the analytical model. Mechanical, electro-mechanical and thermo-electro-mechanical simulations are compared with the analytical model considering the resonance frequencies, electrostatic and thermal effects.
- Fabrication of the sensor structure and test results are presented. The methods and test setups used in the characterization of the sensor is given. Frequency response tests are performed for validation of electro-mechanical and thermo-electro-mechanical models for analytical and FEM models.

Chapter 2 presents the design and modelling of the double-ended tuning fork (DETF) resonator as a temperature sensor. The working principle of the sensor design is

explained in detail with the governing equations. The actuation, sensing and the electrostatic coupling mechanisms are presented. Finite element simulations are conducted and verified with the analytical model. The effect of temperature and proof mass voltage on the resonance frequency of the mode of interests, which are in-phase mode and out of phase mode are simulated and compared with the analytical model.

Chapter 3 presents the fabrication of the sensor structure. Process flow of the fabrication steps is illustrated briefly. The fabrication results are presented. The reasons for the difference between the design and the fabricated sensor dimensions are discussed.

In Chapter 4, the characterization of the electrostatically coupled DETF sensor structure is presented. The experimental test setup used in the characterization is explained in details. The frequency response test results are compared with the electro-mechanical model and finite element simulation results. For the system level tests, the effect of the temperature on the resonance frequencies using the frequency response plots is compared with thermo-electro-mechanical model and finite element simulations. The possible reasons for the difference between the test results and the models are discussed.

As the final chapter, Chapter 5 concludes the obtained results during this study. Recommendations and future work to develop this design is presented.



## CHAPTER 2

### DESIGN AND MODELLING OF THE DETF MEMS RESONATOR

In this chapter, the design and modelling of the double-ended tuning fork MEMS resonator are presented. In MEMS structures, due to Moore's Law, all phenomena play an essential role, and each effect should be considered carefully. The interaction between the electrical, mechanical and thermal energy domains are considered for the analysis. Section 2.1 introduces the operation principles of MEMS resonators briefly. In Section 2.2, the theory about MEMS resonator is presented. Then, the governing equations of the system, electrostatic actuation and detection principles are explained. After that, the electrostatic coupling between the tines and its effect on the resonance is demonstrated. In Section 2.3, the dynamics of the DETF resonator structure is studied as two degrees of freedom system. In Section 2.4, Finite Element Analysis(FEM) results are presented to validate the analytical model. In this section, pull-in, static deflection and modal analyses are explained.

#### 2.1 Operation Principle of the MEMS Resonator

The applications of the resonant based MEMS sensors are explained in Chapter 1. Considering the advantages such as wide measurement range, high sensitivity, and the compatibility with CMOS, DETF resonator-based MEMS sensors appear as a promising element and are studied in many of the previous studies. Besides, utilization of this structure with other MEMS devices, such as force sensor, accelerometer, gyroscopes, prevents the thermal lag and gives the exact temperature for the temperature compensation of the devices.

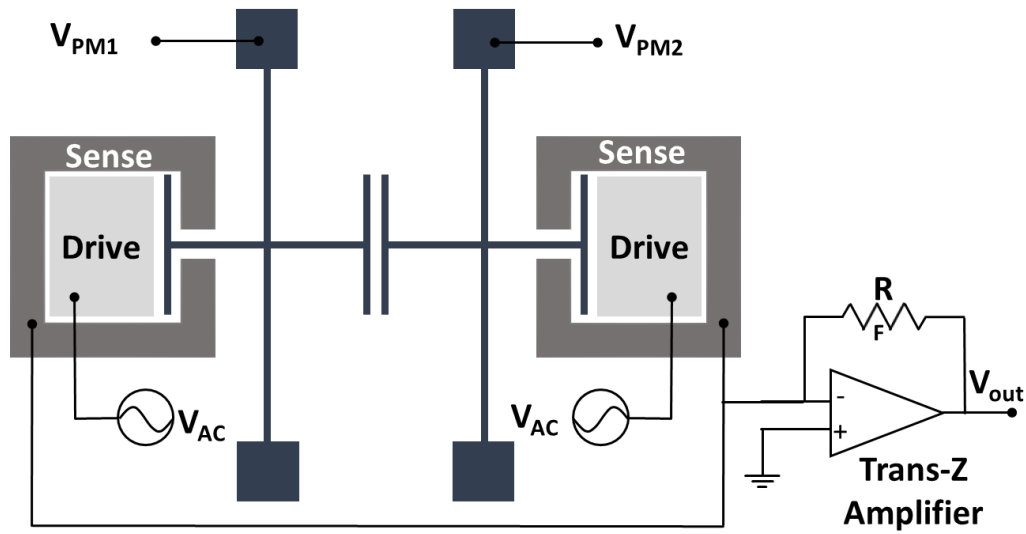


Figure 2.1. The complete schematic of the DETF resonant system with drive and sense electrodes

The design of the DETF resonant element used in this study is shown in Figure 2.1. The tines have 2 capacitive plates on each side. The outer plates of tines are used for the capacitive actuation and capacitive sensing whose operating principles are explained in Section 2.2.1 and 2.2.2. The inner capacitive plates at the centre are used for the electrostatic coupling between tines. This electrostatic coupling serves as a negative spring and the most crucial part of this study. This spring enables the mode-ordering, which is explained in Section 2.2.3. These resonators are operated at their resonance frequency by applying the AC drive signal with the same frequency. In the presence of external disturbance, the resonance frequency of the resonator changes and the device can be used as a sensor. The detail of the utilization of the resonator as a temperature sensor and the operation principle is given in Section 2.2.4 Table 2.1 summarizes the parameters used in the design and shown in Figure 2.2. Although Young's modulus of the material is a temperature-dependent property, in this study, it is taken as a constant parameter to simplify the calculations. This effect can be found in the literature[53].

Table 2-1 Device parameters used in this study

<b>Parameter</b>	<b>Symbol</b>	<b>Value</b>
Tine Length	$L_f$	500 $\mu\text{m}$
Tine Width	$W_f$	10 $\mu\text{m}$
Capacitive Plate Length	$L_p$	320 $\mu\text{m}$
Capacitive Plate Width	$W_p$	10 $\mu\text{m}$
Connector Length	$L_c$	120 $\mu\text{m}$
Connector Width	$W_c$	10 $\mu\text{m}$
Device Thickness	$h$	35 $\mu\text{m}$
Gap	$g$	2 $\mu\text{m}$
Young's modulus for (111) Si	$E_{Si}$	170 GPa
The density of the Si	$\rho$	2330kg/m <sup>3</sup>
Vacuum Permittivity	$\epsilon_0$	8.85x10 <sup>-12</sup> F/m
Proof Mass Voltage for tine 1	$V_{PM1}$	10V(variable)
Proof Mass Voltage for tine 2	$V_{PM2}$	-10V(variable)
Trans-Z feedback resistance	$R_f$	1M $\Omega$
Thermal Expansion Coeff. Of Silicon[54]	$\alpha_{Si}$	2.59x10 <sup>-6</sup> 1/K
Thermal Expansion Coeff. Of Glass	$\alpha_g$	3.25x10 <sup>-6</sup> 1/K

## 2.2 Analytical Modelling of DETF Resonant MEMS Load Cells

For the analytical model, the equation of motion for a beam under an axial load is derived using Euler-Bernoulli beam theory in [55] to find the lumped mass and effective spring constants. In this approach, there are some assumptions;

- Shear deformations are neglected. In other words, the cross-section is assumed to remain parallel since the resonator plate thickness is very small compared to other dimensions.
- Rotary inertia is neglected.
- The beam is uniform.
- Material property is same every point in the volume, which means isotropic.
- There is no structural damping within the system.

Following these assumptions, the equation of the motion for the transverse vibration of the beam subjected to axial force is,

$$\frac{\partial^2}{\partial x^2} \left( EI \frac{\partial^2 w(x,t)}{\partial x^2} \right) + \frac{\partial}{\partial x} \left( F \frac{\partial w(x,t)}{\partial x} \right) + \rho A \frac{\partial^2 w(x,t)}{\partial t^2} = P(x,t) \quad (2.1)$$

where  $w$  is the deflection of the beam in the  $y$ -direction,  $E$  is the modulus of elasticity,  $I$  is the moment of inertia of the beam,  $F$  is the axial force applied to the beam,  $\rho$  is the material density,  $A$  is the cross-section area of the beam and  $P(x,t)$  is the transverse force applied to the beam. For a clamped-clamped beam, the boundary conditions are no deflection and no slope at the end of the beams.

$$\begin{aligned} w(0) = w(L) = 0 \\ \left. \frac{dw}{dx} \right|_{x=0} = \left. \frac{dw}{dx} \right|_{x=L} = 0 \end{aligned} \quad (2.2)$$

Assuming the unforced vibration, where  $P = 0$  is everywhere and including all the point masses as the inertial forces distributed along the beam,

$$P = \sum_j m_j \ddot{w}(x_j) \delta(x_j) \quad (2.3)$$

The differential equation is solved by the separation of variables method.

$$w(x,t) = \sum_i q_i(t) \phi_i(\varepsilon) \text{ where } \varepsilon = \frac{x}{L} \quad (2.4)$$

The solution in general form is;

$$M_{eff}\ddot{q} + c\dot{q} + K_{eff}q = P(t) \quad (2.5)$$

where  $M_{eff}$  is the effective mass,  $c$  is the damping coefficient and  $K_{eff}$  is the effective spring constant. The terms in the governing equation can be taken as inertia and stiffness terms as,

$$M_{eff} = \rho AL \int_0^1 \phi_i^2 d\varepsilon + \sum_j m_j \left( \phi_i(\varepsilon_j) \right)^2 \quad (2.6)$$

$$K_{eff} = \frac{EI}{L^3} \int_0^1 \left( \frac{d^2 \phi_i}{d\varepsilon^2} \right)^2 d\varepsilon + \frac{F}{L} \int_0^1 \left( \frac{d\phi_i}{d\varepsilon} \right)^2 d\varepsilon \quad (2.7)$$

$$c = \sqrt{\frac{K_{eff} M_{eff}}{Q}} \quad (2.8)$$

Using the above equations and by applying the normalized mode shape function for any given mode into the equation, the effective mass and effective spring constants which are used to find the natural frequency of the mode is derived. In this study, the system is modelled as an undamped system, since the resonator is operated under vacuum. Therefore, the undamped and damped frequencies are very close to each other. Besides, the capacitive plates on each side of the centre tines are assumed to be rigid and connected to the centre of the tine since the vibration amplitudes are very small. For a clamped-clamped beam under a point load at its centre, the normalized mode shape function for half tine, whose schematic is given in Figure 2.2, can be taken as,

$$\phi(\varepsilon) = 16\varepsilon^3 - 12\varepsilon^2 + 1 \quad (2.9)$$

After applying the non-dimensionalized mode shape into effective mass and effective spring constant equations, the simplified term are obtained as below.

$$M_{eff} = \frac{13}{35} \rho w_f L_f + 2\rho (w_c L_c + w_p L_p) \quad (2.10)$$

$$K_{eff} = 192 \frac{EI}{L_f^3} + 2.4 \frac{F_{app}}{L_f} \quad (2.11)$$

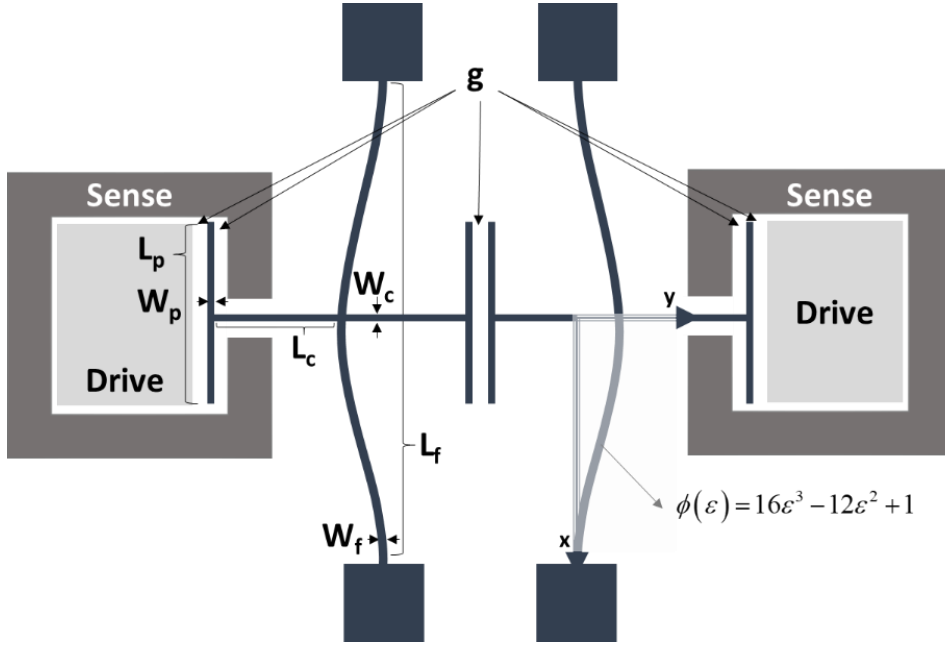


Figure 2.2. The geometrical parameters used in design on the schematic view of the out of phase mode

For an undamped system, the resonance frequency of a single tine anchored from one end and an axial force applied from the other end for the given mode will be,

$$\omega_n = \sqrt{\frac{K_{eff}}{M_{eff}}} = \sqrt{\frac{192 \frac{EI}{L_f^3} + 2.4 \frac{F_{app}}{L_f}}{\frac{13}{35} \rho w_f L_f + 2\rho(w_c L_c + w_p L_p)}} \quad (2.12)$$

### 2.2.1 Capacitive Actuation

The system is kept at the desired resonance mode by exciting with an alternating current(AC) signal, whose frequency is the same with the resonance frequency of the DETF resonator. The driving signal is applied from the drive electrodes. This alternating current signal creates an electrostatic force between the drive electrode and the capacitive plate and excites the system. The change in the stored electrostatic energy between the capacitive plate and the drive electrode is used to find the

excitation the force. Neglecting the fringing field effect on edges of the capacitive plates and assuming these plates are rigid, the energy stored between the parallel plate and the drive electrode is,

$$E = \frac{1}{2} CV^2 \quad (2.13)$$

where  $V$  is the applied voltage difference,  $C$  is the capacitance between the capacitive plate of the resonator and drive electrode. The capacitance is found by

$$C = \frac{\epsilon_0 A}{g} \quad (2.14)$$

Where the  $\epsilon_0$  is the vacuum permittivity assuming the system operates in vacuum conditions.  $A$  is the overlap area of the resonator plate and the drive electrode which is proportional to tine length  $L_p$  and the thickness of the device  $h$ .  $g$  is the gap between the resonator plate and the drive electrode. As the system vibrates, the energy stored between the parallel plates changes since the gap changes. As the tine of the resonator moves by  $x$ , the energy stored in the capacitance will be,

$$E = \frac{1}{2} CV^2 = \frac{1}{2} \frac{\epsilon_0 L_p h}{(g+x)} (V_{PM} - V_{AC})^2 \quad (2.15)$$

where  $V_{AC} = v_{ac} \sin(\omega t)$  is the applied voltage for the excitation After taking the derivative of stored energy with respect to displacement, the electrostatic force is calculated between the plates as,

$$F_D = \frac{\partial E}{\partial x} = -\frac{1}{2} \frac{\epsilon_0 L_p h}{(g+x)^2} \left\{ \underbrace{\left( \frac{v_{ac}^2}{2} + V_{PM}^2 \right)}_{\text{DC Term}} - \underbrace{(2V_{PM} v_{ac} \sin(\omega t))}_{\text{Sinusoidal Term}} - \underbrace{\frac{1}{2} (v_{ac}^2 \cos(2\omega t))}_{\text{Double Frequency Term}} \right\} \quad (2.16)$$

The applied AC voltage is very small, and the double frequency term is filtered, so they are neglected. The forcing term is,

$$F_D = -\frac{1}{2} \frac{\epsilon_0 L_p h}{(g+x)^2} \left\{ V_{PM}^2 + \frac{v_{ac}^2}{2} - 2V_{PM} v_{ac} \sin(\omega t) \right\} \quad (2.17)$$

Moreover, the vibration amplitude is very tiny compared to the gap. After eliminating the terms according to the above assumption and taking one more derivative with respect to displacement, the electrostatic spring constant can be found as,

$$k_D = -\frac{\varepsilon_0 L_P h}{g^3} V_{PM}^2 \quad (2.18)$$

### 2.2.2 Capacitive Detection

The detection mechanism is driven by the movement of the mass by the electrostatic forces. As the tine moves, the capacitance changes between capacitive tine and sense electrode, therefore an alternating current is induced on the sense electrode with the same frequency of the resonance. Employing a trans-impedance-amplifier(TIA), the induced current created by moving charges is converted to the voltage and is fed to the circuitry. The induced alternating current is found by taking the derivative of the charge between the plates with respect to time.

$$i = \frac{\partial q}{\partial t} = \frac{\partial (CV_{DC})}{\partial t} = \frac{\partial C}{\partial x} \frac{\partial x}{\partial t} V_{DC} + (\dot{V}_{DC}) C = \frac{\partial C}{\partial x} \dot{x} V_{DC} = -\frac{\varepsilon_0 L_P h}{g^2} \dot{x} V_{DC} \quad (2.19)$$

Assuming the capacitive tine motion is defined as  $x = A \sin(\omega t)$  and putting into the equation below, the output of the trans-impedance amplifier,

$$V_{out} = i R_f = -\frac{\varepsilon_0 L_P h}{g^2} (A \omega \cos(\omega t)) V_{DC} R_f \quad (2.20)$$

where  $R_f$  is the feedback resistance used in the circuitry.

### 2.2.3 Electrostatic Coupling Stiffness

In the resonator used in this study, there is an electrostatic coupling stiffness between the inner capacitive plates of the tines. This spring behaves as a negative spring and can be defined with a similar approach. In this case,

$$F_{elect} = -\frac{1}{2} \frac{\varepsilon_0 L_p h}{(g - x_1 + x_2)^2} \{V_{PM1} - V_{PM2}\}^2 \quad (2.21)$$

Assuming that the displacement magnitudes are the very small, same in magnitude but in the opposite directions. The spring constant between the tines is,

$$k_{elect} = -\frac{\varepsilon_0 L_p h}{g^3} (V_{PM1} - V_{PM2})^2 \quad (2.22)$$

Note that, the forces on a single tine applied by the drive electrode and electrostatic coupling are in the opposite directions. So, assuming the displacements are very small, the total force on a single tine is,

$$F_t = F_D + F_{elect} = -\frac{1}{2} \frac{\varepsilon_0 L_p h}{g^2} \left\{ V_{PM1}^2 + \frac{V_{ac}^2}{2} - 2V_{PM1}V_{ac} \sin(\omega t) \right\} + \frac{1}{2} \frac{\varepsilon_0 L_p h}{g^2} \{V_{PM1} - V_{PM2}\}^2 \quad (2.23)$$

The equation of motion for the single tine 1 including all terms is,

$$M_{eff} \ddot{x} + C_{eff} \dot{x} + K_{eff} x = F_D + F_{elect} = \dots -\frac{1}{2} \frac{\varepsilon_0 L_p h}{(g + x_1)^2} \left\{ V_{PM}^2 + \frac{V_{ac}^2}{2} - 2V_{PM}V_{ac} \sin(\omega t) \right\} + \frac{1}{2} \frac{\varepsilon_0 L_p h}{(g + x_1 - x_2)^2} \{V_{PM1} - V_{PM2}\}^2 \quad (2.24)$$

### 2.2.4 Operation Principles of MEMS DETF Resonators as MEMS Temperature Sensor

In this study, the DETF fork resonator is anchored from both ends. The resonance frequency of the resonator and the force sensitivity depends on the axial force on the resonator. For this design, the axial force is induced by the thermal strain on the sensor structure. The difference in the thermal expansion coefficients of the resonator structure and substrate materials results in thermal stress and an axial force when

there is a temperature change. In this design, thermal expansions on the cross-sections and the capacitive gaps are neglected since the width of the resonator is very small compared to the length of the resonator and tiny gap. The schematic view of the cross-section of the sensor structure is given in Figure 2.3.

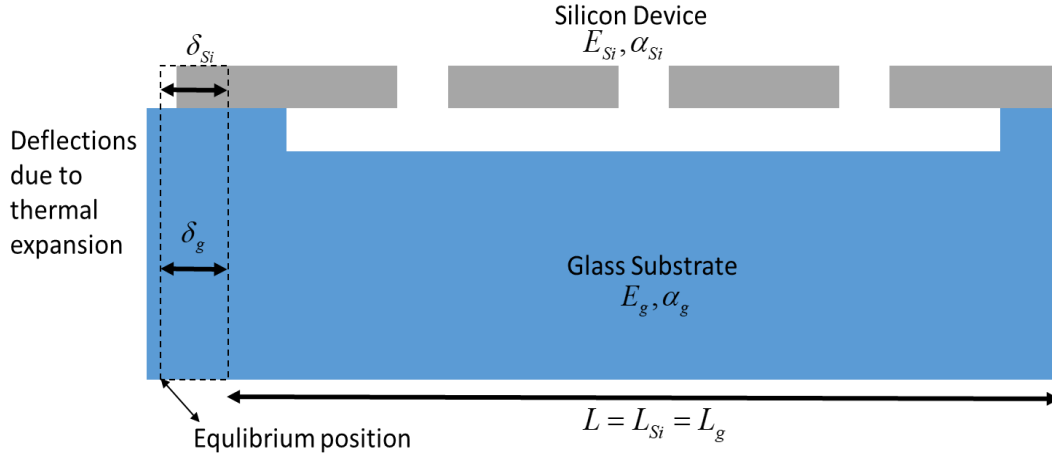


Figure 2.3. Schematic view of the cross-section of the device under temperature change

The axial force on the resonator tines is written by the thermal strain equation clamped from both ends to the glass substrate, as stated in[23]. However, in this design, there is no cap wafer, which affects the strain as in the study mentioned above.

$$\delta_f = L_f (\alpha_g - \alpha_{Si}) \Delta T \quad (2.25)$$

Where the length of the resonator  $L_f$  and the distance between the anchor points are the same.  $\alpha_{Si}$  and  $\alpha_g$  stand for the thermal expansion coefficients of the silicon and the glass substrate. Since the resonant structure is anchored from both ends, the strain terms will also be the same. Hence, the thermally induced force applied to the resonator is obtained by,

$$F_{app} = (\alpha_g - \alpha_{Si}) \Delta T E_{Si} A_{Si} \quad (2.26)$$

As it is seen from the equation above, the axial force term applied to the resonator is temperature-dependent. Therefore, the resonance frequency of the resonator is affected by the temperature change due to stress induced by the thermal expansion coefficient difference of the glass substrate and the device.

### 2.3 Dynamic Model of the 2 Degree of Freedom DETF Resonator

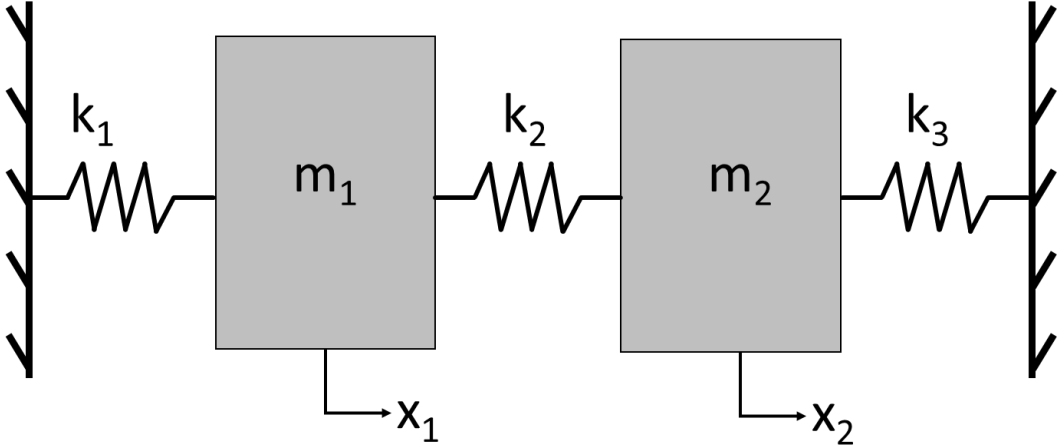


Figure 2.4. A two degree of freedom representation for the system.

The schematic of the lumped model of the two degrees of freedom system is given in Figure 2.4. The equation of motion for a single tine is utilized for the two tines. For the lumped model, assuming there is no damping since the resonator is operated in a vacuum chamber, the matrix form of the given system is,

$$[M]\{\ddot{x}\} + [K]\{x\} = \{0\}$$

$$\begin{bmatrix} m_1 & 0 \\ 0 & m_2 \end{bmatrix} \begin{bmatrix} \ddot{x}_1 \\ \ddot{x}_2 \end{bmatrix} + \begin{bmatrix} k_1 + k_2 & -k_2 \\ -k_2 & k_2 + k_3 \end{bmatrix} \begin{bmatrix} x_1 \\ x_2 \end{bmatrix} = \begin{bmatrix} 0 \\ 0 \end{bmatrix} \quad (2.27)$$

where stiffnesses shown in the above equation are,

$$k_1 = k_{1eff} + k_{D1} = 192 \frac{EI}{L_f^3} + 2.4 \frac{F_{app}}{L_f} - \frac{\epsilon_0 L_P h}{g^3} V_{PM1}^2 \quad (2.28)$$

$$k_2 = k_c + k_{elec} = k_c - \frac{\varepsilon_0 L_p h}{g^3} (V_{PM1} - V_{PM2})^2 \quad (2.29)$$

$$k_3 = k_{2eff} + k_{D2} = 192 \frac{EI}{L_f^3} + 2.4 \frac{F_{app}}{L_f} - \frac{\varepsilon_0 L_p h}{g^3} V_{PM2}^2 \quad (2.30)$$

where  $k_c$  is mechanical coupling stiffness at the endpoints for each tine. However, this term is negligibly small compared to the electrostatic coupling stiffness, which is a dominant parameter for this study. Assuming  $x = \{u\} e^{i\omega t}$  is a solution for the system and putting into the equation.

$$\begin{aligned} -\omega^2 [M] \{u\} e^{i\omega t} + [K] \{u\} e^{i\omega t} &= \{0\} \\ \underbrace{[[K] - \omega^2 [M]]}_{\text{This term will be zero}} \{u\} e^{i\omega t} &= 0 \end{aligned} \quad (2.31)$$

By solving the above equation to find the non-trivial solution,

$$(k_1 + k_2 - \omega^2 m_1)(k_2 + k_3 - \omega^2 m_2) - (k_2)^2 = 0 \quad (2.32)$$

Expanding the equation and rearranging the terms,

$$\underbrace{m_1 m_2 \omega^4}_A - \underbrace{(m_1(k_2 + k_3) + m_2(k_1 + k_2))\omega^2}_B + \underbrace{k_1 k_2 + k_1 k_3 + k_2^2 + k_2 k_3 - k_2^2}_C = 0 \quad (2.33)$$

$$\underbrace{m_1 m_2 \omega^4}_A - \underbrace{(m_1(k_2 + k_3) + m_2(k_1 + k_2))\omega^2}_B + \underbrace{k_1 k_2 + k_1 k_3 + k_2 k_3}_C = 0 \quad (2.34)$$

The modal frequencies are found as follows.

$$\omega_{1,2} = \sqrt{\frac{-B \mp \sqrt{B^2 - 4AC}}{2A}} \quad (2.35)$$

In the resonator structure, the electrostatic forces created by the proof mass voltages and the mechanical restoring forces on the resonator tines due to deflections are in equilibrium. However, when the electrostatic forces overcome the restoring mechanical forces due to high proof mass voltages, pull-in takes places. The pull-in state should be avoided because high proof mass voltages create a spark and damage the thin capacitive plates. The analytical calculation is performed according to the

balance of the electrostatic forces and restoring mechanical force on one of the resonator tines for the out of phase mode and opposite sign proof mass voltage configuration as follows;

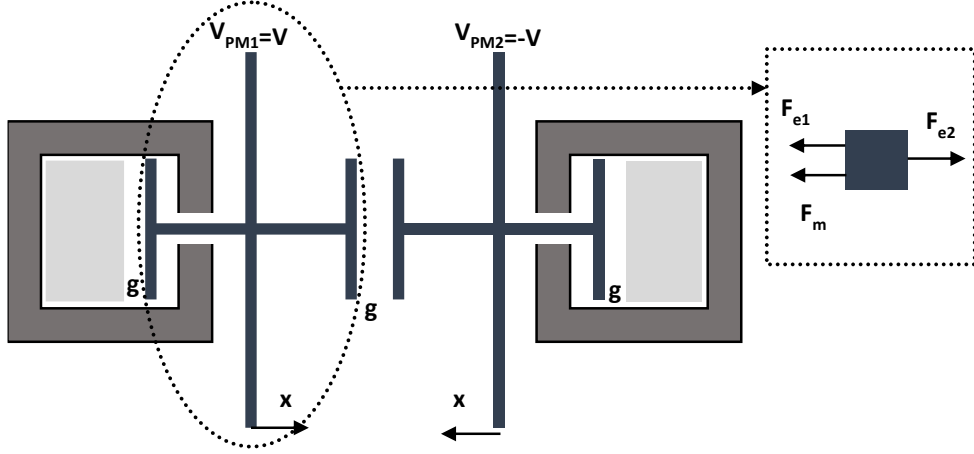


Figure 2.5. Schematic view of the tines for pull-in voltage calculation and free body diagram.

$$F_{e,1} + F_m + F_{e,2} = 0 \quad (2.36)$$

where  $F_{e,1}$  is the electrostatic force between the capacitive plate and the drive electrode,  $F_m$  is the mechanical restoring spring force, and  $F_{e,2}$  is the electrostatic coupling force between the tines.

$$-\frac{1}{2} \frac{\varepsilon_0 L_p h}{(g+x)^2} \{V_{PM1} + v_{ac} \sin(\omega t)\}^2 - k_m x + \frac{1}{2} \frac{\varepsilon_0 L_p h}{(g-2x)^2} \{V_{PM1} - V_{PM2}\}^2 = 0 \quad (2.37)$$

where alternating current is negligibly small compared to proof mass voltage and the alternating term is cancelled due to capacitance change between the capacitive plate and sense electrode behaving as a balancing force. Besides, the double frequency term is neglected. The simplified form of the force balance equation will be,

$$-\frac{1}{2} \frac{\varepsilon_0 L_p h}{(g+x)^2} V^2 - k_m x + \frac{1}{2} \frac{\varepsilon_0 L_p h}{(g-2x)^2} 4V^2 = 0 \quad (2.38)$$

After simplification of equation (2.38), the pull-in voltage is;

$$V(x) = \sqrt{\frac{k_m x}{\varepsilon_0 L_p h \left( \frac{2}{(g-2x)^2} - \frac{1}{2(g+x)^2} \right)}} \quad (2.39)$$

The equilibrium position of the force is found by taking a derivative of the voltage with respect to position and equating it to zero.

$$\frac{\partial V(x)}{\partial x} = 0 \quad (2.40)$$

$$\frac{\partial V(x)}{\partial x} = \frac{\frac{k_m}{\varepsilon_0 L_p h \left( \frac{2}{(g-2x)^2} - \frac{1}{2(g+x)^2} \right)} - \frac{k_m x \left( \frac{8}{(g-2x)^3} + \frac{1}{(g+x)^3} \right)}{\varepsilon_0 L_p h \left( \frac{2}{(g-2x)^2} - \frac{1}{2(g+x)^2} \right)^2}}{2 \sqrt{\frac{k_m x}{\varepsilon_0 L_p h \left( \frac{2}{(g-2x)^2} - \frac{1}{2(g+x)^2} \right)}}} = 0 \quad (2.41)$$

For equation (2.41) the solution for the displacement at which the pull-in occurs is;

$$x = 0.153467 g \quad (2.42)$$

After putting equation (2.42) into the equation (2.39),

$$V_{pull-in} = 0.201283 \sqrt{\frac{k_m g^3}{\varepsilon_0 L_p h}} \quad (2.43)$$

In common DETF structure as in Figure 1.2, there is only one proof mass voltage applied on the tines. For this configuration, in the lumped model in Figure 2.4, only  $k_1$  and  $k_2$  spring can be adjusted by proof mass voltage. Again for this design, the resonance frequency of the in-phase mode is lower than the out-of-phase mode frequency. As the proof mass voltage is increased, the in-phase mode fails due to pull-in first. Since the out-of-phase mode is used as the operational mode, the resonator can not be operated close to pull-in limit of the out-of-phase mode, where the sensitivity is higher, because the resonator buckles due to in-phase modes pull-in already. However, in this study, the electrostatic spring constant  $k_{elec}$  between the tines behaves as a negative spring and pulls the out of mode frequency close to the

pull-in mode. In other words, when  $k_2 < 0$ , the out of phase mode frequency is smaller than the in phase mode frequency.

The out-of-phase mode and in-phase mode frequency equations can be written in a simpler form as,

$$\omega_1 = \omega_{out-of-phase} = \sqrt{\frac{K_{eff1} + k_D + k_{elect}}{M_{eff1}}} \quad (2.44)$$

$$\omega_2 = \omega_{in-phase} = \sqrt{\frac{K_{eff2} + k_D}{M_{eff2}}} \quad (2.45)$$

Here, it is vital that as the voltage difference is increased, the electrostatic coupling between the tines gets stronger. This creates a broader frequency separation between the out-of-phase and in-phase mode at the zero loading. Moreover, the limiting case for the design is the pull-in of the structure due to the high voltage difference and buckling of the tine due to critical load at the tip. Therefore, by adjusting the proof mass voltages, high resolution can be obtained. After putting thermally induced axial force term(2.26), and stiffness terms (2.28)(2.29)(2.30) into(2.32),

$$\omega_{out-of-phase} = \sqrt{\frac{192 \frac{EI}{L_f^3} + 2.4 \frac{(\alpha_g - \alpha_{si}) \Delta T E_{Si} A_{Si}}{L_f} - \frac{\epsilon_0 L_p h}{g^3} V_{PM1}^2 - \frac{\epsilon_0 L_p h}{g^3} (V_{PM1} - V_{PM2})^2}{\frac{13}{35} \rho w_f L_f + 2\rho (w_c L_c + w_p L_p)}} \quad (2.46)$$

$$\omega_{in-phase} = \sqrt{\frac{192 \frac{EI}{L_f^3} + 2.4 \frac{(\alpha_g - \alpha_{si}) \Delta T E_{Si} A_{Si}}{L_f} - \frac{\epsilon_0 L_p h}{g^3} V_{PM1}^2}{\frac{13}{35} \rho w_f L_f + 2\rho (w_c L_c + w_p L_p)}} \quad (2.47)$$

Note that, the resonance frequency term depends not only the geometrical parameters but also the applied voltages on the tines besides the temperature difference term. In Figure 2.6, it is seen that increasing proof mass voltage decreases the buckling load limit. The force sensitivity, which is the slope of the curve, increases with increasing the proof mass voltage for the zero axial force. Therefore, by adjusting the proof mass voltage, high sensitivity can be obtained by operating the resonator

to the resonators buckling limit. Since the applied force is the thermally induced force for the sensor used in this study, the figure is very useful to understand the behaviour of the resonator under axial load for various voltages.

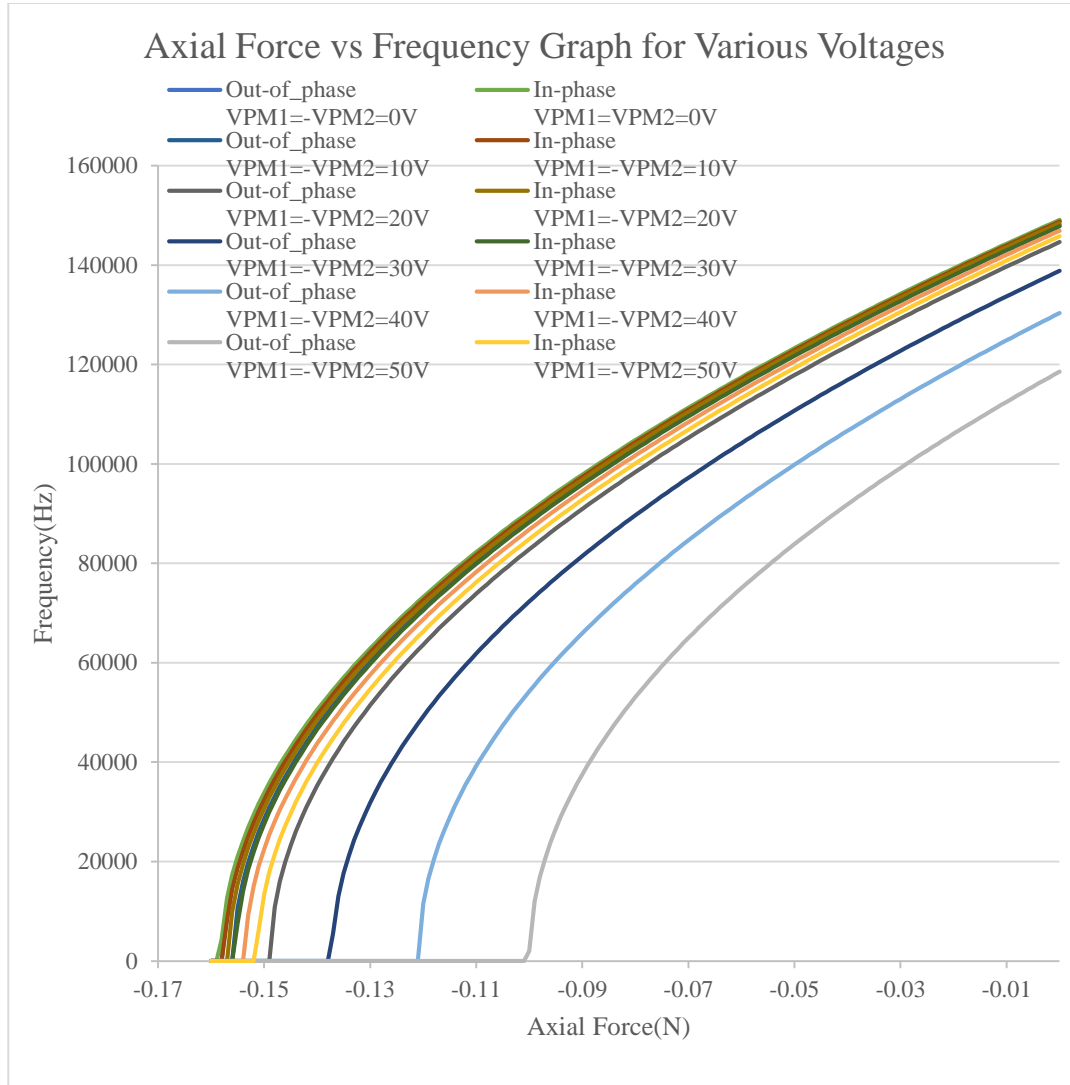


Figure 2.6. The effect of the electrostatic coupling for various voltages on the axial force versus resonance frequency relation.

The scale factor (the rate of change of the out-of-phase mode frequency with respect to temperature) is found using (2.46) and (2.47) by taking derivative with respect to temperature change,

$$\frac{\partial \omega_{out-of-phase}}{\partial T} = \frac{1.2(\alpha_g - \alpha_{si}) E_{Si} A_{Si}}{M_{eff} L_f \sqrt{192 \frac{EI}{L_f^3} + 2.4 \frac{(\alpha_g - \alpha_{si}) \Delta T E_{Si} A_{Si}}{L_f} - \frac{\epsilon_0 L_p h}{g^3} V_{PM1}^2 - \frac{\epsilon_0 L_p h}{g^3} (V_{PM1} - V_{PM2})^2}} \quad (2.48)$$

$$\frac{\partial \omega_{in-phase}}{\partial T} = \frac{1.2(\alpha_g - \alpha_{si}) E_{Si} A_{Si}}{M_{eff} L_f \sqrt{192 \frac{EI}{L_f^3} + 2.4 \frac{(\alpha_g - \alpha_{si}) \Delta T E_{Si} A_{Si}}{L_f} - \frac{\epsilon_0 L_p h}{g^3} V_{PM1}^2}} \quad (2.49)$$

After putting it in a simpler form, it is seen that scale factor is a function of the resonance frequency, material properties used in the sensor. So, it changes throughout the working range. It is also important to emphasize that decreasing resonance frequency increases the sensitivity of the sensor, and it can be adjusted by the proof mass voltages.

$$\frac{\partial \omega_{out-of-phase}}{\partial T} = \frac{1.2(\alpha_g - \alpha_{si}) E_{Si} A_{Si}}{M_{eff} L_f \omega_{out-of-phase}} \quad (2.50)$$

$$\frac{\partial \omega_{in-phase}}{\partial T} = \frac{1.2(\alpha_g - \alpha_{si}) E_{Si} A_{Si}}{M_{eff} L_f \omega_{in-phase}} \quad (2.51)$$

In this system, the coupling strength should be mentioned. In the previous studies, depending on the coupling method and the coupling strength, different approaches are used. In most of the studies, amplitude changes are utilized as a sensing method using the weak coupling between the resonators as mentioned before. For our design, the strength of the coupling between the resonators is comparable with the effective stiffness of the tines. The equations of the electrostatic coupling between the capacitive electrodes and the mechanical stiffness terms are given in (2.14), (2.18) and (2.22). The ratio of stiffness,  $\kappa$ , is defined,

$$\kappa = \frac{k_2}{k_1} = \frac{k_{elect}}{K_{eff} + k_D} \quad (2.52)$$

where  $K_{eff,m}$  is the mechanical stiffness term. There are 2 electrostatic stiffness terms, which are the stiffness between tines and fixed electrodes  $k_D$ , and the stiffness between the resonator tines when there is a proof mass voltage difference  $k_{elec}$ .

$$\kappa = \frac{-\frac{\epsilon_0 L_P h}{g^3} (V_{PM1} - V_{PM2})^2}{192 \frac{EI}{L_f^3} + 2.4 \frac{(\alpha_g - \alpha_{si}) \Delta T E_{Si} A_{Si}}{L_f} - \frac{\epsilon_0 L_P h}{g^3} V_{PM1}^2} \quad (2.53)$$

In the opposite proof mass configuration and no temperature change,  $\kappa$  is,

$$\kappa = \frac{-\frac{\epsilon_0 L_P h}{g^3} (2V_{PM})^2}{192 \frac{EI}{L_f^3} - \frac{\epsilon_0 L_P h}{g^3} V_{PM}^2} \quad (2.54)$$

In analytical mode, the numerical values for this design and parameters given in Table 2-1 are summarized in the table below.

Table 2-2. Parameters of the numerical analysis for the opposite proof mass voltage configuration using the geometrical parameter used in Table 2-1.

Parameter	Symbol	Value	Unit
Effective mass	$M_{eff}$ (2.10)	0.1508	$\mu\text{g}$
Effective spring constant	$K_{eff}$ (2.11)	757.120	N/m
Proof mass voltages ( $V_{PM1} = -V_{PM2} = V_{PM}$ )	$V_{PM}$	50	V
Electrostatic stiffness between the electrode and tine	$k_D$	-30.990	N/m
Electrical coupling stiffness	$k_{elec}$	-123.959	N/m
Ratio of stiffness	$\kappa$	0.1707	-

Figure 2.7 shows the variation of the stiffness ratio of the electrostatic coupling stiffness to the  $k_1$  term, which includes the effective spring of the resonator for the out-of-phase mode shape and the electrostatic stiffness between the fixed electrodes

and the capacitive tines. It is seen that, although there is two electrostatic coupling stiffness on tines each side since the coupling stiffness is higher, the out-of-phase mode frequency drops with increasing proof mass voltage. Besides, the electrostatic coupling gets stronger and  $\kappa$  gets higher with increasing voltage

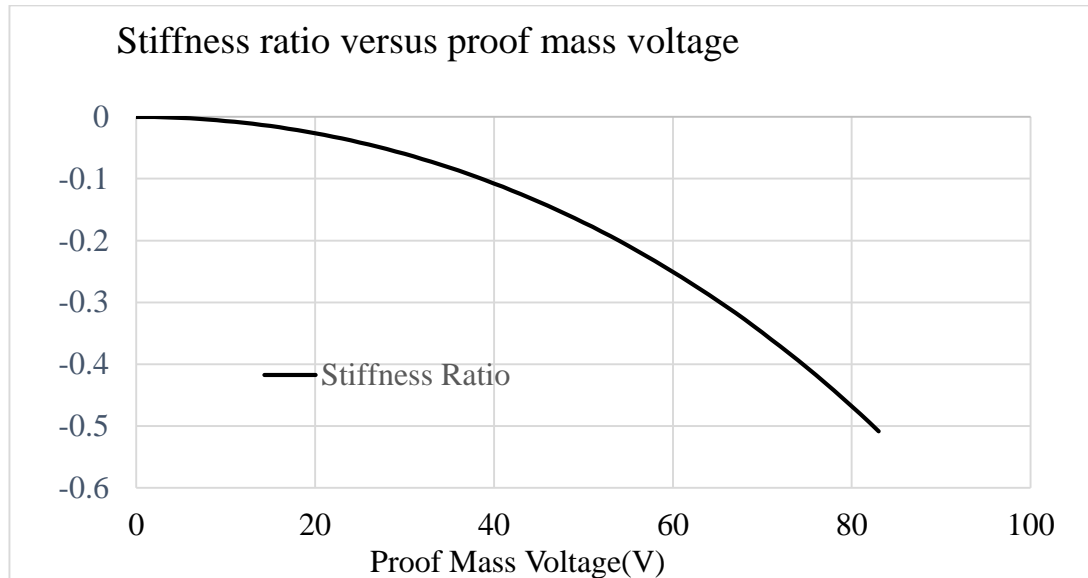


Figure 2.7. Stiffness ratio of the electrostatic coupling stiffness to effective stiffness with respect to proof mass voltage.

## 2.4 Finite Element Analysis of Resonant MEMS Load Cells

The analytical model is validated by finite element modelling. For this purpose, COMSOL Multiphysics is used. Modal analysis, electro-mechanical analysis and thermo-electro-mechanical analysis are performed to validate the analytical model. The 3D geometric model is constructed by parametric variables which are given in Table 2-1. For the material properties, built-in single-crystal isotropic silicon and borosilicate glass are selected. In the physics definition, all material is defined as a linear elastic material. The glass is fixed from a corner and roller definition is specified to the 3 surfaces letting substrate to expand in all directions due to thermal expansion. For the electrical boundary conditions, the terminal is selected for the faces of the tines. The proof mass voltages are defined as parametrically. The voltage

value of the drive electrodes is defined as zero voltage since the amplitude of the applied AC voltage is very small for the excitation compared to the bias voltage. All the model is placed in a box which represents the vacuum whose material property is unity for the relative permittivity. This includes the fringing field effect at the edges of the plates.

#### 2.4.1 Pull-in Voltage and Static Deflection Study for DETF Resonator

At the resonance, the system is excited by AC signal with a bias voltage. As a result of the bias voltage, there is a static deflection on the tines. In this study, there is a vital role in the proof mass voltage, which is changing the temperature sensitivity of the resonator. Therefore, to operate the sensor within the safe voltage range, in other words, to avoid the pull-in or buckling due to electrostatic force, the pull-in analysis is crucial. In this analysis, the voltages which bring the tines to the equilibrium at a given displacement is calculated. The analysis result shows that the pull-in voltage for this design is 51.6V, which is the minimum value of Figure 2.8, assuming the voltages of the tines are same in magnitude but opposite sign. The analytically calculated proof mass voltage by equation (2.43) is 49.75V.

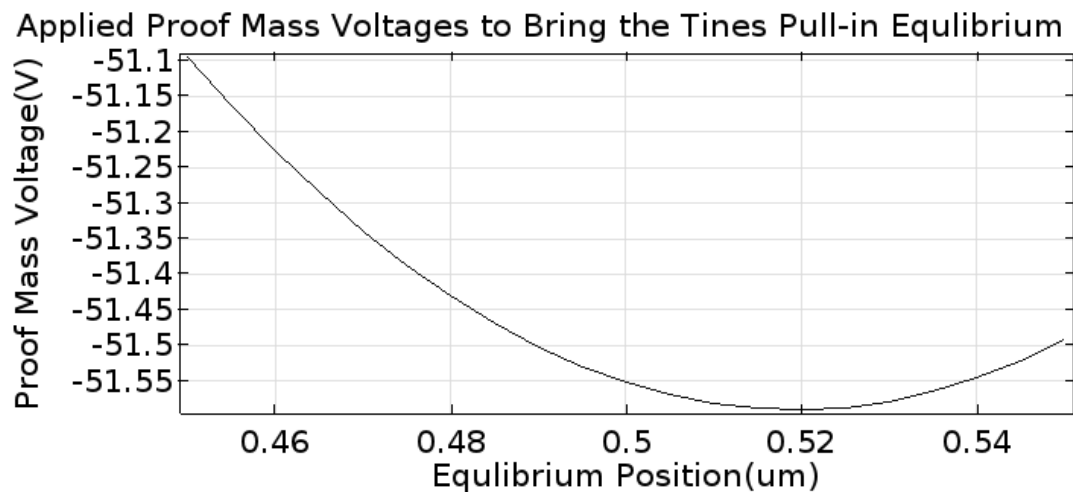


Figure 2.8. Pull-in analysis performed by COMSOL Multiphysics

After finding the pull-in voltage, the effect of the increasing proof mass voltage effect on the static deflection is investigated. The applied proof mass configuration and the corresponding deflection graph for 45V proof mass voltage are shown in Figure 2.9.a and Figure 2.9b, respectively.

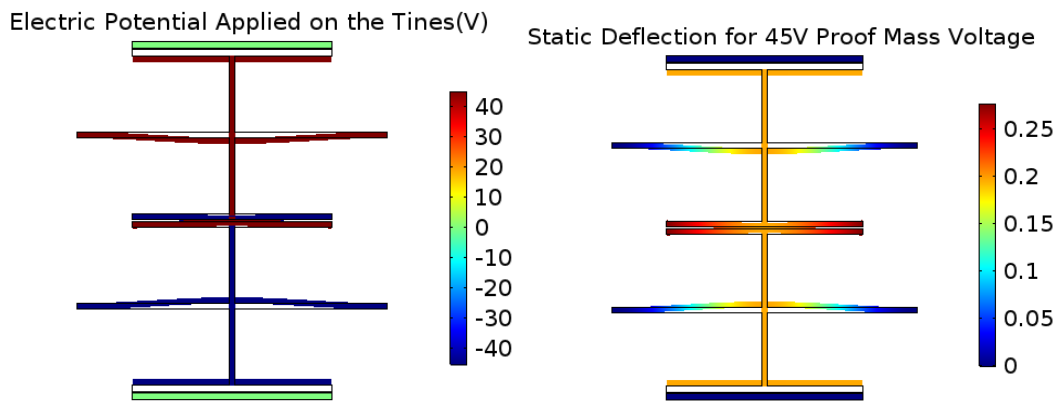


Figure 2.9. Applied voltage and corresponding static deflection analysis of tine resonator for +45V and -45V proof mass voltages.

Figure 2.10 shows the tip point displacement of a deflected tine for the increasing voltages. As it is seen from the graph, the deflection magnitude increases nonlinearly with the increasing proof mass voltage. This also shows that electrostatic softening effect moves the resonator to the pull-in state.

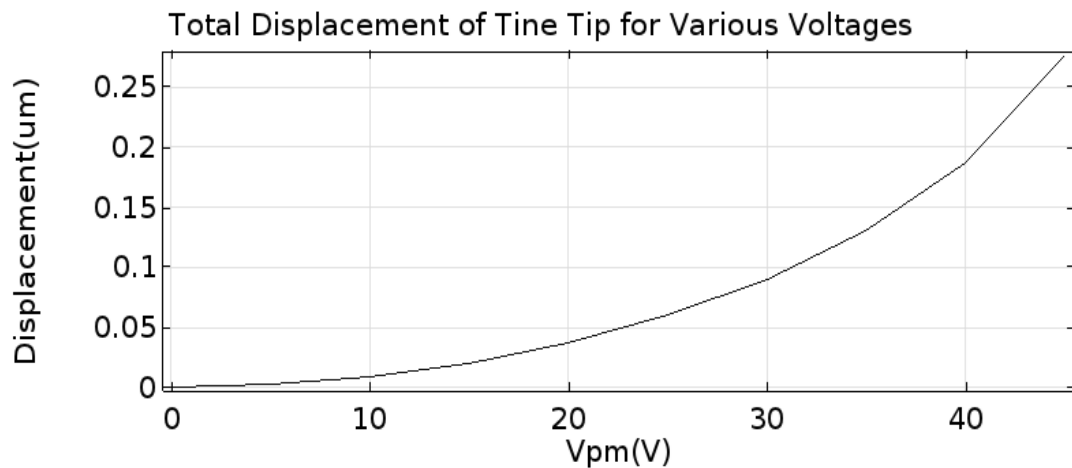


Figure 2.10. Displacement versus voltage graph of the endpoint of the capacitive tine.

Figure 2.11 shows the deflection curve of the electrostatic coupling electrode for various voltages. It is observed that increasing voltage causes the static deflection at the endpoint of the capacitive tine much higher than the centre of the resonator tine. This also creates a nonlinearity on the capacitive tine by increasing the amplitude stiffening effect and electrostatic softening. These effects are the critical parameters, which change the resonance characteristic of the structure nonlinearly.

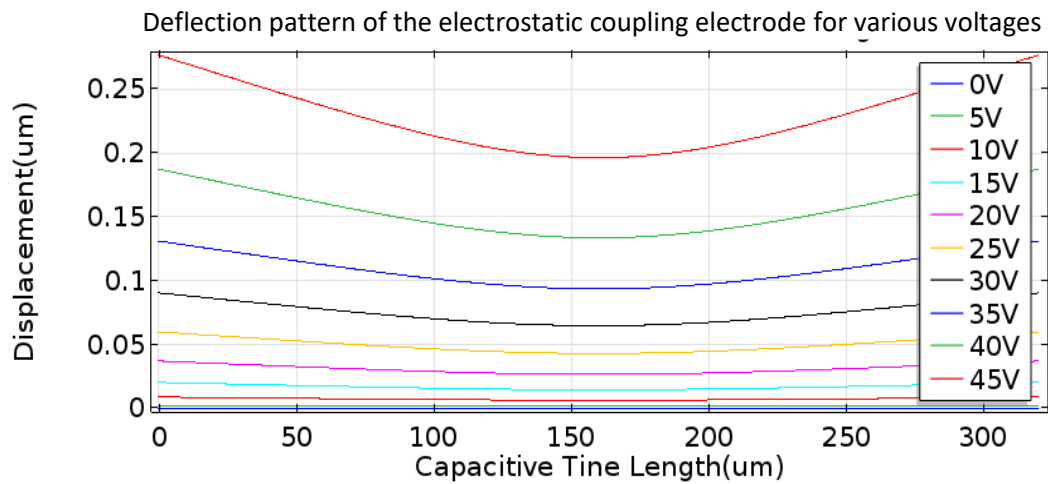


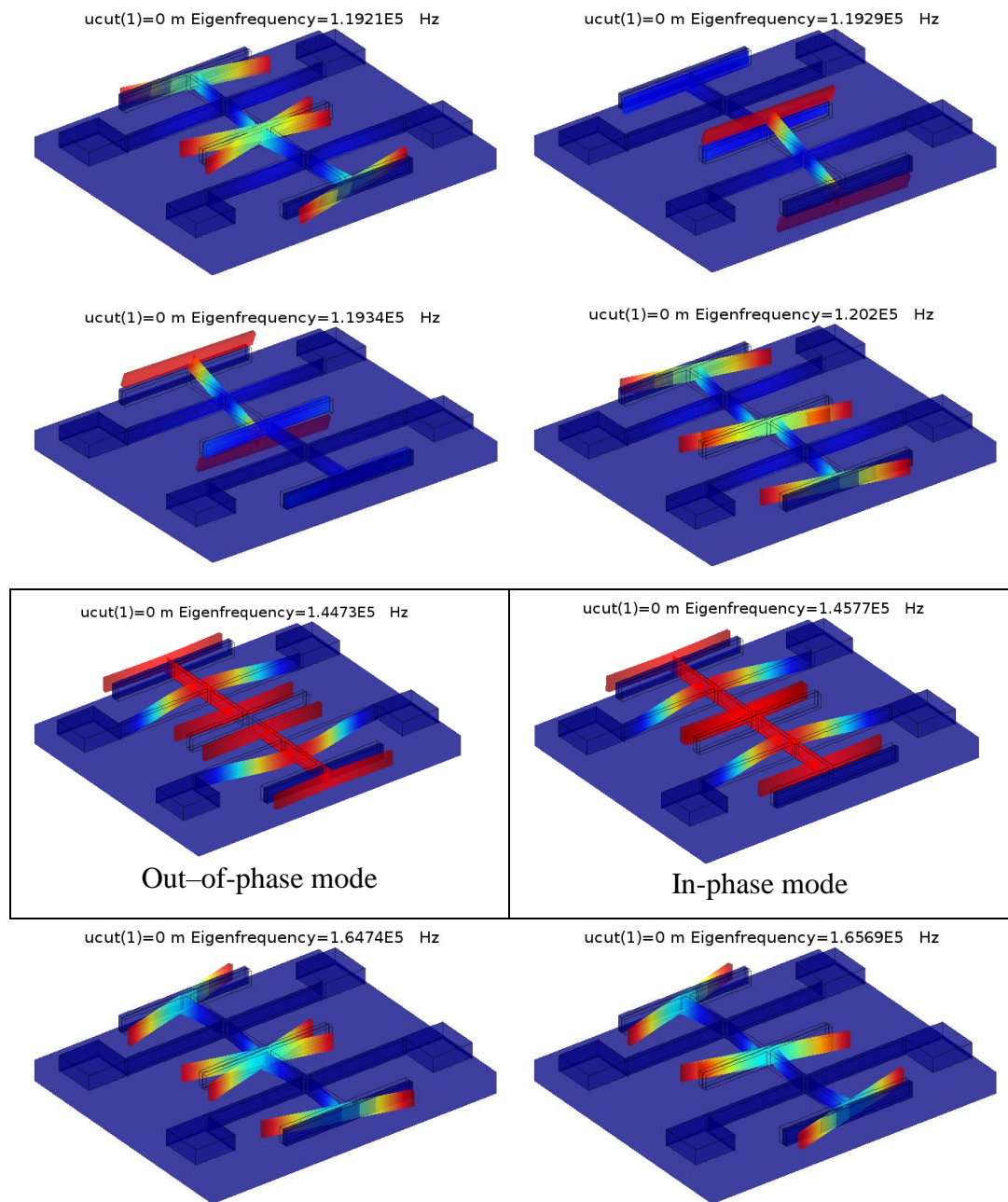
Figure 2.11. Deflection pattern of the electrostatic coupling electrode for different voltages.

#### 2.4.2 Mode Shape Analysis for the DETF MEMS Resonator

The modal analysis is also performed to validate the analytical model results. The eigenfrequency study is conducted to find the first eight mode shapes, which are summarized in Table 2-1. The geometrical model and the boundary conditions are the same as explained before. Geometric nonlinearities are taken into consideration in the simulations. The proof mass voltage applied to the tines is 10V in magnitude and opposite sign. Finite element analysis shows that the analytical model is verified for the out-of-phase and in-phase modes. For the 10V proof mass voltage out of phase mode frequency and in-phase mode frequency deviates 2.23% and 2.04%, respectively. The reason for this deviation is the assumption that the capacitive tines are rigid, which makes the analytical model results higher. Besides, in the FEM, the

fringing field effects are included, which enhances the electrostatic softening effect, which decreases the resonance frequency as expected. By introducing this electrostatic spring, the out-of-phase mode frequency gets lower than the in-phase mode due to electrostatic coupling.

Table 2-3. The first 8 mode shape simulation results obtained by COMSOL for  $V_{PM2}=10V$ ,  $V_{PM2}=-10V$



### 2.4.3 FEM Simulations of the Electrostatic Softening Effect

After the modal analysis, the effect of the electrostatic softening effect is studied. For this purpose, an eigenfrequency analysis is conducted with a parametric sweep for the same proof mass voltages where a single resonator is used as the sensing element. The same model, which is explained before, is used for this study. Figure 2.12 shows the resonance frequency change for the various proof mass voltages for the in-phase mode and the out-of-phase mode, which are obtained by analytical and finite element model. As the voltage is increased, the frequency change rises. It is seen that the analytical model and the FEM are in agreement. Since there is no electrostatic coupling, in-phase mode and out-of-phase mode frequencies are very close to each other and decrease with the same behaviour.

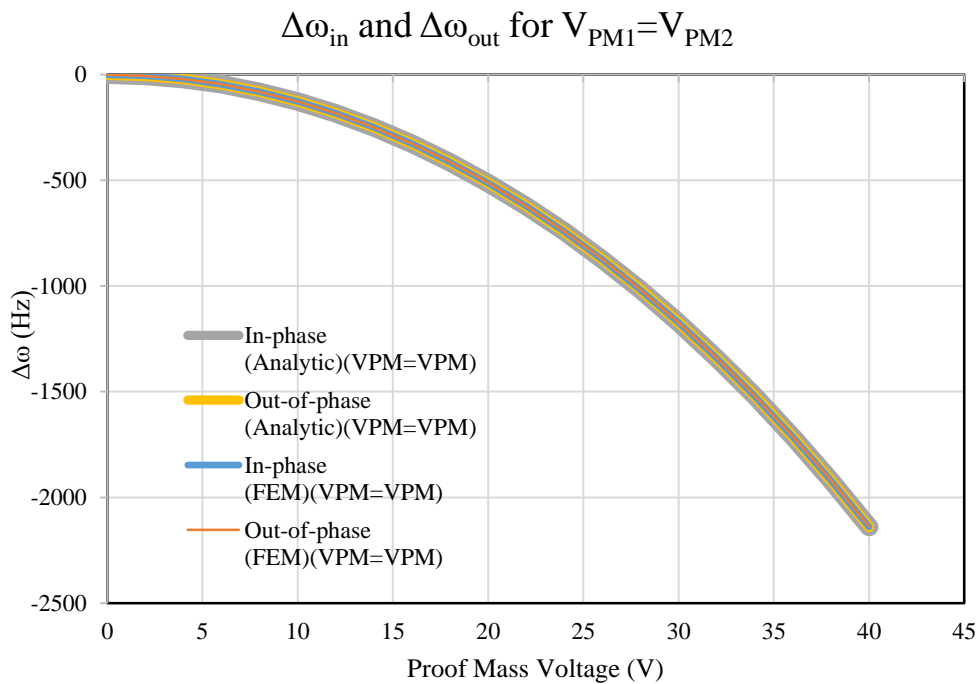


Figure 2.12. The effect of the increasing proof mass voltage for the same proof mass voltage configuration where the single tine is utilized as the temperature sensor.

The same analysis is performed for the opposite sign proof mass voltage configuration. Figure 2.13 shows that due to the electrostatic coupling between the resonators, the out-of-phase mode frequency decreases drastically compared to the

in-phase mode as expected. Moreover, for this proof mass configuration, the analytical model and the finite element model agrees also. However, it is noted that as the proof mass voltages close to the pull-in voltage, frequency shift for the analytical and the finite element model become distant. The reason for this separation could be the increasing nonlinearity in the finite element model.

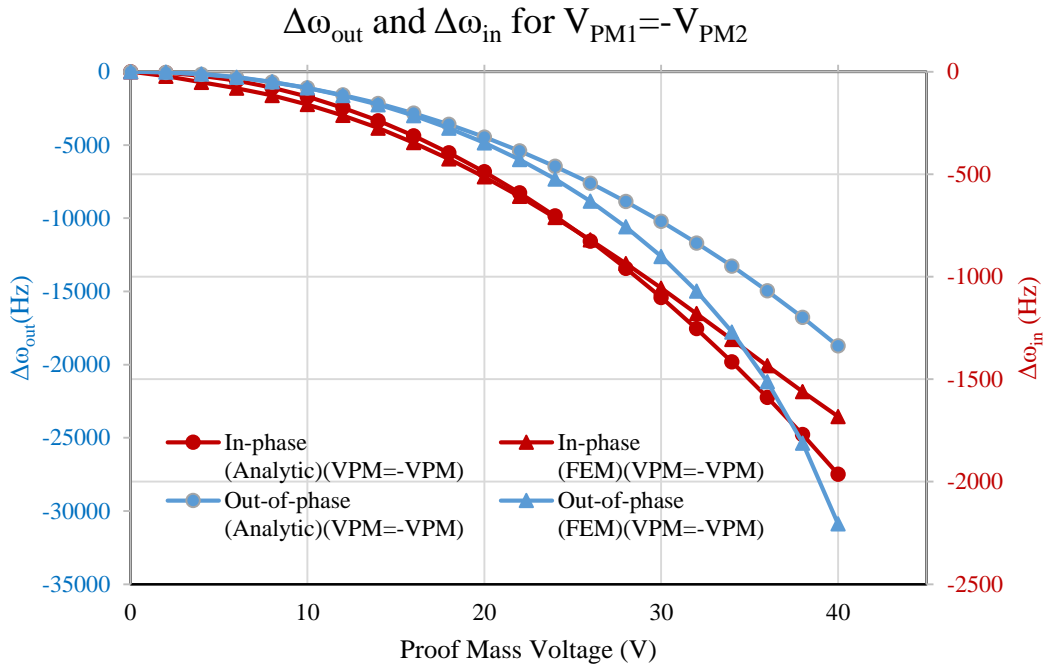


Figure 2.13 The electrostatic softening effect due to the increasing proof mass voltage for the opposite sign proof mass voltage configuration.

#### 2.4.4 Finite Element Simulations of the Temperature Change

The analytical model of the temperature change is validated with the finite element simulations performed using COMSOL Multiphysics, as explained before. Figure 2.14 represents the analytically calculated results for the frequency change versus temperature. Analytical results show that the frequency increases linearly with the increasing temperature. It is also seen that the out of phase mode for the opposite sign proof mass configuration gives the best result in terms of the temperature sensitivity, which is the slope of the lines.

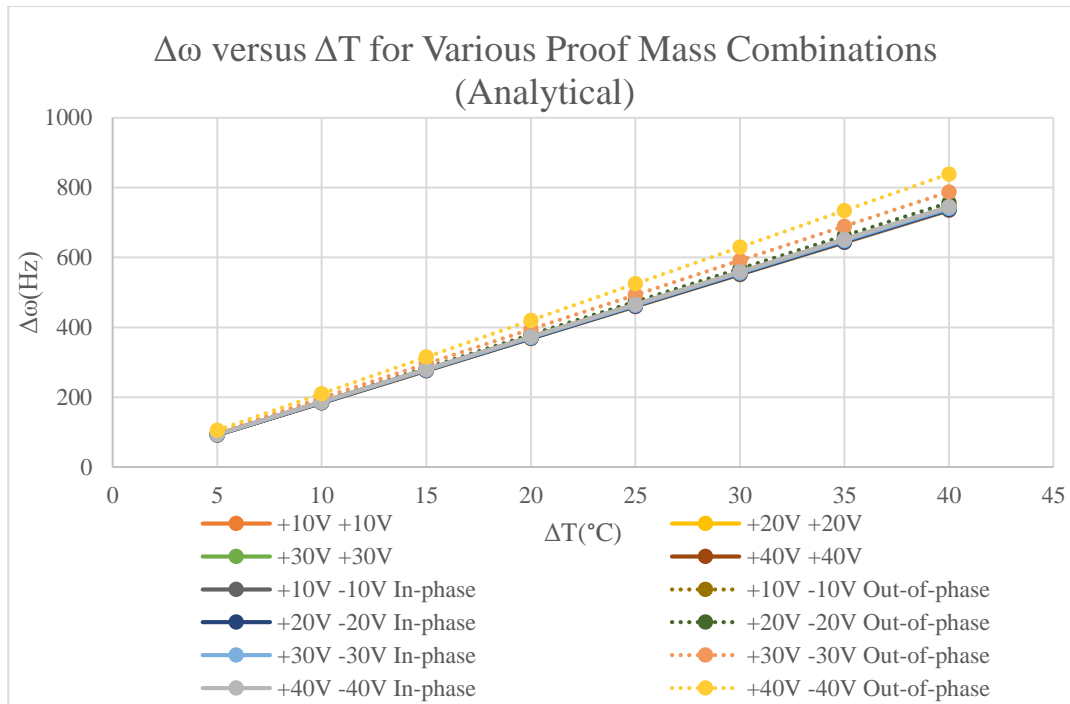


Figure 2.14. Frequency change versus temperature change graphs obtained analytically for the same, and the opposite sign proof mass configurations.

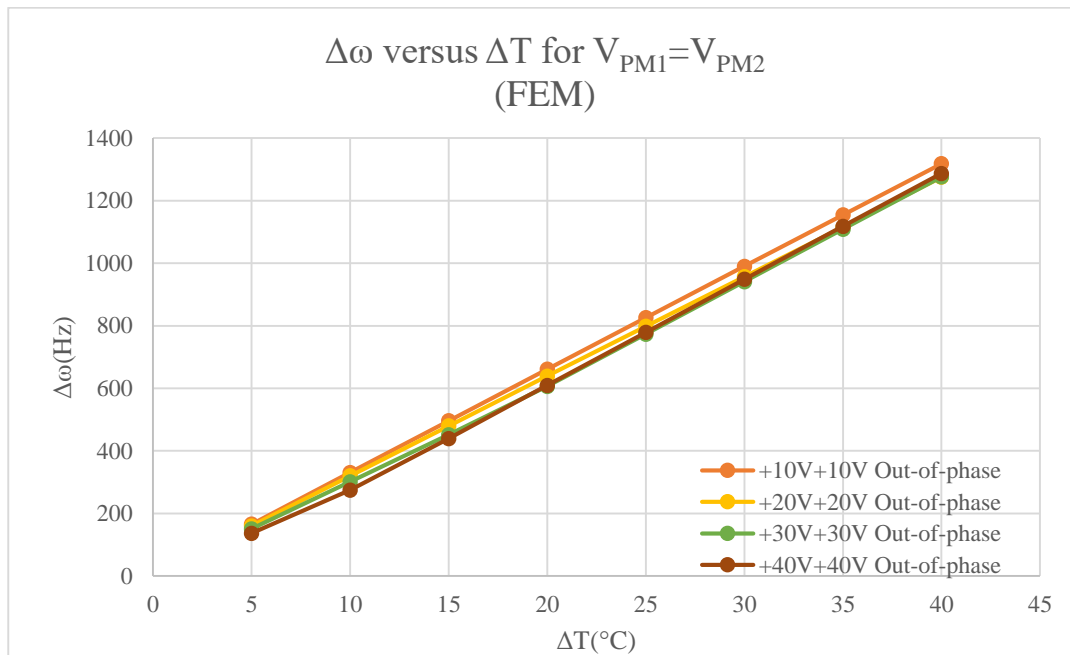


Figure 2.15 Frequency change versus temperature change graphs obtained by FEM results for the same proof mass configurations.

The FEM results, as shown in Figure 2.15, are in agreement with the analytical model for the same proof mass voltage configuration . The frequency change with the temperature change does not change significantly with the increasing proof mass voltage as in analytical results for the single tine same proof mass voltage configuration.

The FEM results for the opposite sign proof mass configuration is given in Figure 2.16. For the lower voltage values, the behaviour of the frequency change in the presence of the temperature change and frequency change values are in agreement with the analytical model. At the higher voltages, the frequency change with temperature increase is linear again. However, the sensitivity, which is the slope of the frequency change versus temperature change graph is higher than the analytical model. The main reason for this behaviour is the nonlinearity of the resonator due to high proof mass voltage. This FEM analysis shows that as the voltage comes closer to the pull-in voltage, the sensitivity increases rapidly as expected.

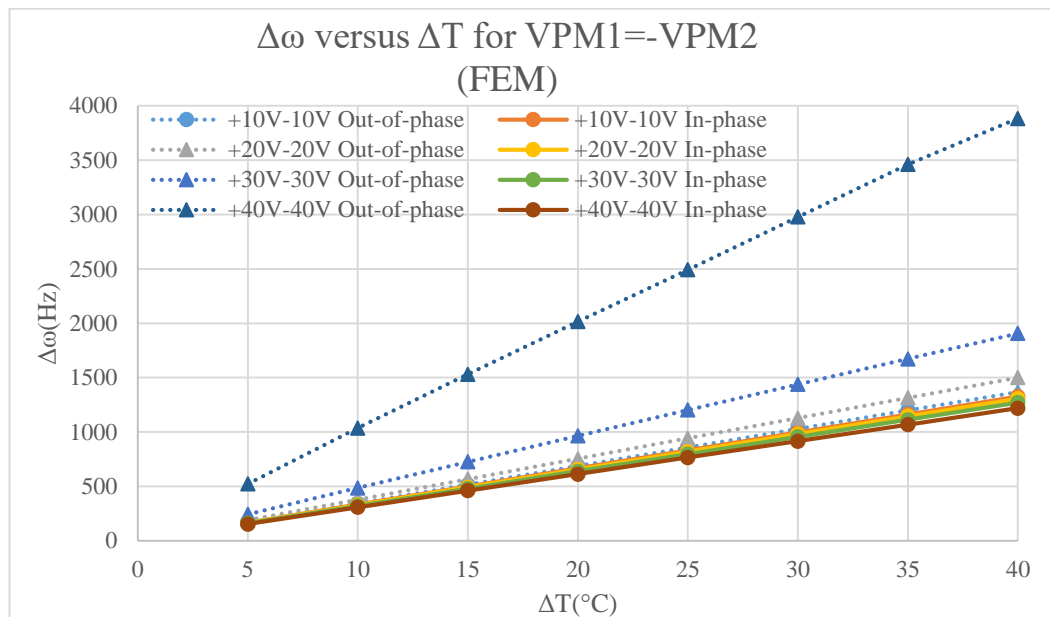


Figure 2.16. Frequency change versus temperature change plot for opposite proof mass voltage configuration.

## 2.5 Summary

In this chapter, analytical and finite element modelling of the DETF MEMS resonator is presented. The equation of motion for the resonator beam is solved to explain the desired mode resonance behaviour,. The excitation and sensing methods are described with the equations in detail. The electrostatic softening between the tines is presented. The effect of electrostatic softening in the opposite proof mass configuration on the resonance frequency and the temperature sensitivity are discussed. This effect is shown with the analytical model and validated with the FE model.

## CHAPTER 3

### FABRICATION OF THE DESIGNED MEMS RESONATOR

In this chapter, the fabrication process of the double-ended tuning fork MEMS resonator used in this study is explained briefly. The fabrication steps are performed in the cleanroom environment to prevent contamination. In Section 3.1, the fabrication of the sensor structure, which consists of the silicon-on-insulator (SOI) wafer for the sensor structure and the anchor wafer for the electrical connections, is explained in detail. In Section 3.2, the results of the fabrication are shown. The fabrication of the microfabricated resonator is similar to aMEMS process developed in METU MEMS Centre without the hermetic encapsulation with an SOI cap wafer. The further details of the microfabrication steps can be found in [56].

#### 3.1 Process Flow of the Sensor Structures

The fabrication of the sensors is basically a silicon on glass (SOG) process, which contains 4 main fabrication steps. These steps include the fabrication of the anchor wafer, the fabrication of the device layer, the bonding of the wafers and process after bonding.

The process flow of the anchor wafer starts with the precleaning step of a glass wafer, which is the immersion in piranha solution ( $\text{H}_2\text{SO}_4\text{-H}_2\text{O}_2$ , 1-1) for 30 minutes to remove the organic contamination. Then the glass wafer is immersed into the buffered hydrofluoric acid (BHF) solution ( $\text{HF-H}_2\text{O}_2$ , 1-7) for 5 minutes to roughen the surface of the glass substrate to increase the adhesion of the metallization layer, which is illustrated in Figure 3.1.

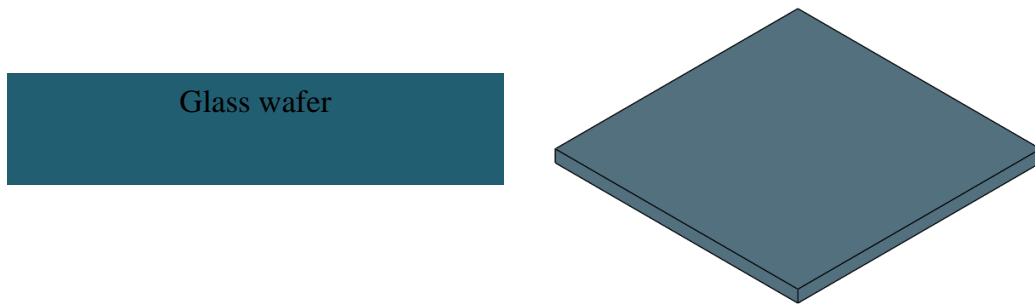


Figure 3.1. Cleaning step of the glass wafer.

Then, a chromium (Cr) layer as the adhesion layer and a gold (Au) layer are deposited by sputtering as the hard mask for the formation of anchors. After the anchor lithography, the metal mask is formed with wet etching in commercial TFA gold etchant and commercial 1020AC chromium etchant. Then, the photoresist is stripped with PRS2000 solution. The anchors are etched as in with HF solution, and the metal hard mask layer is stripped with the same metallization etchants, and anchors for the suspended resonant structures are formed, as illustrated in Figure 3.2

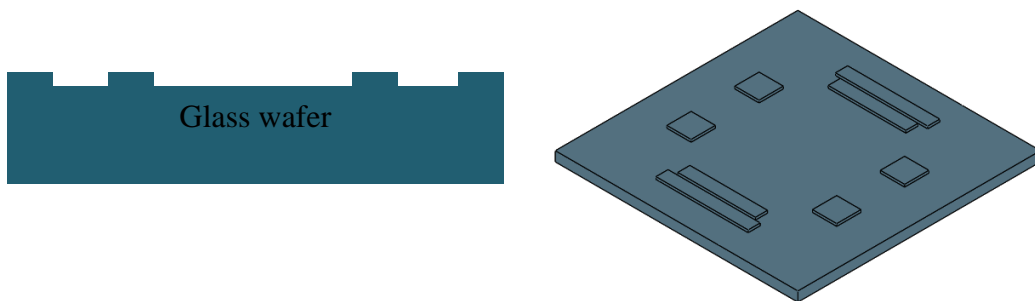


Figure 3.2. Anchors on glass wafer formed with wet etching in HF solution.

After the formation of glass anchors, another 20nm Cr and 200nm Au layers are deposited on the wafer with sputtering to create the metallization lines and the bonding regions for the structure. The deposited metallization layer is formed with lithography. For the step coverage on the anchors, a thick photoresist is used, which is SPR 220-7. Metal wires are defined with wet etching in TFA gold etchant and 1020AC chromium etchant. The photoresist is stripped with PRS2000 solution. This

step is the last -step for the substrate wafer, which includes the anchors for the resonant structures and metal wires for the electrical connections, as it is seen in Figure 3.3

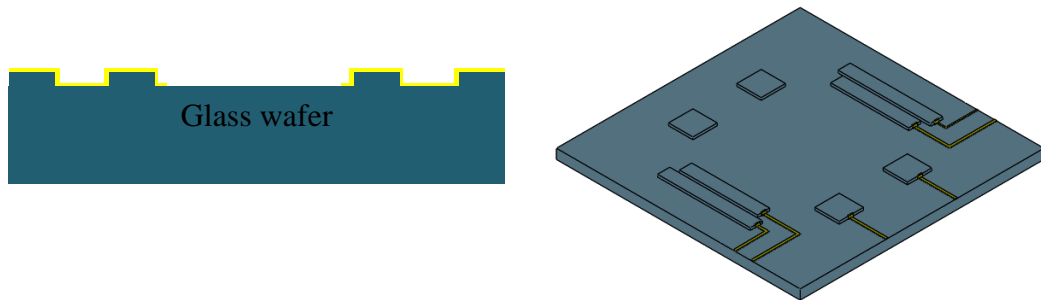


Figure 3.3. Substrate wafer with anchors and metallization lines.

An SOI wafer having 35 $\mu\text{m}$  device thickness and 2  $\mu\text{m}$  buried oxide is used. The selection of orientation is important since Young's modulus of silicon is orientation dependent. For  $\langle 111 \rangle$  plane Young's modulus is the same in all directions of the flexural vibration direction. Besides very low resistivity silicon is used for the device layer. For the fabrication of the SOI wafer, firstly, it is precleaned to remove the organic contaminations like anchors wafer in piranha solution for 30 minutes. Then, to remove very thin native oxide, which grows in atmospheric conditions due to air moisture, an etch in BHF is done for 5 minutes.

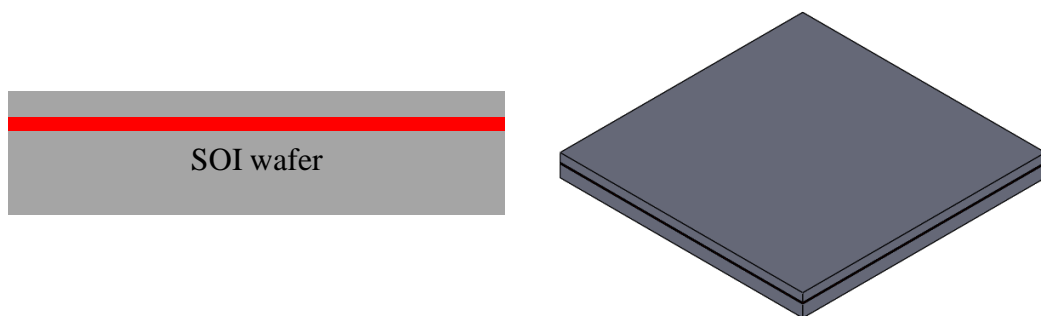


Figure 3.4. Precleaning of the SOI wafer is done in piranha and BHF solution.

After the lithography for the resonant structures, the device layer of the wafer is etched with the DRIE process until the buried oxide layer is reached. The photoresist

of the SOI wafer is removed by immersion in the PRS2000 solution for 30min after the O<sub>2</sub> plasma etching to remove the sidewall polymer residues. The SOI wafer is cleaned in the piranha solution before the bonding. The simplified view is in Figure 3.5

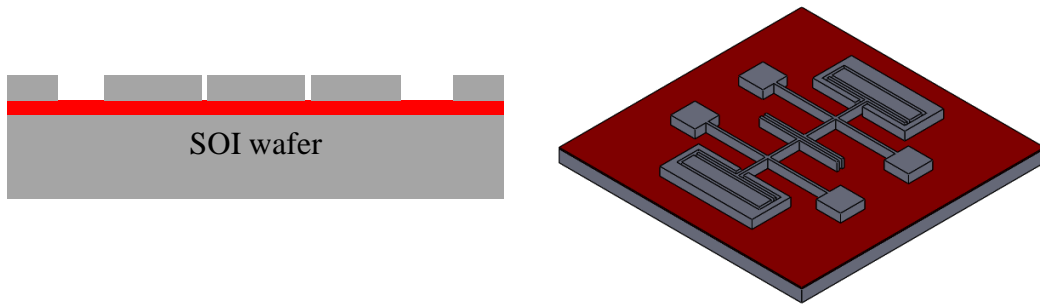


Figure 3.5. Formation of the resonant structures is done with DRIE.

After the fabrication of the substrate wafer and the device wafer, by anodic bonding 2 wafers are bonded together. In this step, in addition to the bonding force at elevated temperatures, high voltage is applied to the wafers to create SiO<sub>2</sub> bonds between the silicon device layer of the SOI wafer and the glass anchors as in Figure 3.6

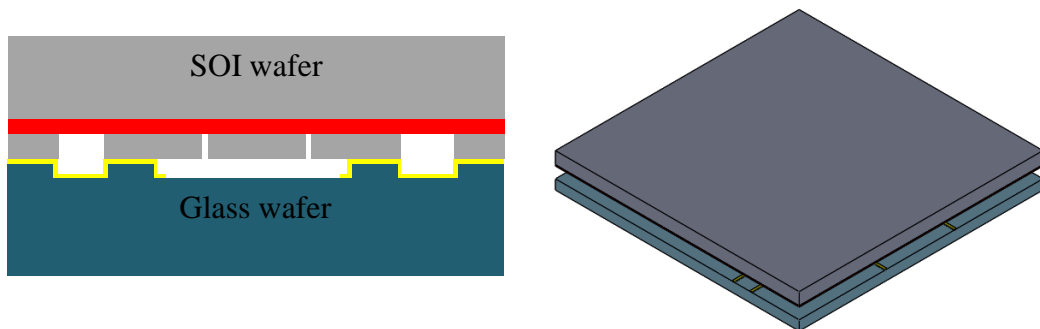


Figure 3.6. Anodic bonding of the substrate wafer and the SOI wafer.

The handle layer of the SOI wafer is removed with the thinning process in DRIE until the buried oxide is reached. Then the bonded wafers are put into 1:7 BHF solution to release the suspended structures. The duration of the BHF is optimized in this step since the etchant also etches the glass layer. The excess etch duration creates undercut for the metallization layer. Therefore, breakage of the metal wire occurs

where the metal lines are narrow. The schematic view of the last step is given in Figure 3.8.

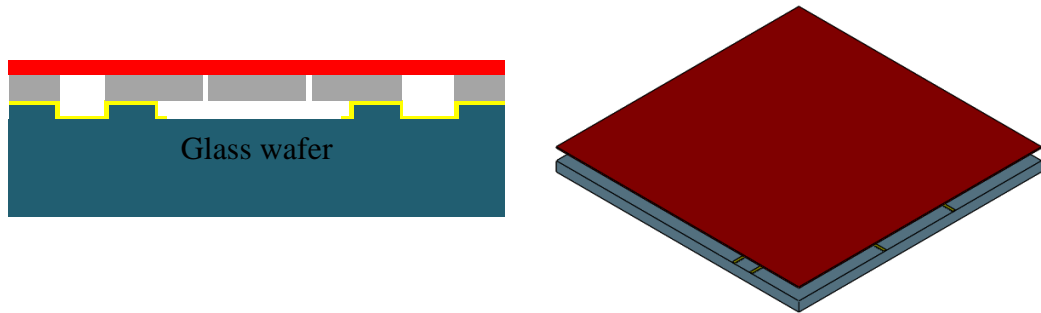


Figure 3.7. Removal of the handle layer of the SOI wafer is processed by DRIE.

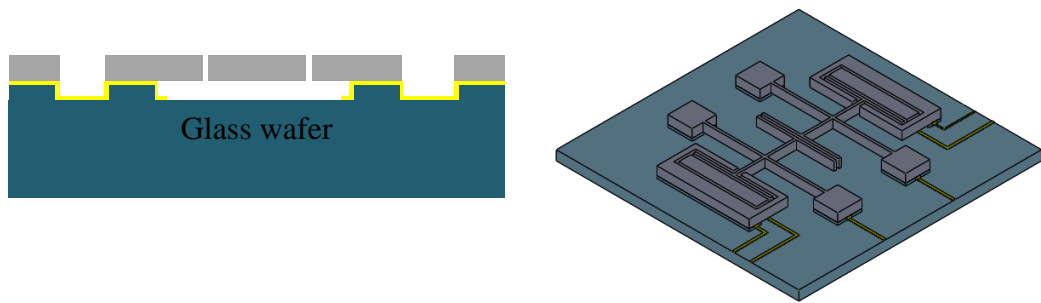


Figure 3.8. Removal of the buried oxide in BHF solution.

After the fabrications steps, the wafer is diced into small sensor chips. The dimensions of the chips are determined at the beginning of the design phase considering the dimensions of the ceramic dual-inline packages(CERDIP) used in testing. Since there is no encapsulation for hermetic packaging and wiring as in aMEMS process[56], for electrical connections, wire bonds are applied to the electrodes as in Figure 3.9 The residual contamination on the sensors can prevent the movement of the resonators, or by sticking on the moving tines, they might change the resonance characteristic. Therefore, the dicing and wire bonding processes are performed carefully to prevent any contamination. The metallization lines in Figure 3.10 are used in the completed aMEMS process. For this study, all the connection

are provided with the wire bonds, and the test are performed. in a vacuum chamber, instead of hermetic packages.

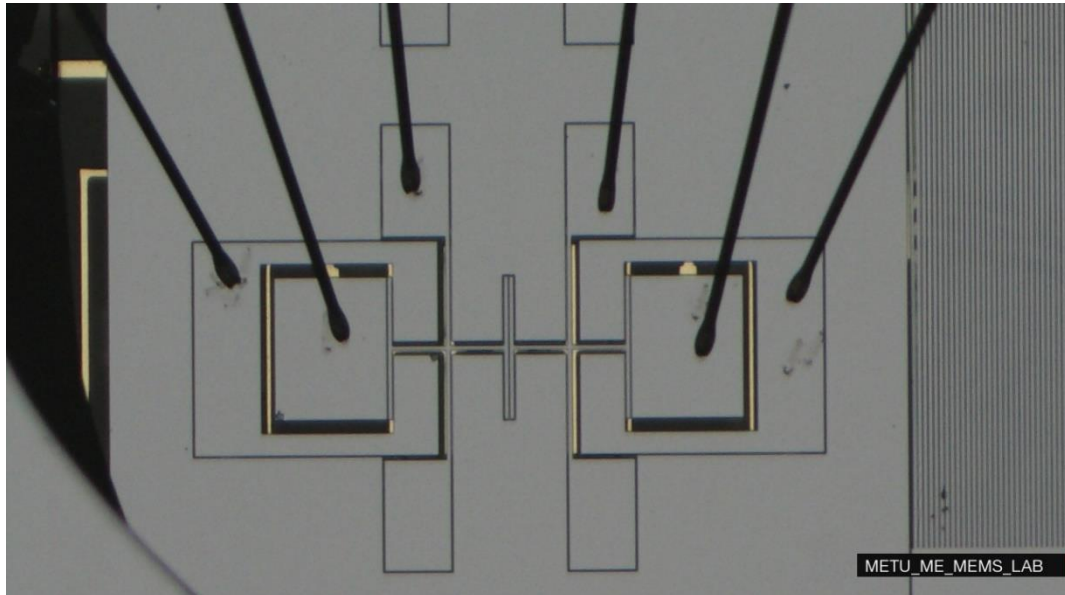


Figure 3.9. Optical microscopy photo of the device with wire bonds.

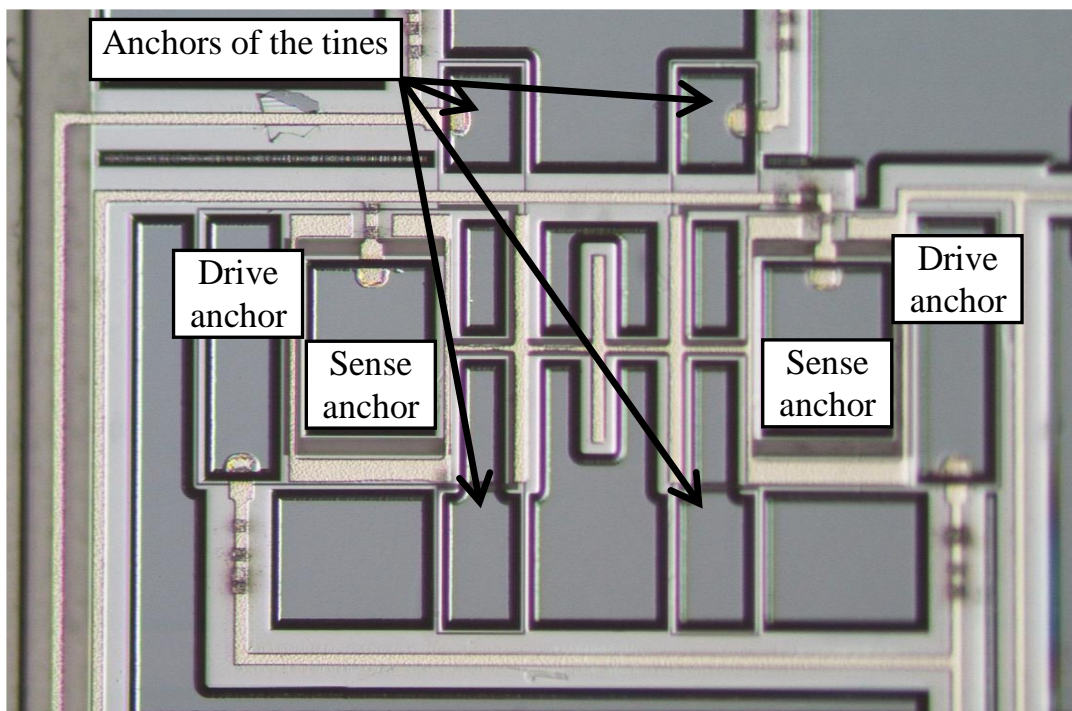


Figure 3.10. The bottom view through the glass wafer.

### 3.2 Fabricated DETF Resonators

After the fabrication, SEM images of the fabricated sensor are captured in METU MEMS Center. These SEM images are taken in order to check the critical dimensions of the sensors, as in Figure 3.11.

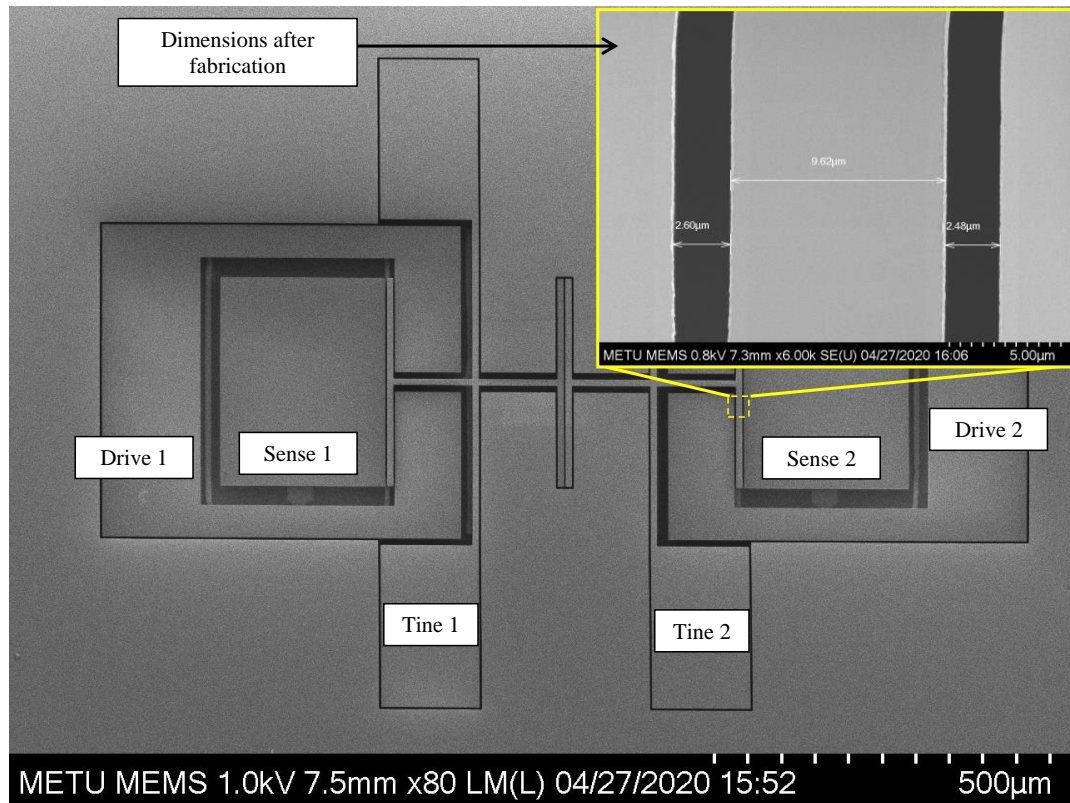


Figure 3.11. SEM image of the fabricated device with the critical dimensions which are indicated in the box.

These critical dimensions are the capacitive gaps between the capacitive plates and fixed electrodes, the capacitive gap between the electrostatic softening plates and the thickness of the sensor structure. The change in the geometrical parameter changes the effective spring constants and the mass of the resonator. Therefore, the resonance frequency of the resonator is affected significantly. By comparing the design parameters given in Table 2-1 and the dimensions given in Figure 3.11, it is seen that the gaps are wider, and the sensor structure widths are smaller than the designed values. The reason for the change in the sensor dimensions is the imperfections in

the fabrication due to undercuts in lithography and deep reactive ion etching steps. Therefore, for further study, the undercuts should be considered as the design parameter to validate the analytical model and the test results.

### **3.3 Summary**

In this chapter, the fabrication processes of the designed resonant temperature sensor are presented briefly. The simplified crosssection and three-dimensional isometric illustrations are used for the explanation of each step. The fabrication results are discussed with captured SEM images. The importance and effects of the fabrication imperfections are emphasized.

## **CHAPTER 4**

### **TEST RESULTS**

In this chapter, the followed test procedures, equipment used in the testing and the characterization results of the MEMS DETF resonant sensor are presented. The system-levels are performed in a vacuum chamber. The temperature is controlled with a thermoelectric heater and a commercial temperature sensor. In Section 4.1, the frequency response setup and the characterization results of the fabricated resonator are presented. The frequency response of the system for different proof mass voltages are shown. Section 4.2 presents the system-level tests. In these tests, the response of the MEMS DETF resonators to the temperature change is investigated. Finally, the results and conclusions are presented in Section 4.3.

#### **4.1 Frequency Response Characterization of the Resonators**

There are two primary purposes for the characterization of the system. The first one is to prove whether the sensors operate correctly or not. The second purpose of the frequency response testing is to validate the analytical model and finite element modelling with the test results. In Section 4.1.1, the test setup used in the characterization is presented for both the single tine, in which the single tine is utilized for the same proof mass configuration, and the double tine for the opposite proof mass configuration is presented.

##### **4.1.1 Frequency Response Test Setup**

The frequency response tests are performed in the vacuum chamber. A network analyzer is used to characterize the device under test. The network analyzer generates a sine shape drive signal to excite and move the tines by electrostatic actuation. A

trans-impedance amplifier converts the created response current to voltage and fed back to the network analyzer. By comparing the transmitted and reflected signals coming from the sensors, the characterization of the sensor is performed. The schematic of the test setup is in Figure 4.1.

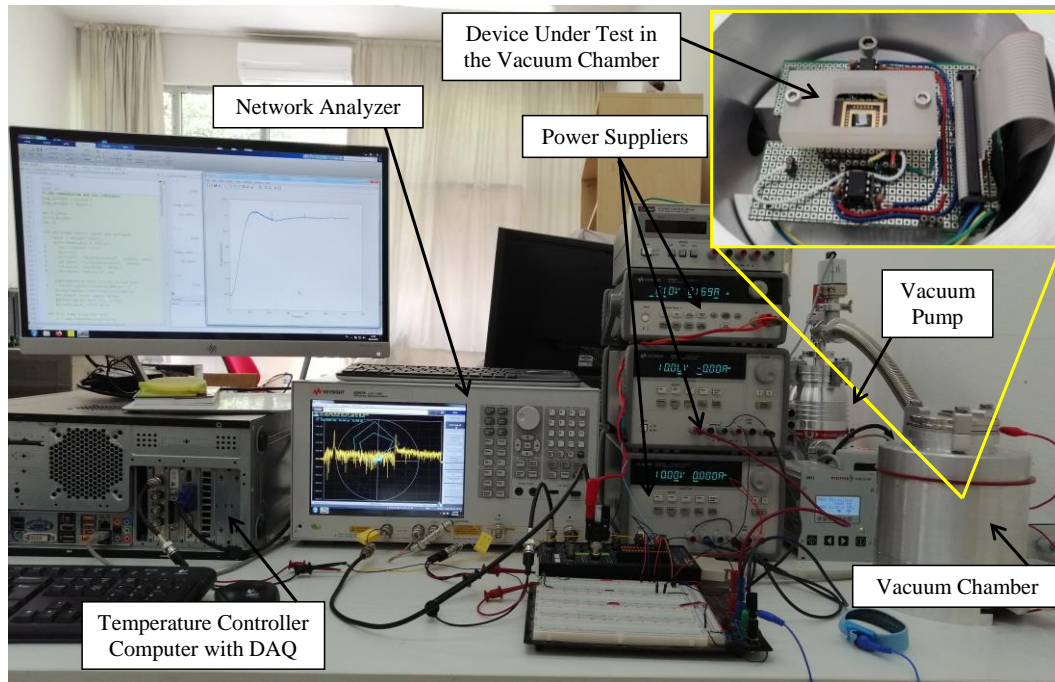


Figure 4.1. Frequency response setup

The ambient pressure in the vacuum chamber is around 0.25mTorr. In this frequency response tests, Agilent E5061B Network Analyzer is used to obtain the frequency response plots by generating a drive signal, which is a sine wave having  $2mV_{pp}$ (peak to peak) voltage and receiving the sense signal. Commercial LF353 operational amplifiers are used as the trans-impedance amplifiers, having  $1M\Omega$  feedback resistances. These TIAs are put next to the sensor in the vacuum chamber to decrease the noise level in the measurements. The proof mass voltages and op-amp supply voltages are provided with power supplies. By changing the proof mass voltages from the power supply, the effect of the electrostatic coupling on frequency response plots is investigated. During the frequency response tests, the response for the zero proof mass voltages is obtained to cancel the feedthrough capacitance of the

circuitry. Thus, only the mechanical response of the resonator is obtained by subtracting. The IF bandwidth for the sampling is selected as 15Hz.

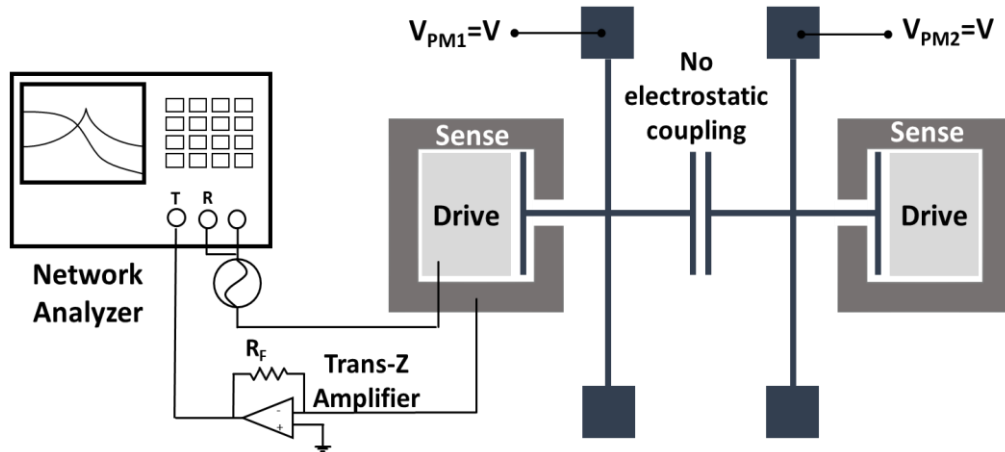


Figure 4.2. Schematic view of the frequency response test setup for the single tine is utilized with the same proof mass configuration.

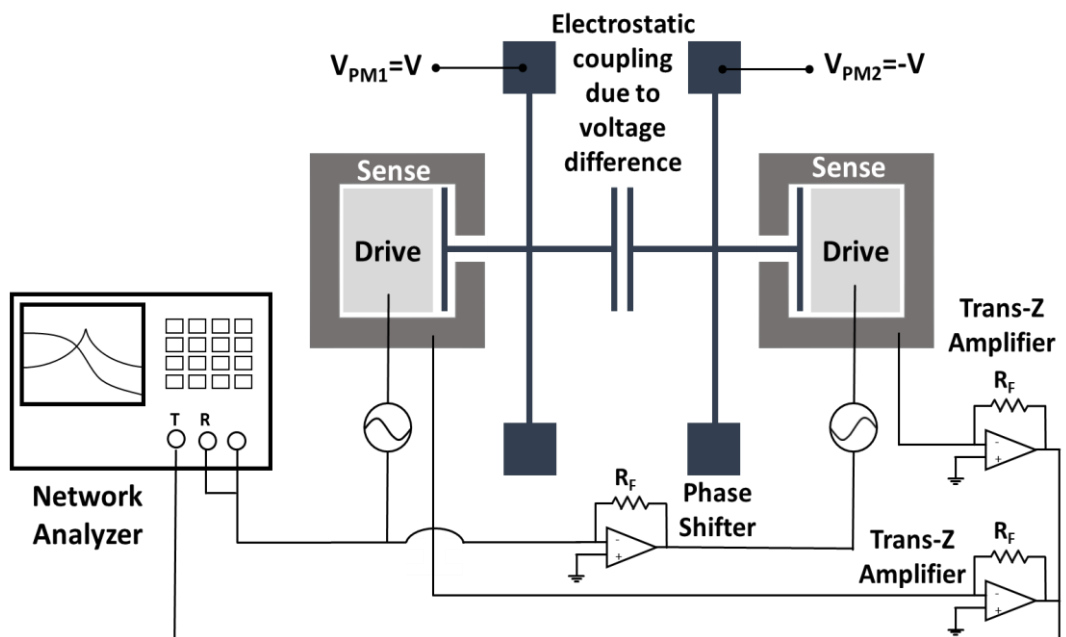


Figure 4.3. Schematic view of the frequency response test setup for both tines is utilized with the opposite proof mass configuration.

### 4.1.2 Frequency Response Test Results

The frequency response test results are obtained by the test procedure, which is explained in the previous section. The feedthrough in the system is subtracted from the response. The frequency response plots represent only the electro-mechanical characteristic of the resonant system. The frequency span is kept very wide to find the modes of interests which are the out of and in phase modes for the changing voltages. This characterization tests under the room temperature of 25°C.

Firstly, the effect of the increasing proof mass voltage is studied for the same proof mass configuration, where the single tine is actuated and sensed, whose schematic view is given in Figure 4.2. As it is seen from Figure 4.4, the increasing proof mass voltage on both tines decreases the resonance frequency of the resonator. Moreover, since the proof mass voltage increases, the output signal gets more potent as expected. In this configuration, since the proof mass voltages of both tines are the same, there is no electrostatic coupling.

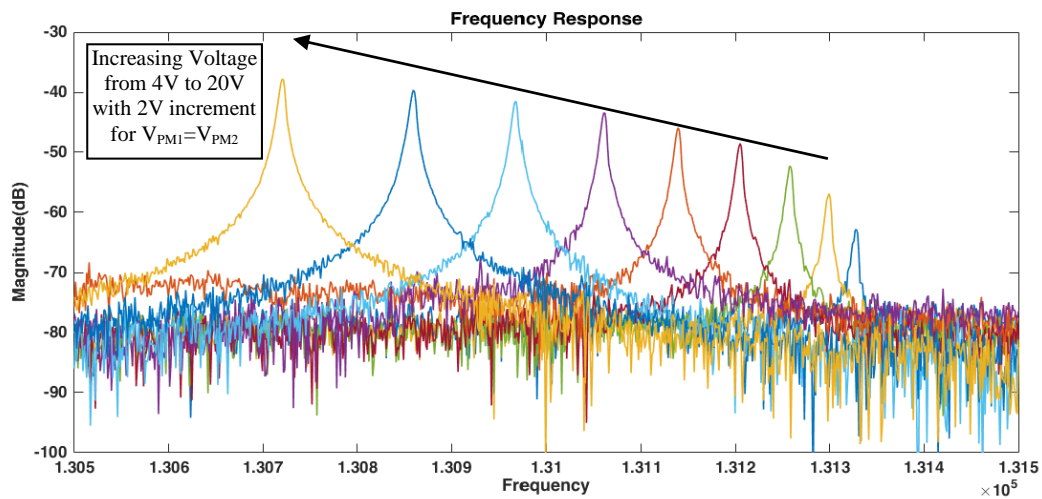


Figure 4.4. Frequency Response Graph for  $V_{PM1}=V_{PM2}$

In Figure 4.5, the frequency response for the opposite sign voltage configuration for various voltages, whose schematic is given in Figure 4.3 is presented. In this configuration, there is an electrostatic coupling between the capacitive plates. This

coupling behaves as a negative spring constant, which is the most critical part of this thesis. In two degree of freedom mass-spring-damper systems, the in-phase mode frequency is lower than the out-of-phase mode frequency, as it is explained in Section 2.3. When a negative spring constant between the resonant masses is defined, the mode-ordering, which is the change of the in-phase and the out-of-phase mode orders, can be done. Therefore, the operational out-of-phase mode frequency can be pushed down very close to the pull-in state without pull-in of the in phase-mode. Thus, the resonator can be operated at higher sensitivity.

As it is seen from Figure 4.5, the level of the output signals increases with the increasing voltage magnitude as expected. The resonance frequency for the out-of-phase mode is lower than the in-phase mode frequency, thanks to mode ordering. Besides, as the voltage difference increases, the out-of-phase mode frequency shifts faster than the in-phase mode, which agrees with the analytical and the finite element model. In testing, since there is a limited amount of fabricated sensor, the proof mass voltages are kept in the safe region, to prevent the pull-in of the resonators due to high voltage. The maximum applied voltages are  $V_{PM1}=20V$  and  $V_{PM2}=-20V$ , although the analytical and FEM analysis show that the pull-in voltage is around 50V.

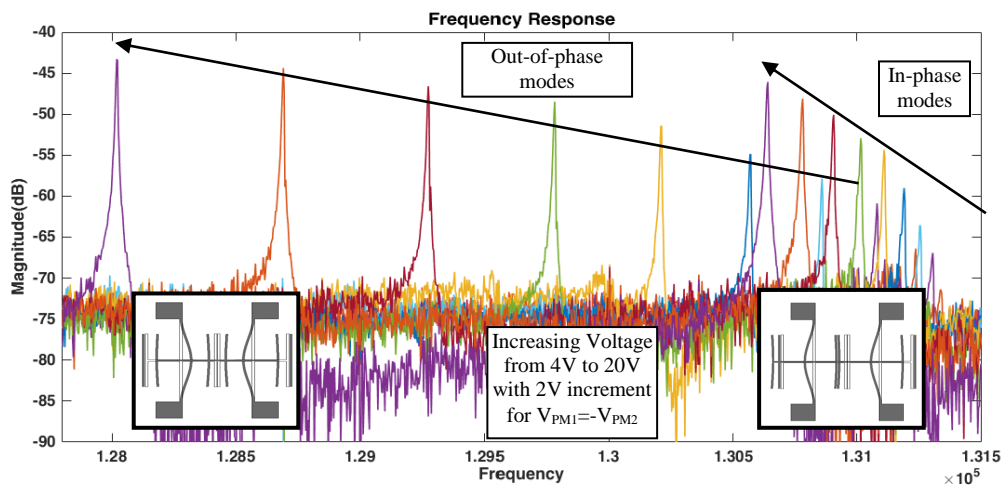


Figure 4.5. Frequency Response Graph for  $V_{PM1}=-V_{PM2}$

Figure 4.6 belongs to the resonance frequency for the out-of-phase mode for  $V_{PM1}=20V$  and  $V_{PM2}=-20V$  with a quality factor around 25500, which is a dimensionless parameter which defines the ratio of the stored energy at the resonance to energy lost per cycle. The IF bandwidth of the quality factor analysis is selected as the 5Hz.

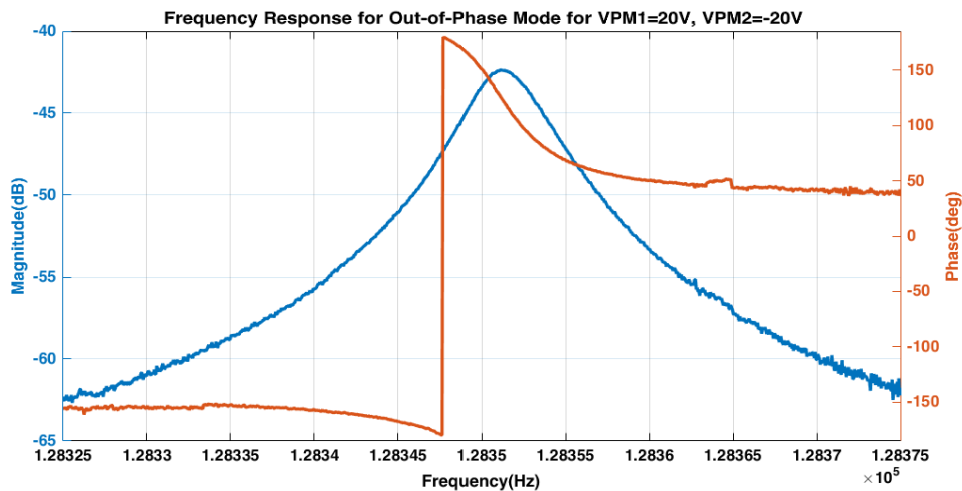


Figure 4.6. The close view of the frequency response plot to see the quality factor for the out-of-phase mode.

## 4.2 System-Level Test

The system-level tests are performed by changing the temperature of the resonator in the vacuum chamber. The frequency response of the system is used for the analysis. For various proof mass configurations, by looking at the peak of the magnitude plots, frequency change versus temperature change graphs are obtained. The sensitivity analysis is presented at the end with the comparison of the same proof mass configuration where the single tine is utilized and the opposite proof mass configuration where the dual tine is used with the electrostatic coupling.

### 4.2.1 System-Level Test Setup

The temperature of the device in the vacuum chamber is controlled with a proportional-integral controller. A thermoelectric heater is used under the device to provide heat to the system. The temperature is controlled with a current fed to the thermoelectric heater. A commercial LM35 temperature sensor is placed just between the device package and the thermoelectric heater to measure the temperature. The temperature measurement is done with PCI 4461 data acquisition board in the MATLAB environment. Then, in the same software environment by running the PI controller code, which is in Appendix A, a current command is sent to the E3640A using a GPIB interface to control the heat supplied by the thermoelectric heater to the system. After setting the test temperature from the MATLAB environment, the settling of the temperature has waited. The schematic view of the heater, sensor and device under test is given in Figure 4.7.

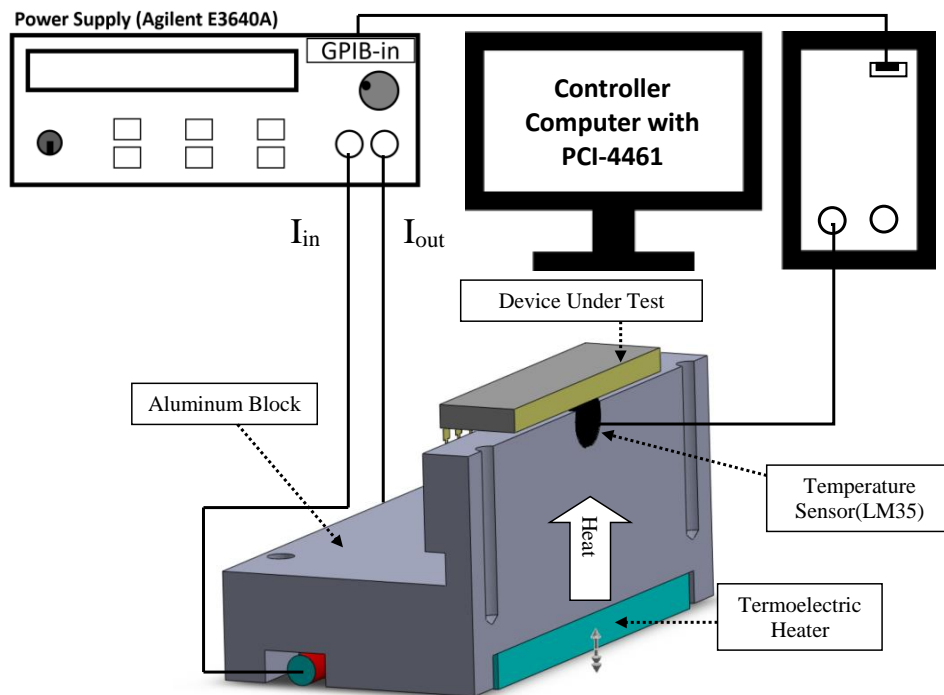


Figure 4.7. Schematic of the temperature controller setup with the device under test.

### 4.2.2 System-Level Test Results

In the system-level test, frequency response plots are obtained at different temperatures for both same and the opposite sign proof mass voltage configurations as in Figure 4.2 and Figure 4.3, respectively. The response of the sensor is in agreement with the analytical and the finite element model. The temperature increment is 5°C, starting from the 25°C to 65°C. The dark blue curves represent 25°C, and the red curves represent 65°C. The other colours belong to intermediate temperature steps.

Firstly, the same proof mass configuration, whose schematic is given in Figure 4.2, temperature tests are performed. In the frequency response graphs, since the frequency change due to various proof mass voltages is very small, plots are very close to each other. Therefore, only temperature graphs belong to two proof mass voltage graphs are presented, which are 10V and 20V in

Figure 4.8. Since the thermal expansion coefficient of the glass substrate is higher than the thermal expansion coefficient of the silicon device, the temperature increase causes an axial force on the resonant structure. Therefore, the resonance frequency of the device for the given proof mass configuration increases with the increasing temperature as it is seen from the graph. Moreover, it is also observed that higher the proof mass voltage, the response amplitudes also increase as in Figure 4.4.

In Figure 4.9 and Figure 4.10, frequency change versus temperature change graphs is presented. It is seen that the frequency change is linear with the temperature change for both cases. The expected behaviour of the sensitivity for the same proof mass configuration in which the single tine is utilized is the increase in the sensitivity with increasing voltage. However, the overall behaviour of the single tine same proof mass configuration given in Figure 4.16 presents that the sensitivity increases starts after 18V proof mass voltages. The reason for this might be the error is data sampling or the residual stress coming from the anodic bonding phase.

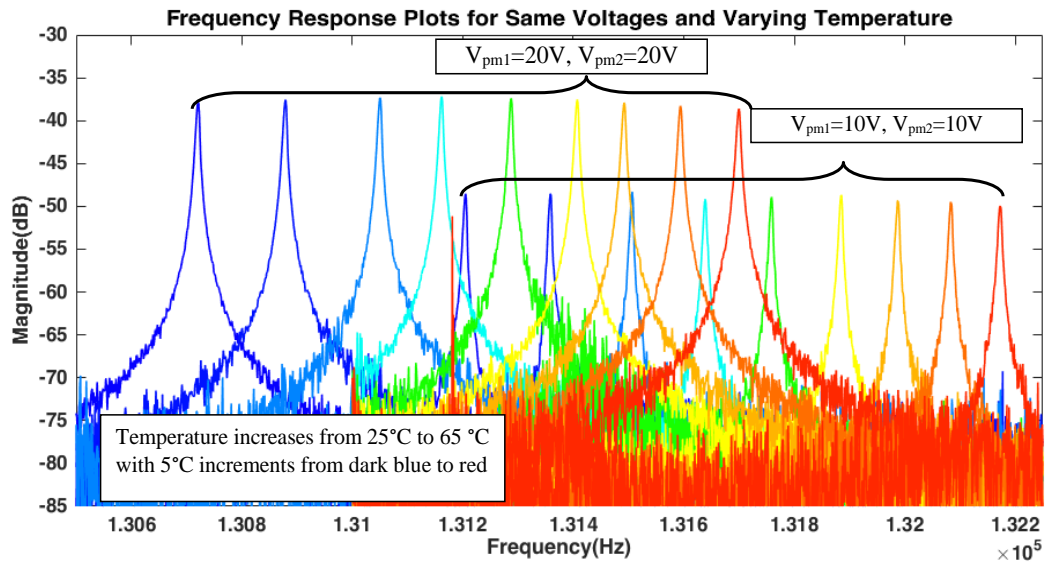


Figure 4.8. Frequency response plots for various temperatures for same proof mass configuration.

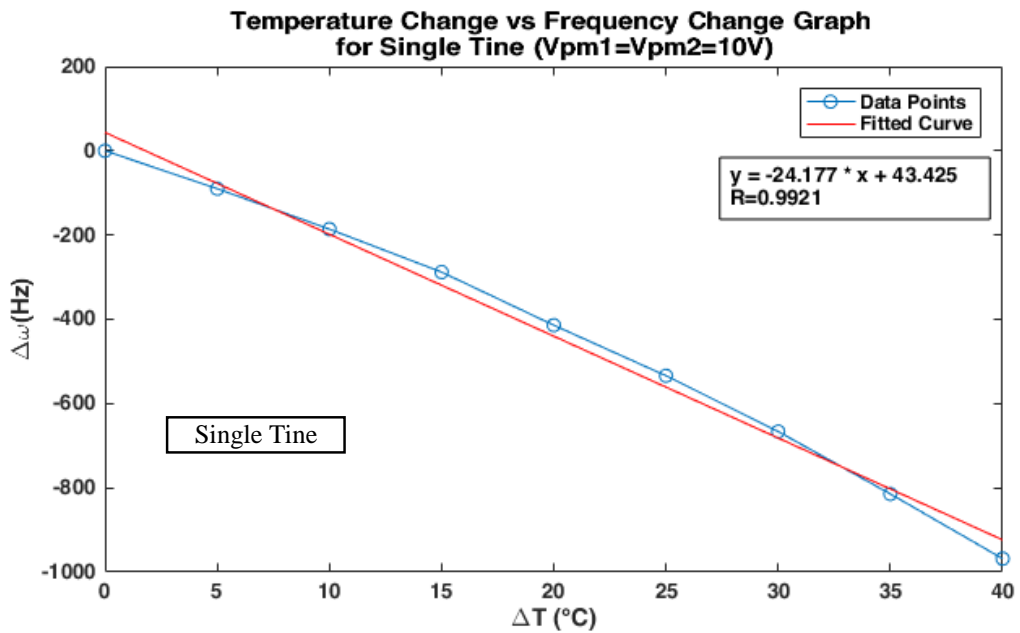


Figure 4.9. System-level test result for DETF resonator for single tine where 10V proof mass voltages applied on both tines

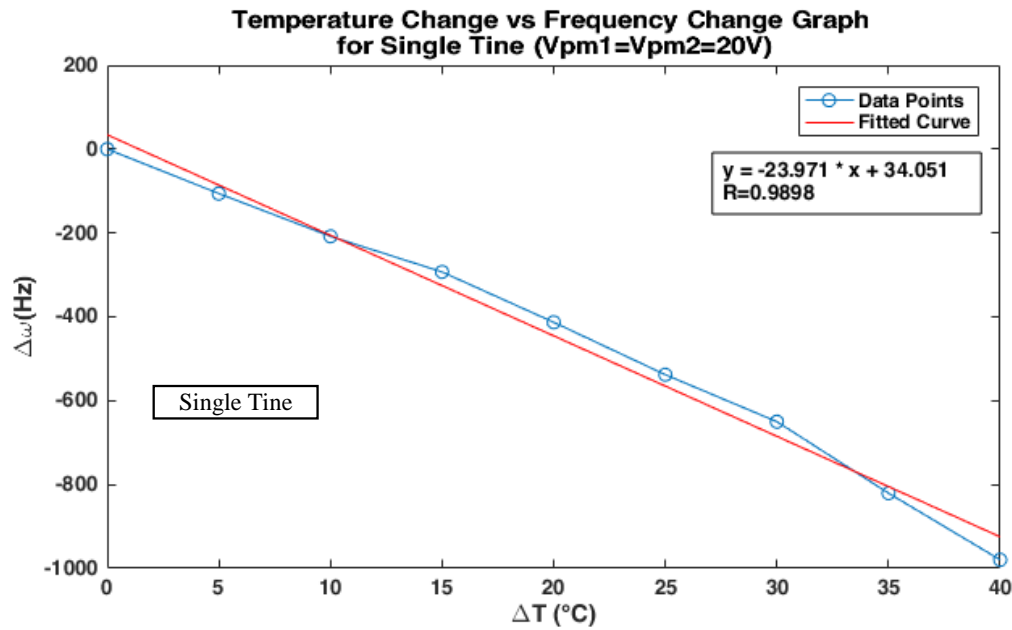


Figure 4.10. System-level test result for DETF resonator for single tine where 20V proof mass voltages applied on both tines

After the single tine same proof mass configuration system-level tests, the proof mass voltages are adjusted for the opposite proof mass configuration. By changing the temperature and proof mass voltages of the tines, data is collected. As the previous sampling, all data is sampled in .csv format and handled by MATLAB. For dual tine opposite proof mass configuration, since there is electrostatic coupling, the significant decrease in resonance frequency with increasing proof mass voltage is expected. Due to the electrostatic coupling between the tines, mode-ordering is expected. Besides, for the system level tests, the change of the out-of phase-mode frequency is expected to be higher than the in-phase mode frequency change in accordance with the analytical and FEM model. The frequency response plots for the dual tine- opposite proof mass configuration results are given in Figure 4.11. The other proof mass voltage results are not presented since the resonant peaks, especially for the in-phase modes are very close to each other and makes the graph complicated. The sensitivity results are given in the following figures. The overall sensitivity of the system-level tests are given in Figure 4.16

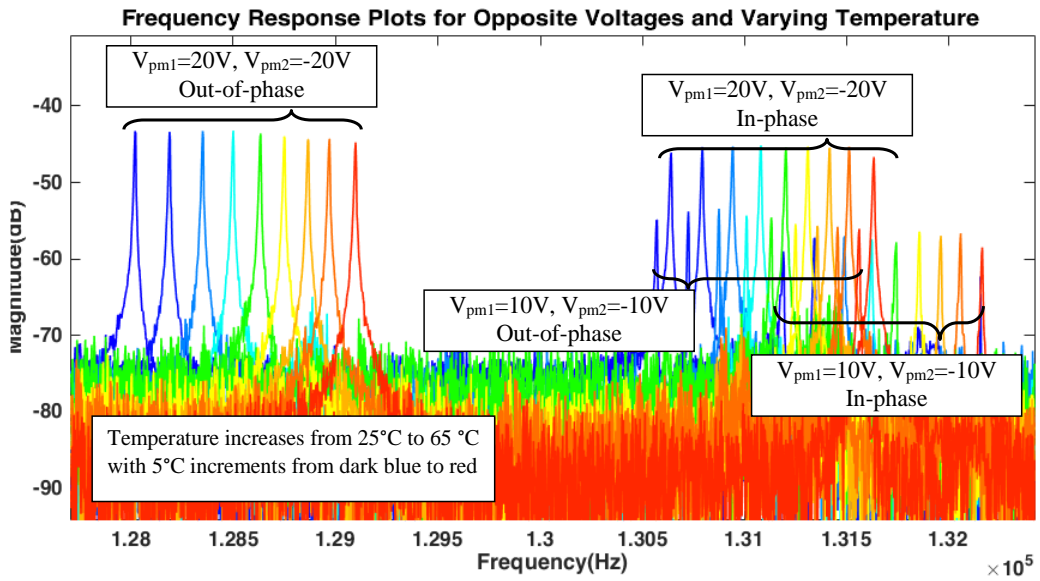


Figure 4.11. Frequency response plots for various temperatures for opposite sign proof mass configuration.

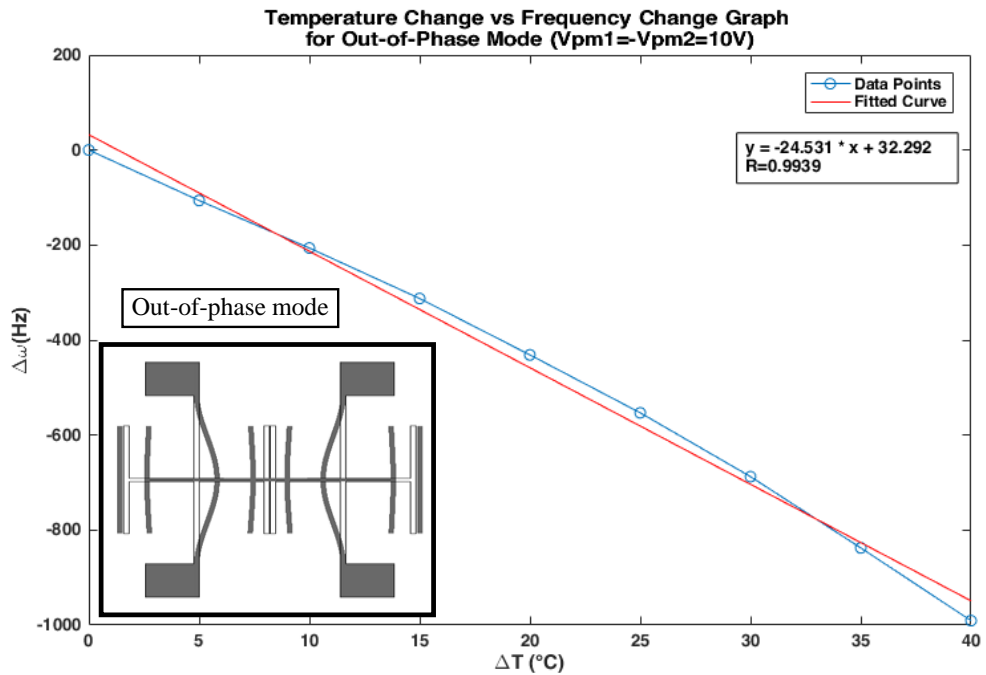


Figure 4.12. The system-level test result of DETF resonator for dual tines with the opposite proof mass configuration for the out-of-phase mode ( $V_{PM1}=10V, V_{PM2}=-10V$ )

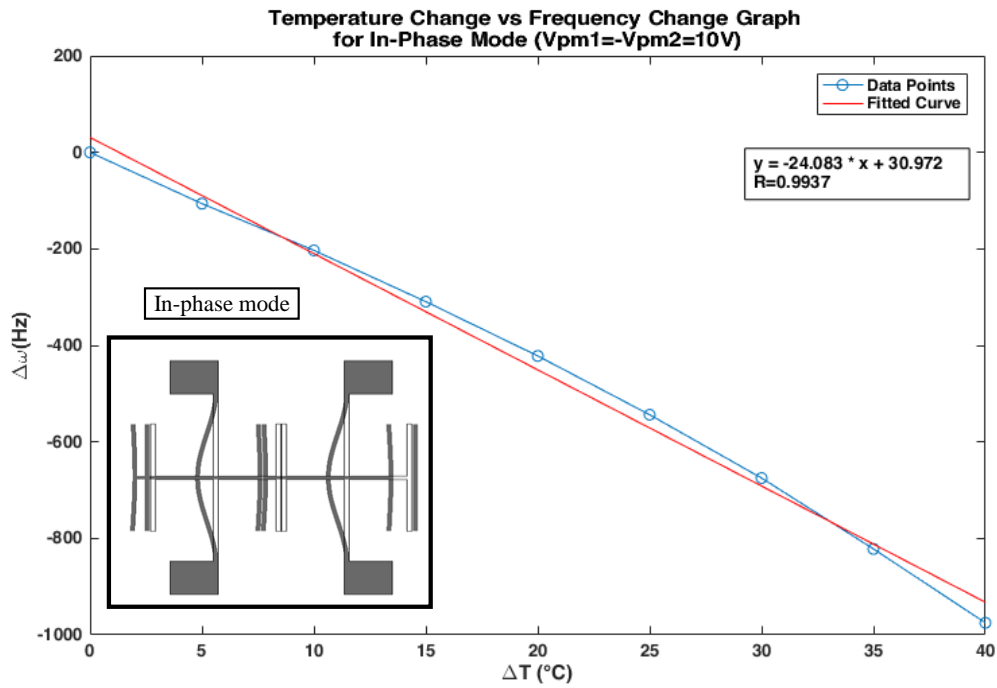


Figure 4.13. The system-level test result of DETF resonator for dual tines with the opposite proof mass configuration for the in-phase mode ( $V_{PM1}=10V$ ,  $V_{PM2}=-10V$ )

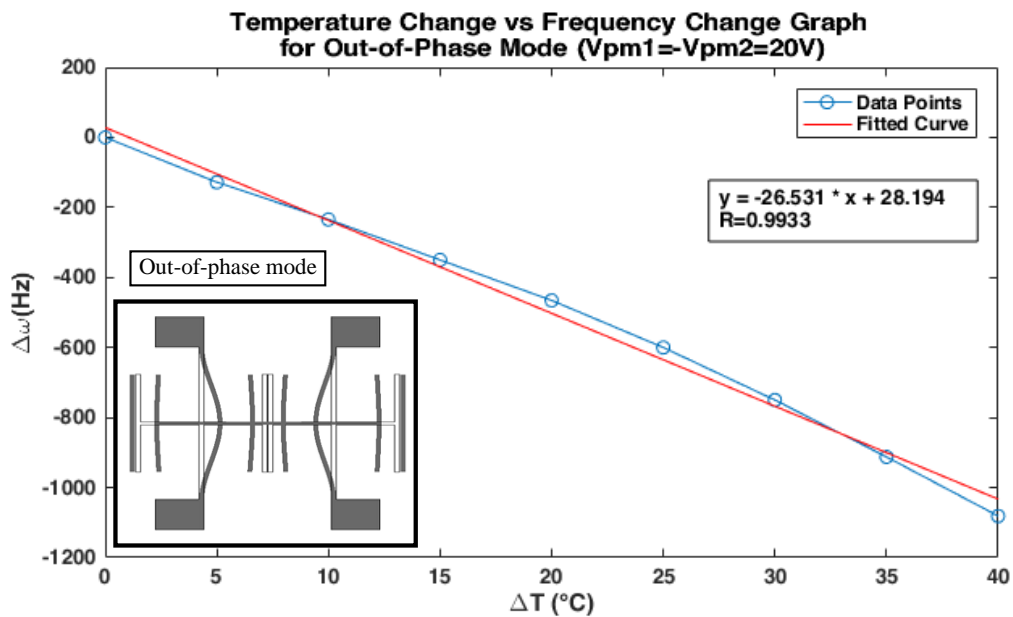


Figure 4.14. The system-level test result of DETF resonator for dual tines with the opposite proof mass configuration for the out-of-phase mode ( $V_{PM1}=20V$ ,  $V_{PM2}=-20V$ )

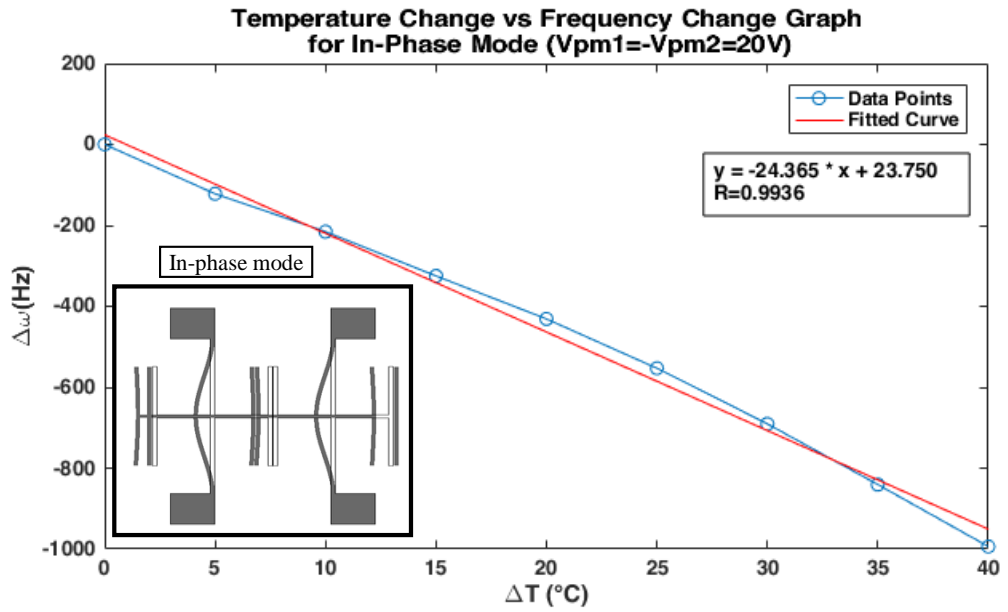


Figure 4.15. The system-level test result of DETF resonator for dual tines with the opposite proof mass configuration for the in-phase mode ( $V_{PM1}=20V$ ,  $V_{PM2}=-20V$ )

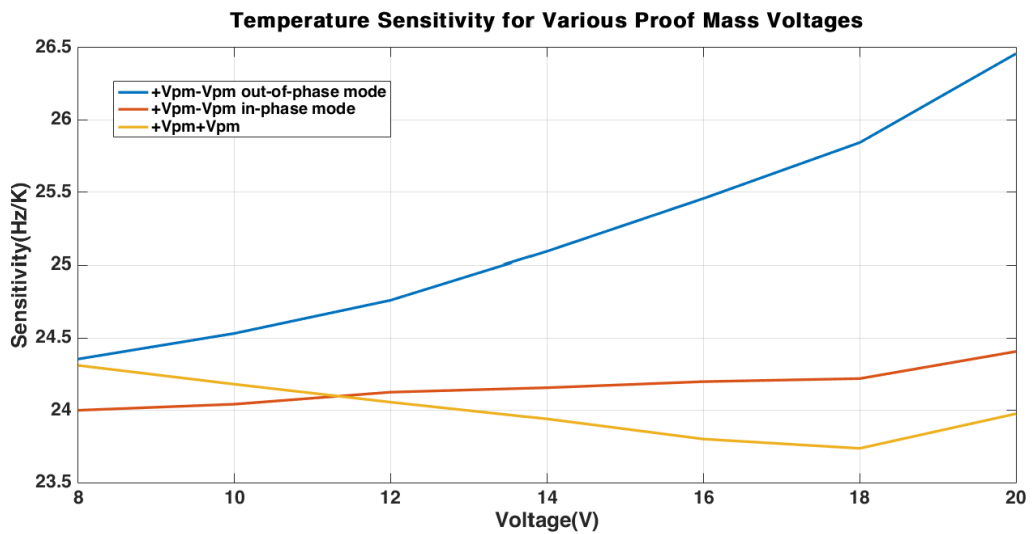


Figure 4.16. Temperature sensitivity versus proof mass voltage graph for the in-phase mode of opposite sign, out-of-phase mode of opposite sign and same sign proof mass voltage configurations.

The temperature sensitivity of the resonator for the various proof mass voltages and both voltage configuration is obtained by taking the maximum values of the frequency response graphs. The results show that for the dual tine opposite sign proof

mass configuration, the sensitivity improvement of the out-of-phase mode is greater than the in-phase mode. The sensitivity of the out of phase mode increases nonlinearly as the proof mass voltage approaches the pull-in voltage as it is seen from Figure 4.16. The sensitivity for dual tine out-of-phase mode is also higher than the in-phase mode sensitivity and the single tine sensitivity.

### **4.3 Summary**

This chapter has presented the characterization and the system level test results of DETF MEMS resonant temperature sensor. All tests are performed in a vacuum environment. The system-level tests are performed by a temperature controller and after the temperature is stabilized. At a pressure level of 0.25mTorr, a quality factor around 25500 for the operation out-of-phase mode is obtained. For single tine same proof mass configuration and dual tine opposite sign proof mass configuration, frequency response analyses are performed to see the effect of the increasing proof mass configuration and temperature difference. In proof mass voltage analysis, it is seen that resonance frequency drops for increasing voltage in both configuration and both modes of the dual tine configuration.

In system-level tests, the effect of increasing temperature is observed as the resonance frequency increase due to thermally induced axial force on the resonant structure. In dual tine configuration, since there is negative electrostatic between the tines, the out of phase mode frequency dropped below the in-phase frequency as expected. The temperature sensitivity of the in-phase mode for dual tine opposite sign proof mass configuration increased from and 24Hz/K to 24.4Hz/K with the voltage increase from 8V to 20V. The temperature sensitivity of the out-of-phase mode for dual tine opposite sign proof mass configuration increased from 24.4Hz/K to 26.5Hz/K with the voltage increase from 8V to 20V, which is a better improvement than the in-phase mode. Besides, as it is seen from Figure 4.16, the increase in sensitivity is nonlinear, since the proof mass voltages are getting close to the pull-in voltage. The achieved sensitivities are not the best sensitivities in the

literature but, in addition to the analytical and FEM analysis, test results show that the temperature sensitivity can be increased by varying coupling stiffness by adjusting the proof mass voltages close to pull-in voltage and mode-ordering.

The differences between the analytical and test results might be based upon:

- The fabricated device dimensions are deviated from the desired values due to lithography and DRIE fabrication steps due to undercut. The undercut on the resonance structures decreases the resonance frequency in agreement with the analytical model.
- The analytical model assumes that capacitive plates move rigidly during the resonance motion. However, these plates have a nonlinear deflection pattern, whose nonlinearity enhances with the increasing voltage.



## CHAPTER 5

### CONCLUSION AND FUTURE WORKS

This study presents an electrostatically coupled double-ended tuning fork MEMS resonator as a temperature sensor. In Chapter 2, the basic operation principles of the resonator are explained with the derivations. The effect of the electrostatic coupling stiffness on the sensor performance is demonstrated. The analytical model is verified with finite element simulations. Modal analysis, electro-mechanical and thermo-electro-mechanical analysis are performed. The fabrication of the MEMS resonator is examined with the simplified view of the process flow, and the fabricated device is presented in Chapter 3. In Chapter 4, the test results, which belongs to the characterization of the temperature sensor, are shown. The conclusions obtained from this research are summarized as follows:

- The basic operation principles of the resonant type MEMS sensors with actuation, detection and electrostatic coupling principles are investigated with derivations. The effect of the electrostatic coupling is presented with equations. Besides, the pull-in phenomenon is explained since it is the limiting factor for the electrostatic coupling phenomenon.
- The effect of the coupling stiffness on the operational modes, which are in-phase and out-of-phase modes, are investigated. It is shown that in the presence of a negative electrostatic coupling stiffness, the out-of-phase mode frequency drops below the in-phase mode frequency, which is called as mode-ordering. The idea of the sensitivity improvement by controlling the proof mass voltages for out-of-phase mode (operational mode) of opposite proof mass configuration is presented.
- The utilization of a double ended-tuning fork resonator as a temperature sensor is explained. The related thermal strain equation, the thermally

induced axial force equation on the tines and their effect on the resonance frequencies are derived.

- The effect of the temperature change of the operational modes, which are in-phase and out-of-phase modes, are investigated.
- Finite element modelling of the existing system is performed. Pull-in analysis is done to prevent the failure of the resonator. Although the system operates at resonance, static deflection analysis is performed to verify the pull-in analysis and show the nonlinearity due to increasing proof mass voltage. The analytical model is verified with the modal analysis. The effect of the proof mass voltage on the desired modes is studied with the electro-mechanical model.
- The effect of the temperature change on the system is studied with the thermo-electro-mechanical model. The operational mode frequencies are obtained with the modal analysis for the given temperature change and the applied proof mass voltage. The results are compared with the analytical model.
- The fabrication of the double ended-tuning fork resonator is performed in METU MEMS Center with silicon on glass method, which is a similar method with aMEMS process. The process flow of the device is illustrated and explained briefly. The fabrication results are presented with SEM images. The difference between the designed sensor and fabrication results are discussed.
- The characterization of the device is performed in the vacuum chamber at a pressure of around 0.15mTorr. The quality factor for the out-of-phase mode is about 25500. Resonance frequencies for the mode of interests of the resonator are close to the analytical model and the FEM simulation results. The effect of the electrostatic softening effect is investigated for the same and the opposite sign proof mass voltage configurations. The frequency change for the opposite sign proof mass configuration from 6V to 20V is 3063Hz and 666Hz for out-of-phase and in-phase, respectively. For the same proof

mass configuration, the resonance shifts 579Hz. In the system level tests, the temperature is increased using a PI controller, and the frequency response plots are obtained for both proof mass configurations and various voltages. The out-of-phase mode and the in-phase mode frequency changes for the temperature increase from 25°C to 65°C are 1078Hz and 988 Hz for the  $V_{PM1}=20V$  and  $V_{PM2}=-20V$ . For the same proof mass configuration ( $V_{PM1}=20V$  and  $V_{PM2}=20V$ ), the frequency change is 986Hz, still lower than the in-phase mode frequency of the opposite sign proof mass voltage configuration but very close as expected. When the overall sensitivities are observed, which are obtained from the maxima of the frequency response plots, it is seen that for the opposite sign proof mass configuration, the out-of-phase and the in-phase temperature sensitivity are increased from 24.4Hz/K to 26.5Hz/K and 24Hz/K to 24.4Hz/K, respectively, with the voltage increase from 8V to 20V.

- The achieved sensitivities are not the best sensitivities in the literature but, in addition to the analytical and FEM analysis, test results show that the temperature sensitivity can be increased by varying coupling stiffness by adjusting the proof mass voltages close to pull-in voltage and mode-ordering.

By using the electrostatic softening effect, in other words, variable coupling stiffness, the temperature sensitivity of the double ended-tuning fork MEMS resonator is improved. The performance and applications of the MEMS temperature sensor can be enhanced as a future work listed below:

- The main idea is utilizing the thermal expansion coefficient difference of the substrate and the resonator in this study. The material used in the fabrication can be changed. Using the materials, which have a higher thermal expansion coefficient difference, will improve the sensitivity by amplifying the thermally induced axial force on the MEMS resonators.
- The effect of the variable coupling stiffness, which uses the electrostatic softening, increases as the proof mass voltages come closer to the pull-in

voltages. Therefore, the resonance characteristic becomes highly nonlinear. The higher sensitivities can be obtained by a more realistic analytical model with nonlinear analysis and operating the resonator just before the pull-in state.

- The phase-locked-loop control circuitry can be set up for a more precise sensitivity analysis.
- The measurement of the actual temperature is critical for the characterization. Therefore, a laser thermometer, which measures the temperature of the substrate directly, can give better results.
- Although the temperature of the setup is controlled with a PI controller, a high precision oven or placing the temperature sensor close to the package will give more precise temperature measurements.
- Due to the fabrication imperfections, the targeted dimensions deviate. These imperfections can be included in the analytical and the finite element models with the nonlinear behaviour to operate the resonator closer to the buckling state.

## REFERENCES

- [1] R. Miller, L. Minnich, J. Nelson, B. Bachelder, and J. Glass, *Specifications, Tolerances, and Other Technical Requirements for Weighing and Measuring Devices*. 2020.
- [2] G. E. Moore, “Cramming more components onto integrated circuits,” *Proc. IEEE*, vol. 86, no. 1, pp. 82–85, 1998, doi: 10.1109/JPROC.1998.658762.
- [3] J. Zhu *et al.*, “Development trends and perspectives of future sensors and MEMS/NEMS,” *Micromachines*, vol. 11, no. 1, 2020, doi: 10.3390/mi11010007.
- [4] I. Arc, “MEMS Market - Forecast(2020 - 2025).” [Online]. Available: <https://www.industryarc.com/Report/15575/mems-market.html>. [Accessed: 08-May-2020].
- [5] K. Azgin, T. Akin, and L. Valdevit, “Ultrahigh-dynamic-range resonant MEMS load cells for micromechanical test frames,” *J. Microelectromechanical Syst.*, vol. 21, no. 6, pp. 1519–1529, 2012, doi: 10.1109/JMEMS.2012.2211576.
- [6] H. Ding, J. Zhao, B. Ju, and J. Xie, “A highly sensitive biaxial resonant accelerometer with two-stage microleverage mechanisms,” in *2016 IEEE 29th International Conference on Micro Electro Mechanical Systems (MEMS)*, 2016, pp. 934–937, doi: 10.1109/MEMSYS.2016.7421785.
- [7] A. L. Herrera-May *et al.*, “A resonant magnetic field microsensor with high quality factor at atmospheric pressure,” *J. Micromechanics Microengineering*, vol. 19, no. 1, 2009, doi: 10.1088/0960-1317/19/1/015016.
- [8] R. a Wickstrom and J. R. Davis, “Gate Transistor,” *IEEE Trans. Electron Devices*, vol. 14, no. 3, pp. 117–133, 1967, doi: 10.1109/T-ED.1967.15912.
- [9] R. J. Halford, “Pressure Measurement Using Vibrating Cylinder Pressure Transducer,” *Instrum. Pract.*, vol. 18, pp. 823–829, 1984.

- [10] G. Stemme, “Resonant silicon sensors,” *J. Micromechanics Microengineering*, vol. 1, no. 2, pp. 113–125, 1991, doi: 10.1088/0960-1317/1/2/004.
- [11] Y. Lu and D. A. Horsley, “Modeling, Fabrication, and Characterization of Piezoelectric Micromachined Ultrasonic Transducer Arrays Based on Cavity SOI Wafers,” *J. Microelectromechanical Syst.*, vol. 24, no. 4, pp. 1142–1149, 2015, doi: 10.1109/JMEMS.2014.2387154.
- [12] K. L. Ekinici, Y. T. Yang, and M. L. Roukes, “Ultimate limits to inertial mass sensing based upon nanoelectromechanical systems,” *J. Appl. Phys.*, vol. 95, no. 5, pp. 2682–2689, 2004, doi: 10.1063/1.1642738.
- [13] G. Piazza, P. J. Stephanou, and A. P. Pisano, “One and two port piezoelectric higher order contour-mode MEMS resonators for mechanical signal processing,” *Solid. State. Electron.*, vol. 51, no. 11–12, pp. 1596–1608, 2007, doi: 10.1016/j.sse.2007.09.037.
- [14] H. Zhu, G. C. Shan, C. H. Shek, and J. E. Y. Lee, “Shear dependent nonlinear vibration in a high quality factor single crystal silicon micromechanical resonator,” *Appl. Phys. Lett.*, vol. 101, no. 3, 2012, doi: 10.1063/1.4737213.
- [15] J. Basu and T. Bhattacharyya, “Microelectromechanical Resonators for Radio Frequency Communication Applications,” *Microsyst. Technol.*, vol. 17, pp. 1557–1580, Oct. 2011, doi: 10.1007/s00542-011-1332-9.
- [16] Y. W. Lin, S. S. Li, Z. Ren, and C. T. C. Nguyen, “Low phase noise array-composite micromechanical wine-glass disk oscillator,” *Tech. Dig. - Int. Electron Devices Meet. IEDM*, vol. 2005, no. c, pp. 278–281, 2005, doi: 10.1109/iedm.2005.1609328.
- [17] T. A. W. Roessig, “Integrated MEMS Tuning Fork Oscillators for Sensor Applications,” Berkeley, 1998.
- [18] S. C. Chang, M. W. Putty, D. B. Hicks, C. H. Li, and R. T. Howe, “Resonant-bridge two-axis microaccelerometer,” *Sensors Actuators A Phys.*, vol. 21, no.

- 1, pp. 342–345, 1990, doi: [https://doi.org/10.1016/0924-4247\(90\)85068-F](https://doi.org/10.1016/0924-4247(90)85068-F).
- [19] Y. L. Zhu, S. R. Wang, and A. P. Qiu, “Design and Simulation of a DETF for Use in a Resonant Gyroscope,” *Key Eng. Mater.*, vol. 295–296, pp. 113–118, 2005, doi: [10.4028/www.scientific.net/KEM.295-296.113](https://doi.org/10.4028/www.scientific.net/KEM.295-296.113).
- [20] S. Pala, M. Çiçek, and K. Azgin, “A Lorentz force MEMS magnetometer,” in *2016 IEEE SENSORS*, 2016, pp. 1–3, doi: [10.1109/ICSENS.2016.7808507](https://doi.org/10.1109/ICSENS.2016.7808507).
- [21] X. Du, L. Wang, A. Li, L. Wang, and D. Sun, “High Accuracy resonant pressure sensor with balanced-mass DETF resonator and twinborn diaphragms,” *J. Microelectromechanical Syst.*, vol. 26, no. 1, pp. 235–245, 2017, doi: [10.1109/JMEMS.2016.2632108](https://doi.org/10.1109/JMEMS.2016.2632108).
- [22] O. Kaya, T. Köse, and K. Azgin, “Integrated Temperature Sensor for Temperature Compensation of Inertial Sensors,” in *2019 IEEE International Symposium on Inertial Sensors and Systems (INERTIAL)*, 2019, pp. 1–2, doi: [10.1109/ISISS.2019.8739559](https://doi.org/10.1109/ISISS.2019.8739559).
- [23] T. Kose, “DEVELOPMENT OF AN INTEGRATED RESONANT MEMS TEMPERATURE SENSOR,” 2016.
- [24] P. Thiruvankatanathan, J. Yan, and A. A. Seshia, “Ultrasensitive mode-localized micromechanical electrometer,” in *2010 IEEE International Frequency Control Symposium, FCS 2010*, 2010, pp. 91–96, doi: [10.1109/FREQ.2010.5556368](https://doi.org/10.1109/FREQ.2010.5556368).
- [25] P. Pai, H. Pourzand, and M. Tabib-Azar, “Magnetically coupled resonators for rate integrating gyroscopes,” in *Proceedings of IEEE Sensors*, 2014, vol. 2014-Decem, no. December, pp. 1173–1176, doi: [10.1109/ICSENS.2014.6985217](https://doi.org/10.1109/ICSENS.2014.6985217).
- [26] B. E. DeMartini, J. F. Rhoads, M. A. Zielke, K. G. Owen, S. W. Shaw, and K. L. Turner, “A single input-single output coupled microresonator array for the detection and identification of multiple analytes,” *Appl. Phys. Lett.*, vol. 93, no. 5, pp. 2006–2009, 2008, doi: [10.1063/1.2964192](https://doi.org/10.1063/1.2964192).

- [27] M. Manav, G. Reynen, M. Sharma, E. Cretu, and A. S. Phani, “Ultrasensitive resonant MEMS transducers with tuneable coupling,” *J. Micromechanics Microengineering*, vol. 24, no. 5, 2014, doi: 10.1088/0960-1317/24/5/055005.
- [28] M. Spletzer, A. Raman, A. Q. Wu, X. Xu, and R. Reifenberger, “Ultrasensitive mass sensing using mode localization in coupled microcantilevers,” *Appl. Phys. Lett.*, vol. 88, no. 25, 2006, doi: 10.1063/1.2216889.
- [29] C. Zhao, G. S. Wood, J. Xie, H. Chang, S. H. Pu, and M. Kraft, “A force sensor based on three weakly coupled resonators with ultrahigh sensitivity,” *Sensors Actuators, A Phys.*, vol. 232, pp. 151–162, 2015, doi: 10.1016/j.sna.2015.05.011.
- [30] P. Thiruvengatanathan, J. Yan, J. Woodhouse, and A. A. Seshia, “Enhancing parametric sensitivity in electrically coupled MEMS resonators,” *J. Microelectromechanical Syst.*, vol. 18, no. 5, pp. 1077–1086, 2009, doi: 10.1109/JMEMS.2009.2025999.
- [31] P. W. Anderson, “Absence of Diffusion in Certain Random Lattices,” *Phys. Rev.*, vol. 109, no. 5, pp. 1492–1505, Mar. 1958, doi: 10.1103/PhysRev.109.1492.
- [32] C. Zhao, “A MemS sensor for stiffness change sensing application based on three weakly coupled resonators,” *Sot. Phd*, 2016.
- [33] P. Thiruvengatanathan, J. Woodhouse, J. Yan, and A. A. Seshia, “Manipulating vibration energy confinement in electrically coupled microelectromechanical resonator arrays,” *J. Microelectromechanical Syst.*, vol. 20, no. 1, pp. 157–164, 2011, doi: 10.1109/JMEMS.2010.2090501.
- [34] S. Ilyas and M. I. Younis, “Theoretical and experimental investigation of mode localization in electrostatically and mechanically coupled microbeam resonators,” *Int. J. Non. Linear. Mech.*, vol. 125, no. April, p. 103516, 2020, doi: 10.1016/j.ijnonlinmec.2020.103516.

- [35] C. Zhao, M. H. Montaseri, G. S. Wood, S. H. Pu, A. A. Seshia, and M. Kraft, "A review on coupled MEMS resonators for sensing applications utilizing mode localization," *Sensors Actuators, A Phys.*, vol. 249, pp. 93–111, 2016, doi: 10.1016/j.sna.2016.07.015.
- [36] A. A. Seshia *et al.*, "A vacuum packaged surface micromachined resonant accelerometer," *J. Microelectromechanical Syst.*, vol. 11, no. 6, pp. 784–793, 2002, doi: 10.1109/JMEMS.2002.805207.
- [37] C. T.-. Nguyen, "MEMS technology for timing and frequency control," *IEEE Trans. Ultrason. Ferroelectr. Freq. Control*, vol. 54, no. 2, pp. 251–270, 2007, doi: 10.1109/TUFFC.2007.240.
- [38] T. Kose, K. Azgin, and T. Akin, "Design and fabrication of a high performance resonant MEMS temperature sensor," *J. Micromechanics Microengineering*, vol. 26, no. 4, p. 45012, 2016, doi: 10.1088/0960-1317/26/4/045012.
- [39] M. A. Hopcroft *et al.*, "Temperature Compensation of a MEMS Resonator Using Quality Factor as a Thermometer," in *19th IEEE International Conference on Micro Electro Mechanical Systems*, 2006, pp. 222–225, doi: 10.1109/MEMSYS.2006.1627776.
- [40] M. A. Hopcroft, "Temperature-stabilized silicon resonators for frequency references," *PhD thesis Mech. Eng. Stanford Univ.*, no. September, 2007.
- [41] W.-T. Hsu and C. T.-. Nguyen, "Stiffness-compensated temperature-insensitive micromechanical resonators," in *Technical Digest. MEMS 2002 IEEE International Conference. Fifteenth IEEE International Conference on Micro Electro Mechanical Systems (Cat. No.02CH37266)*, 2002, pp. 731–734, doi: 10.1109/MEMSYS.2002.984374.
- [42] M. Afridi, A. Hefner, J. Geist, C. Ellenwood, A. Varma, and B. Jacob, "Microhotplate-Based Sensor Platform for Standard Submicron CMOS SoC Designs," in *2005 International Semiconductor Device Research Symposium*, 2005, pp. 260–261, doi: 10.1109/ISDRS.2005.1596084.

- [43] K. E. Wojciechowski and R. H. Olsson, “A Fully Integrated Oven Controlled Microelectromechanical Oscillator—Part II: Characterization and Measurement,” *J. Microelectromechanical Syst.*, vol. 24, no. 6, pp. 1795–1802, 2015, doi: 10.1109/JMEMS.2015.2441045.
- [44] J. C. Salvia, R. Melamud, S. A. Chandorkar, S. F. Lord, and T. W. Kenny, “Real-Time Temperature Compensation of MEMS Oscillators Using an Integrated Micro-Oven and a Phase-Locked Loop,” *J. Microelectromechanical Syst.*, vol. 19, no. 1, pp. 192–201, 2010, doi: 10.1109/JMEMS.2009.2035932.
- [45] C. Liu, R. Tabrizian, and F. Ayazi, “A  $\pm 0.3$  ppm Oven-Controlled MEMS Oscillator Using Structural Resistance-Based Temperature Sensing,” *IEEE Trans. Ultrason. Ferroelectr. Freq. Control*, vol. 65, no. 8, pp. 1492–1499, 2018, doi: 10.1109/TUFFC.2018.2843781.
- [46] O. Kaya, T. Köse, and K. Azgım, “A Dual-Resonator Temperature Sensing Approach With Time Base Error Suppression,” *IEEE Sens. J.*, vol. 20, no. 2, pp. 707–714, 2020, doi: 10.1109/JSEN.2019.2943289.
- [47] T. Yin, H. Wu, Q. Wu, H. Yang, and J. Jiao, “A TIA-based readout circuit with temperature compensation for MEMS capacitive gyroscope,” *NEMS 2011 - 6th IEEE Int. Conf. Nano/Micro Eng. Mol. Syst.*, pp. 401–405, 2011, doi: 10.1109/NEMS.2011.6017377.
- [48] C. Zhang, Q. S. Wu, T. Yin, and H. G. Yang, “A MEMS gyroscope readout circuit with temperature compensation,” *2010 IEEE 5th Int. Conf. Nano/Micro Eng. Mol. Syst. NEMS 2010*, vol. 0, no. 1, pp. 458–462, 2010, doi: 10.1109/NEMS.2010.5592435.
- [49] B. Kim, M. Agarwal, J. Salvia, H. Mehta, and T. W. Kenny, “CMOS-COMPATIBLE DUAL-RESONATOR MEMS TEMPERATURE SENSOR WITH MILLI-DEGREE ACCURACY,” no. 3, pp. 229–232, 2007.
- [50] C. Chiang *et al.*, “A NOVEL , HIGH-RESOLUTION RESONANT THERMOMETER USED FOR TEMPERATURE COMPENSATION OF A

COFABRICATED PRESSURE SENSOR,” pp. 54–57, 2012.

- [51] K. A. A. Makinwa, “Smart Temperature Sensors in Standard CMOS.” [Online]. Available: [http://ei.ewi.tudelft.nl/docs/TSensor\\_survey.xls](http://ei.ewi.tudelft.nl/docs/TSensor_survey.xls). [Accessed: 01-Sep-2020].
- [52] K. Souri, R. Palwai, W. Chen, C. Arft, S. Tabatabaei, and C. Sechen, “Dual-MEMS-Resonator Temperature-to-Digital Converter with 40 $\mu$ K Resolution and FOM of 0.12pJK<sup>2</sup>,” pp. 200–202, 2016.
- [53] M. A. Hopcroft, W. D. Nix, and T. W. Kenny, “What is the Young’s modulus of silicon?,” *J. Microelectromechanical Syst.*, vol. 19, no. 2, pp. 229–238, 2010, doi: 10.1109/JMEMS.2009.2039697.
- [54] A. Torrents, K. Azgin, S. Godfrey, E. Topalli, T. Akin, and L. Valdevit, “MEMS Resonant Load Cells for Micro-Mechanical Test Frames: Feasibility Study and Optimal Design,” *J. Micromech. Microeng. J. Micromech. Microeng*, vol. 2050, pp. 125004–125017, Dec. 2010, doi: 10.1088/0960-1317/20/12/125004.
- [55] S. S. Rao, *Vibration of Continuous Systems*. 2007.
- [56] M. M. Torunbalci, S. E. Alper, and T. Akin, “The advanced MEMS (aMEMS) process for fabricating wafer level vacuum packaged SOI-MEMS devices with embedded vertical feedthroughs,” in *2015 Transducers - 2015 18th International Conference on Solid-State Sensors, Actuators and Microsystems (TRANSDUCERS)*, 2015, pp. 472–475, doi: 10.1109/TRANSDUCERS.2015.7180963.



## APPENDICES

### A. Temperature Controller Algorithm with Proportional-Integral Controller

```
clc
clear
close all
%% SET TEMPERATURE AND PID CONSTANTS
temp_set0=30 % degree C
temp_set1=30 % degree C
kp= 0.2023;
ki= 0.001251;
kd= 0;
%% SET POWER SUPPLY LIMITS and SETTINGS
sport = serial('COM3');
sport.Terminator = 'CR/LF';
fopen(sport);% Open virtual serial port
fprintf(sport, '*RST;*CLS;*OPC;*WAI');
%% Sample Power Supply Output
fprintf(sport, 'APPL 6.1, 0.0');
fprintf(sport, 'OUTP ON');
%% Read temp using PCI-4461
s = daq.createSession('ni');
addAnalogInputChannel(s, 'Dev1', 0, 'Voltage');
rate=204800;
s.Rate = rate;
s.DurationInSeconds=0.01;
dataIn=s.startForeground;
ai0=(dataIn(:,1))';
ai1=(dataIn(:,2))';
temp_ai0 = mean(ai0);

% Temperature calculations as a function of voltage
for LM35
    temp_act0 = temp_ai0*100.0; % Celsius
%%
i=1;
curr=0.000;
DT=0;
DT2=0;
Error_P=0;
Error_I=0;
Error_D=0;
time_log(1)=0;
```

```

temp0_log(1)=temp_act0;

while i<160000
i
tic
dataIn=s.startForeground;
    ai0=(dataIn(:,1))';
% plot(ai0); hold on ;    plot(ai1)
temp_ai0 = mean(ai0);
% Temperature as a function of voltage for LM35
temp_act0 = temp_ai0*100.0      % Celsius

DT=toc+DT2;
Error_P=temp_set0-temp_act0;
Error_I=Error_I+(temp_set0-temp_act0)*DT;
Error_D=(temp_set0-temp_act0)/DT;
tic
    curr=(kp*Error_P)+(ki*Error_I)+(kd*Error_D);
%%% Current limit
if    curr>1.4
    curr=1.399;
elseif curr<0
    curr=0.001;
end
% Send Current data to Power Supply
cur=num2str(sprintf('%.3f',curr));
to_pow_sup=['APPL 6.100, ',cur];          %E3640A
fprintf(sport, to_pow_sup);
%%%%% COLLECT DATA %%%%%%%%%%%%%%%%%%%%%%%%%%%%%%
temp0_log(i+1)=temp_act0; %under package
time_log(i+1)=DT+time_log(i);
current_log(i)=curr;
%%%%% PLOT DATA %%%%%%%%%%%%%%%%%%%%%%%%%%%%%%
plot(time_log,temp0_log);
ylabel('Temperature(deg C)')
xlabel('Time(sec)')

i=i+1;
DT2=toc;
end
%% After finish, run this code in command window
fprintf(sport, 'OUTP OFF') ;
fprintf(sport, '*RST');
fclose(sport);
delete(sport);
clear sport

```